Nanostructured Materials for Electrocatalytic Applications

RITU RAI

A thesis submitted for the partial fulfillment of
the degree of Doctor of Philosophy

Institute of Nano Science and Technology,
Knowledge City, Sector-81, SAS Nagar, Manauli PO, Mohali, 140306, Punjab, India.

Indian Institute of Science Education and Research Mohali
Knowledge city, Sector 81, SAS Nagar, Manauli PO, Mohali, 140306, Punjab, India.

March 2022

DEDICATED TO

My Father and Mother for all the unconditional love, untiring efforts, and endless support which has always motivated me to achieve my goals. You both have been my favorites. I will always be thankful to God for gifting such precious gems in my life …Love You, mom and dad….

The second pillar of my life is my husband who always encourages me to believe in myself and does best whatever be the situation. Thanks for being with me always.

Last but not least to my Father in law and mother in law who always supported and helped me to complete my work

Declaration

The work presented in this thesis has been carried out by me under the guidance of Dr. VIVEK BAGCHI at the Institute of Nano Science and Technology Mohali. This work has not been submitted in part or in full for a degree, a diploma, or a fellowship to any other university or institute. Whenever contributions of others are involved, every effort is made to indicate this clearly, with due acknowledgment of collaborative research and discussions. This thesis is a bonafide record of original work done by me and all sources listed within have been detailed in the bibliography.

RITU RAI

In my capacity as the supervisor of the candidate's thesis work, I certify that the above statements by the candidate are true to the best of my knowledge.

Dr. VIVEK BAGCHI

Acknowledgments

There are many people who became part of my journey but firstly I want to thank my supervisor **Dr. VIVEK BAGCHI** who always motivated and gave me full freedom for addressing new challenges. His way of handling and executing interesting ideas always inspired me to do something good. His deep and broad knowledge helped me a lot to execute my work nicely.

I also want to express my gratitude to **Prof Amitava Patra, Director INST Mohali** who has been making constant efforts in providing the best research faculties in the institute. His experience and vision will help this institute to reach greater heights.

I want to extend my thanks to the founding Director of INST **Prof. A.K Ganguli** who allowed me to be a part of this emerging institute. I will always appreciate the tireless efforts he made to build and grow this institute and provide well-equipped working labs in the initial years of the institute.

I also want to thank our INST collaborators **Dr. Ehesan Ali, Dr. Chandan Behra, Dr. Abir De Sarkar** who provided us huge support with deep theoretical calculations which helped us to validate our experimental results.

I genuinely want to thank my **Ph.D. review committee** for their important and valuable suggestions that helped me to complete my work appropriately.

I also want to extend my gratitude to all the **faculties of INST MOHALI** for facilitating me throughout my Ph.D. journey and allowing me to get access to broad instrumentation facilities under one roof. I also want to express my thanks to the **IISER faculty and INST faculty** for sharing and giving basic information about the various techniques during the course work that helped us in solving technical problems.

My special thanks to my lab members Mr. Rajinder, Mr. Zubair, Mr. Ashish, Mrs. Shilpa, Mr. Deepak, Mr. Krishankant, Mr. Vikas, Ms. Ashi for assisting me and always boosting me to complete my work. A special thanks to Mr. Rajinder and Mr. Zubair for always listening to my problems and providing the best solution for them. I also want to express my gratefulness to our lab alumni Dr. Sushmita, Mr. Apurbo, Ms. Ashima, Mrs. Kanika, and project trainee Ms. Shreya and Ms. Manali for being a part of my path.

Special and big thanks to Mr. Krishankant who worked tirelessly and coordinated with me to complete my last project in time. I will always remember the positive attitude and optimistic approach that you kept till the completion of this work.

I also want to thank my batch mates Dr. Dimple, Dr. Swati, Dr. Rashmi, Dr. Ashmeet, Dr. Ankur, Dr.Munish, Dr.Naimat, Dr.Soumen, and Dr.Anup for being constant well-wishers and supporters during the entire journey of my Ph.D.

I am also thankful to all the technical staff, non-technical staff, Administrative staff specially Gurveen mam and Late Shri P.K. Datta Sir for the unconditional support during my Ph.D. I also want to thank all the security guards, Ravinder uncle, and

paramjeet uncle for helping us in transferring various instruments and lab stuff from one place to another.

Very big thanks to INST MOHALI for providing the best research facilities, fully equipped labs, a homely environment, and funding for carrying out my Ph.D. research work also. I am also grateful to IISER MOHALI for providing a wonderful hostel facility during the initial years of my PhD

At last, I would like to express my heartiest gratitude towards my parents, my brothers, my husband, and most importantly my son who has been my ultimate source of motivation during thesis writing and made it possible for me to accomplish my goal.

.

TABLE OF CONTENTS

LIST OF FIGURES

LIST OF TABLES

ACRONYMS

XRD	X- ray diffraction
PXRD	Powder X ray diffraction
TEM	Transmission Electron Microscope
SEM	Scanning Electron Microscope
XPS	X ray photoelectron microscopy
FTIR	Fourier Transforms Infrared
UV-Vis	Ultraviolet visible Spectroscopy
TGA	Thermo Gravimetric Analysis
SAED	Selected area electron diffraction
DSC	Differential scanning calorimetry
HER	Hydrogen evolution reaction
CV	Cyclic voltammetry
LSV	Linear sweep voltammetry
Pt	Platinum
GO	Graphene Oxide
RGO	Reduced Graphene Oxide

EIS	Electrochemical Impedance Spectroscopy
EDX	Energy-Dispersive X-ray Spectroscopy
DFT	Density functional theory
THF	Tetrahydrofuran
OER	Oxygen evolution reaction
GCE	Glassy Carbon electrode
CP	Constant Phase Element
GC	Gas Chromatography
MS	Mass Spectrometry
LDH	Layered double hydroxide
GCD	Galvanostatic charge-discharge
EIS	Electrochemical Impedance Spectroscopy

ABBREVIATIONS

µl	Microliter
ml	Milliliter
λ	Wavelength
η	Over potential
θ	Theta
mg	Milligram
q	Charge
j	Current Density
°C	Degree Celsius
F	Faradays constant
Δ	Delta
Hz	Hertz
Å	Angstrom
Nm	Nanometer
mM	Mili Molar
cm	Centimeter

SYNOPSIS

ABSTRACT

The rising energy demands and the overuse of fossil fuels have deteriorated the environment to such an extent that a huge dependency is created on renewable sources of energy. One of the major destruction of using these fossil fuels is elevated CO_2 levels and ocean acidification which has created an unsafe environment for human beings and other living organisms [1-3]. The ultimate solution to this problem is to bring renewable sources of energy like solar energy, wind energy, etc. into usage. Although these forms of energies have somewhat succeeded in solving the existing issues related to energy but still they fail to deliver satisfactory performance due to problems associated with their inefficient technologies, availability of sources, and geographical errors. Hydrogen is an excellent fuel that can replace fossil fuels. It is a clean fuel and contributes least to the emission of greenhouse gasses [4]. Currently, steam reforming and coal gasification are two developed industrial techniques used majorly production of hydrogen. The main loopholes of these techniques are firstly they produce low-quality hydrogen and secondarily they are dependent on deteriorating fossil fuels [5, 6]. Therefore a new strategy should be looked upon for the production of hydrogen using a simple, eco-friendly, and efficient approach. Electrochemical Water splitting is one such method that produces a pure quality of hydrogen using water as a raw material. Hydrogen evolution reaction and oxygen evolution reaction are two important half-cell reactions of electrochemical water splitting. Nobel metal-based catalysts based on Pt and Pd are considered as state of art catalysts for hydrogen evolution reaction due to optimum binding energy and highest exchange current density in acidic as well as alkaline medium. But high cost and scarcity of these metals limit their applications on large scale. Therefore new materials based on non-noble metals which are abundant in nature should be designed and synthesized to replace the high-cost noble metals catalysts for hydrogen evolution reaction. Oxygen evolution reaction on the other hand is a more complex process as compared to hydrogen evolution reaction. The kinetic barrier associated with each step raises the overall potential required for driving the reaction. The oxides, hydroxides of Ir, Ru, and Rh are the most popular and efficient catalysts for oxygen evolution reaction yet their applicability is restricted due to their high cost.. Thus it is highly desirable to synthesize new catalytic materials based on non-noble metals and their composites for both oxygen evolution reaction and

hydrogen evolution reaction that show superior activity comparable to benchmark catalyst as well as good stability when used for longer durations. Carbon supports based on graphene and its derivatives are considered integral parts of these catalytic systems. They play an important role in holding the nanoparticles together as well as serve the purpose of activity enhancers either by boosting the interaction or participating in the reaction mechanism.

Based on the above concerns the present thesis is dedicated to the synthesis and fabrication of new catalytic nanomaterial for oxygen evolution reaction and hydrogen evolution reaction both based on metal oxides, hydroxides, metal nitrides, and phosphides of earth-abundant non-noble metals. It also focuses on devising a new methodology for the synthesis of reduced graphene oxide using a unique approach as compared to traditionally available chemical reduction and mechanical exfoliation methods.

The detailed outcome of each project is briefly summarized chapter-wise subsequently.

Chapter 1: Introduction

This chapter covers the background behind the origin of the problem, mechanistic aspects of the designed issue, a detailed literature analysis, and evaluating criteria for designing the new catalytic materials.

Chapter 2: Materials and Method

This chapter contains a brief description of various chemicals, methodologies, and processes involved in the synthesis and fabrication of catalytic materials. The elaborative details of materials and protocols involved in the synthesis of individual catalysts are discussed in respective chapters. The techniques used for the characterization of materials are also discussed subsequently.

Chapter 3: Environmentally Benign Metal-Free Reduction of GO Using Molecular Hydrogen: A Mechanistic Insight.

In this chapter, we report a simple methodology to synthesize RGO under hydrogen in THF, which can be scaled up effortlessly without compromising the quality of the product [7]. The extent of reduction reaches a maximum at a pressure of 40 bars at 180 °C. The reaction was carried out in a stainless steel pressure vessel, resulting in excellent quality RGO. The method of

extraction is very facile and imparts zero impurity, and hence, no purification is needed after reduction. The hydrogen reduced RGO (HRGO) achieves a C/O ratio higher than 11.3 and the ID/IG ratio obtained higher than 1.6. A detailed theoretical calculation reveals the possibility of the formation of solvated electrons in such a reaction, which is shown for the first time. A two-way approach was attempted to understand and detect the reactive intermediate responsible for such GO to RGO reduction. The first approach involved the use of a probe substrate in the same reaction condition. The second approach was to monitor the reaction mixture during the progress of the reaction using a UV−visible spectrophotometer connected to the reactor. DFT calculation directly correlating with the experimental results was performed to evaluate the electronic structure and properties of solvated electrons for the anionic, solvated, and neutral forms of THF. We hypothesized that the transient species is the solvated electron in THF. In the presence of suspended GO in THF at high pressure, H_2 generates H^+ and $^-$. The generated e− undergoes a different non-equilibrium relaxation process. It could reduce neutral THF to $[THF]^-$. The other possibility is that the generated electron could be solvated by THF solvent molecules. Here, we would like to emphasize that the electron is a fundamental quantum particle, and thus any classical picture of solvation (e.g., ions solvated in water) will certainly not hold. Rather, it is an additional electron that loosely bounds with multiple THF molecules and none of these solvents (THF) molecules that form the solvation shell can have exclusive access to that additional electron. Such special sharing of an electron between the THF molecules provides additional stability to be detected as the transient species.

Chapter 4: Ultrathin Co_3O_4 Nanosheets wrapped Mesoporous TiO_2 for oxygen evolution reaction.

In this chapter, a hybrid nanostructure with Mesoporous TiO_2 embedded on Co_3O_4 Nanosheet was developed for Oxygen evolution reaction. The integration of Mesoporous TiO_2 with Co_3O_4 interfaces indeed accelerates OER activity even in absence of any carbonaceous components. The heterostructure shows an OER activity with an overpotential of 340 mV at 10 mA/cm^2 with the long-term stability of 40000 Seconds. The electrochemical active surface area (ECSA) also indicates a higher activity for $TiO_2@Co_3O_4$. The low Tafel slope obtained in the case of catalyst i.e. 70 mV/dec indicates faster reaction kinetics. The catalyst also displays high turnover frequency and high faradaic efficiency justifying the superiority of the catalyst.

Chapter 5: Self-Supported $COVW_{0.025}$ LDH as a Catalyst for Hydrogen Evolution Reaction in Alkaline Medium.

In this chapter, self-supported $COVW_{0.025}$ LDH Nanosheets on Ni foam were synthesized using a simple one-pot precipitation method and used as a catalyst for alkaline hydrogen evolution reaction. On incorporation of tungsten into the CoVLDH, there is a significant improvement in the activity as over potential decreases to 127 mv from 200 mV. Moreover, the catalyst has a low value of Tafel slope indicating faster kinetics which is also reflected by a low value of charge transfer resistance. The catalyst was also found to be stable for 20 hours at a current density of 10 mA/cm^2 and 15 hours at a current density of 50 mA/cm^2.

Chapter 1

Introduction

1. Introduction

1.1 Energy crisis and the importance of Renewable energy

During the past few decades energy has been a hardcore backbone of economic growth, globalization, and development. It is one such key component on which the progress of various technological innovations is largely dependent. There is an annual increase of 2.3 % in energy consumption around the global world. The fossil fuels based on coal and petroleum amount to 86.4 % of the energy requirement of the world as per the information by EIA (2010) [1, 2]. Various conventional energy sources mainly fossil fuels have dominated the market and enjoyed popularity during this period. It has been further estimated that by 2020 the consumption of fossil fuels will be around 3.3 terawatts and is expected to increase further with the same projection for oil, natural gas, and coal [3] in coming years. The continuous use of these sources for meeting the energy requirements causes adverse effects on ecology making the environment unsuitable for both humans and organisms. The most severe and negative impact of these fossil fuels is that they are the major participant in releasing greenhouse gasses and causing global warming. On average 21.3 billion tons of carbon dioxide emissions are reported per year by the combustion of fossil fuels and the natural processes such as photosynthesis can absorb only half of the liberated amount thereby projecting an increase of 10.65 billion tons of carbon dioxide [4, 5]. Such uncontrolled rise in CO_2 levels over the years has huge impact on the earth's atmosphere as well as on human life and endangering many species. One such big consequence of rising CO_2 levels is the acidification of oceans which has come into the picture recently in a Royal society meeting and report [6]. Carbon dioxide and resulting ocean acidification are estimated to rise due to no curb on unchecked carbon emissions and climate mutations. Due to the continuous and unstoppable use of fossil fuels, the reservoirs of fossil fuels are diminishing rapidly making researchers and scientists all over the global world think of some other alternative sources of energy that can take up this challenge of replacing the major producers of energy. Renewable sources of energy are the emerging candidates which can provide solutions to multiple problems such as carbon emission, environmental degradation, and deteriorating fossil fuel reservoirs. Infinite and long-lasting supplies are the two main features of renewable sources of energy making them the most admirable candidates for solving the energy crisis. They are the cleaner sources of energy that cause minimum harm to the environment as compared to conventional fossil fuels. The major investments in the case of renewable energy sources are done on materials, manpower, and maintenance excluding the expenditure done on importing

energy. The success of renewable energy is largely dependent on the availability of the source but it can be beneficial and cost-effective after the development of the technology and the associated infrastructure [7]. Wind energy is one form of renewable energy which shows zero dependence on fossil fuels. It is an emission-free technology that does not carry the risk of causing any harmful effects on the environment. According to the report submitted by the world energy commission, 600 tons of CO_2 emissions can be clogged by using 1 million kWh of wind energy. The input of energy spent on installation of a wind plant is compensated by the amount of energy gained in the plant making it highly sustainable [8]. Solar energy is one of the biggest and everlasting source of energy which bears an enormous potential to fulfil the energy demands as compared to geothermal and biomass because of the availability of geothermal sources at fewer locations and lesser stock of biomass in nature [9, 10]. The earth's surface almost receives 4 million exajoules (1EJ= 10^{18} J) of energy out of which 5 X 10^{4} EJ is easily harvestable [11]. Despite this, the contribution of solar energy to the global energy supply is very little. Moreover, the intensity of solar radiation reaching the earth's surface is greatly mutated by the climate and geographical variation thereby decreasing its efficiency. Although there are numerous ideas and methods to utilize the available renewable energy sources yet they fail to accomplish the goals assigned to them due to inefficient technologies and geographical errors. Therefore there is an urgent need to discover new ways and technologies which can dig out maximum energy from the available energy resources.

1.2 Hydrogen as a fuel

Hydrogen as a fuel is a blooming candidate which can take up this challenge and solve the problems associated with the energy crisis and environmental degradation. It is one of the lightest elements and is present in ample amounts on earth. After the amendment of the energy policy act 1992, hydrogen flourished as a clean fuel. It has come into the picture due to its properties such as eco-friendly behavior, low volumetric density, higher efficiency, and easy production [12]. It is considered a green fuel because of its least contribution to global warming. It finds numerous applications in the industry sector as well as transport systems. As an energy source, the benefit of hydrogen can be taken with the help of fuel cell technologies. Easy Accessibility of Hydrogen due to vast production pathways using various renewable as well as non-renewable sources as shown in Fig below and a wide area of its applications has made it as popular as electricity. This creates a fight and comparison between different energy sources to deliver on commercial-scale platforms.

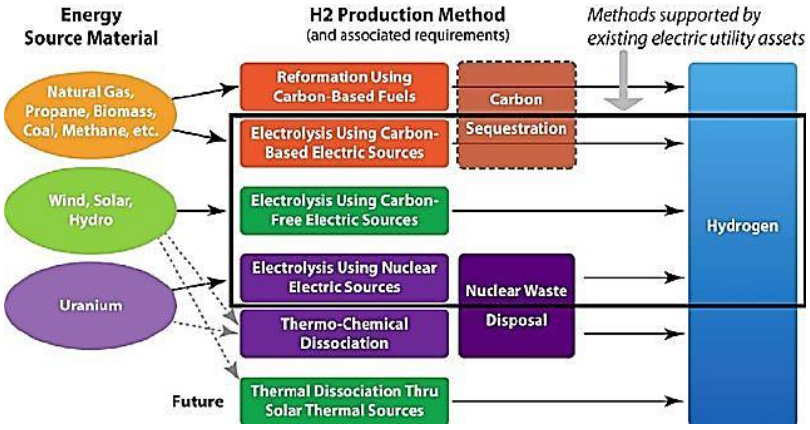

Fig 1.1: Production of Hydrogen using various renewable and non-renewable sources. Image reproduced from ref [13]

The peculiar feature which promotes and recommends the use of hydrogen as a fuel is summarized by the editor of the international journal of hydrogen energy who carries the specialization in hydrogen technology and energy summarized that [14, 15]

- Hydrogen is the ultimate source that can be made easily available to consumers in the easiest way.
- It can be converted into other forms of energy through various conversion approaches.
- It is an endless source because it can be easily obtained by electrolysis of water.
- The burning of hydrogen does not produce any pollutant emissions.
- It has the highest gravimetric density when compared with other fuels.
- It can be conveniently stored in the form of gas at high and low pressure, liquid hydrogen and trapped in the form of hydrides
- It can be easily transported either in native form or any of the forms discussed above.
- It is one of the main reactants in hydrogen-based fuel cells which carry efficiency of almost 60 % [16].

As compared to fossil fuels hydrogen is renewable and does not cause any harm to the environment. It has a great potential as fuel to solve energy-related issues in the coming era. The various properties of hydrogen and other fuels are discussed below in the table which proves the reliability of hydrogen as an energy carrier [17, 18]. It could be easily confirmed from

the below table that hydrogen has the highest energy/per unit mass among all the available conventional fuels. On combustion, it produces water vapours making the carbon emission zero. Moreover, it has a high energy conversion factor. All these factors make hydrogen to be considered as most superior fuel. In the present times although the hydrogen fuel technology seems to be less effective due to improvisations in the technologies related to it still it carries the fact that it could be a real and effective solution in fulfilling the demand for cleaner energy sources. It can also be believed that hydrogen can replace fossil fuels completely and become the most renowned and utmost source of cleaner and eco-friendly energy source in the future [15].

Table 1.1: Properties of various fuels along with hydrogen.

Fuel	Energy/Mass(unit J/Kg)	Energy/Volume (J/m^3)	Carbon emission
Liquid hydrogen	**141.90**	**10.10**	**0.00**
Hydrogen gas	**141.90**	**0.013**	**0.00**
Gasoline	**47.40**	**34.85**	**0.86**
Coal	**30.00**		**0.50**
Natural Gas	**50.00**	**0.04**	**0.46**
Bio diesel	**37.00**	**33**	**0.50**
Fuel Oil	**45.50**	**45.50**	**0.84**

On practical terms, the success and progress of hydrogen fuel technology are still affected by some particular issues related to production and storage such as:

- Hydrogen burns in the presence of air which raises operational safety concerns.
- The storage of hydrogen in liquid is a big challenge because a very low temperature is required for converting it into liquid form.
- High cost of technologies and processes involved.
- Heavy investments are required in transportation and distribution facilities to ensure the availability of hydrogen to the consumer.

Presently major percentage of hydrogen (around 96%) is produced by well-established technology. i.e. steam reforming which uses natural gas as a source. It is a well-renowned method for commercial hydrogen production. But the main loophole of this methodology is that it produces low purity hydrogen as well as it is highly dependent on the rapidly declining fossil fuels beds [19]. Coal gasification is another important industrial method deployed for the production of hydrogen. The presence of CO_2 along with hydrogen after the completion of processes reflects a serious threat to the environment questioning its sustainable behaviour [20]. Some other methods used for the production of hydrogen are electrolysis, wind, solar, and biomass which are still developing and struggling at the initial stages. Thus a new, highly efficient and cost-effective policy should be implemented for H_2 production. Electrochemical Water splitting has recently emerged as the finest method to produce hydrogen in high purity due to some salient features such as readily available water as a starting material, no emission of harmful greenhouse gases and most importantly high efficiency [21]**.** Alternatively, the water splitting can also be aided by some renewable sources of energy such as wind, solar energy, etc. Thus it can be conquered here that the hydrogen economy can be boosted by clubbing renewable energy sources and electrochemical water splitting as represented below.

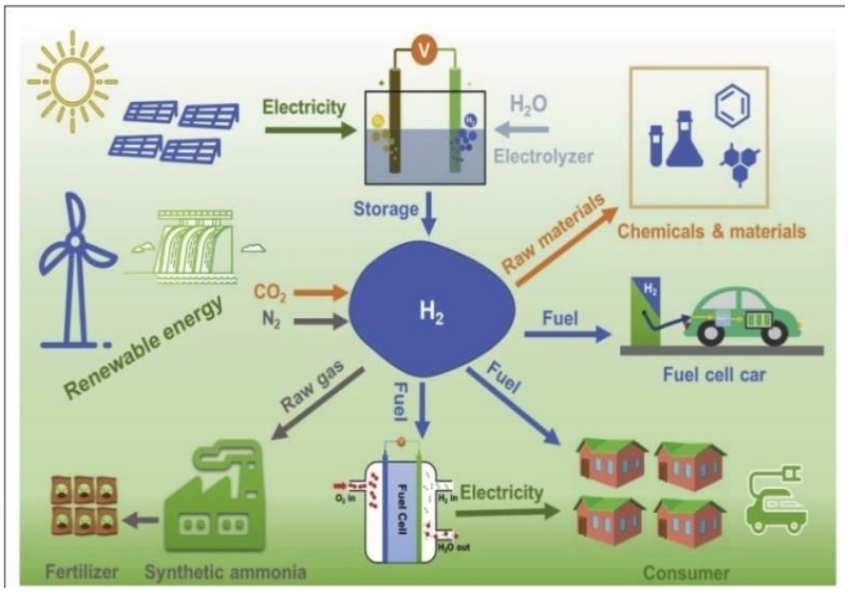

Fig 1.2: Representation of pathway for the transmission of the hydrogen by clubbing renewable sources and water splitting. Image reproduced from ref [22]

1.3 Electrochemical Water splitting

The first report of water splitting was made by Adriaan Paets van Troostwijk and Jan Rudolph Deiman in Haarlem, The Netherlands, in the year 1789 [23]. In their experiment, they

used the electrostatic machine invented by Martinus van Marum and applied the potential difference between two gold electrodes in a leyden jar. They observed the evolution of gasses on both the electrodes which were identified as hydrogen and oxygen respectively. After many years it became an integral part of strategies for tackling the world energy crisis. Having an edge over other known ways and means Electrocatalytic water splitting appears to be fruitful till the issues related to cost and energy efficiency gathered huge attention. Primarily the efficiency can be enhanced by discovering new catalytic materials which can split water with minimum energy input and maximum efficiency. In the early stages of water electrolysis precious metals and their oxides such as Pt, RuO_2 and IrO_2 were used to catalyse the reactions taking place at the electrodes which exaggerated the cost. This particular challenge can be addressed by using non-precious and earth-abundant metals as active materials. Over the few years, the hiked prices of electricity have somewhat delayed the production of hydrogen using electrolysis. This issue can be solved by making the use of big energy reservoirs present in the environment naturally for driving the electrolysis process.

1.3.1 Mechanism of Water Splitting

Electrochemical water splitting is a redox reaction that proceeds with the help of two half-cell reactions named as the Hydrogen evolution reaction taking place at the cathode and the oxygen evolution reaction taking place at the anode. Usually, the water-splitting reaction is either carried in an acidic medium or alkaline medium. The corresponding reactions in both the mediums are shown below [24].

Overall reaction

$2H_2O \longrightarrow 2H_2 + O_2$

In acidic electrolyte

At cathode: $2H^+ + 2e^- \rightarrow H_2 \quad E^\circ = 0\ V$

At anode: $2H_2O \rightarrow O_2 + 4H^+ + 4e^- \; E^\circ = 1.23V$

In alkaline electrolyte

Cathode: $4H_2O + 2e^- \rightarrow 2H_2 + 4OH^- \quad E^\circ = -0.83\ V$

At anode: $4\ OH^- \rightarrow O_2 + H_2O + 4e^-\ E^\circ = -0.40$ V

Irrespective of the medium of the electrolyte used the thermodynamic potential of water splitting is 1.23 V at 25 ^{o}C and 1 atm.

However, practically a potential higher than the thermodynamic potential is applied to drive this reaction. The excess potential (also called over potential η) is applied to get rid of inherent barriers appearing on both the electrodes and in the form of contact and solution resistances. Therefore the exact and real operational potential is represented as

$E_{op} = 1.23\ V + \eta_a + \eta_c + \eta_{other}$

From the above equation, it can be inferred that declining the overpotential would be an important step in making the water-splitting reaction energy efficient.

1.3.2 Hydrogen Evolution Reaction

Hydrogen evolution reaction is a two-electron process taking place at the surface of the cathode using two different mechanisms as shown in the scheme below [25, 26]. It proceeds with three well-defined steps in the acidic medium whereas the path is still uncertain in the alkaline medium. Experimentally fate of the mechanism which will be followed is disclosed by the value of Tafel slope [27, 28].

The first step which is the Volmer step is common in both the mechanisms. In this step, a proton is reduced and adsorbed on the catalyst by the transfer of one electron.

$H^+ + e^- \rightarrow H_{ads}$ Volmer step (1)

The Tafel slope for this step is given by the equation

$$b = \frac{2.303\ RT}{\beta\ F} \approx 120\ \text{mV/dec}$$

Where R stands is the universal gas constant, T is the temperature and F is faraday's constant.

After the completion of the Volmer step, the next step is decided based on H_{ads} coverage. If their high coverage of adsorbed hydrogen on the catalyst surface then two of the adsorbed hydrogen atoms combine chemically to liberate the hydrogen gas molecule. This reaction is known as the Tafel reaction and the Tafel slope, in this case, is given as

$$b = \frac{2.303\,RT}{2F} \approx 30 \text{ mV/dec}$$

In the reverse case if the catalyst surface is not able to hold a large number of adsorbed hydrogen on the surface leading to low coverage and exposure of vacant active sites then the adsorbed H atom will combine with a proton and electron simultaneously to evolve H_2 gas molecule. This reaction is named as Heyrovsky reaction and the corresponding Tafel slope is

$$b = \frac{2.303\,RT}{(1+\beta\,F)} \approx 40 \text{ mV/dec}$$

In the alkaline medium, the mechanism of hydrogen evolution reaction is not well defined. It is slightly slower due to its dependence on the deprotonation of hydroxide ions taking place on the anodic side which directly affects the supply of protons on the cathodic side. More protons formed after deprotonation combines with free hydroxide ions in the alkaline medium making it more difficult for the Hydrogen evolution reaction to proceed.

$H_2O + e^- \rightarrow H_{ads} + OH^-$ Volmer step

$H_2O + e^- + H_{ads} \rightarrow H_2 + OH^-$ Heyrovsky step

$H_{ads} + H_{ads} \rightarrow H_2$ Tafel step

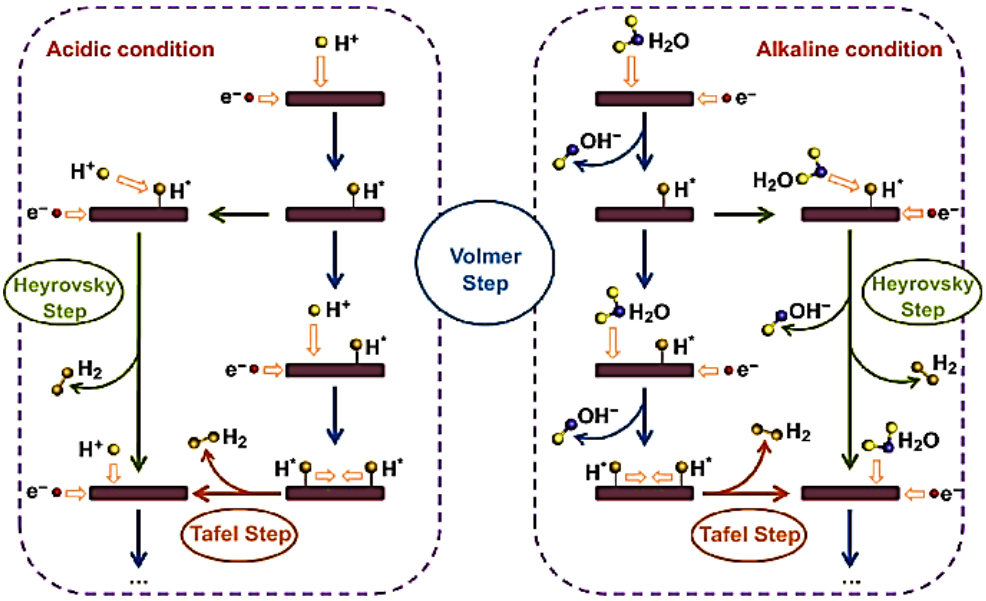

Fig 1.3: Mechanism of Hydrogen evolution reaction in acidic and alkaline medium. Image reproduced from ref [29]

Since in both the mechanisms the adsorption of hydrogen intermediate is the primary step thus the hydrogen-absorbing tendency is the core thing that needs to be carefully assessed

while studying the hydrogen evolving capability of any material. It is usually parameterized using the Gibbs free energy ($\Delta G_{H\ ads}$) of hydrogen adsorption. An ideal catalyst should have a value close to zero because if the value is too low then there will be poor interactions between protons and the electrode surface while a very high value will inhibit the desorption of hydrogen molecules from the surface due to strong interactions. Based on the experimental data obtained from DFT calculations for various metals volcano plot (ΔG_{Hads} vs log J_o) is plotted which gives more elaborative and deeper information about the HER activities of a wide range of metals both in the acidic and alkaline medium shown in Fig below [30, 31].

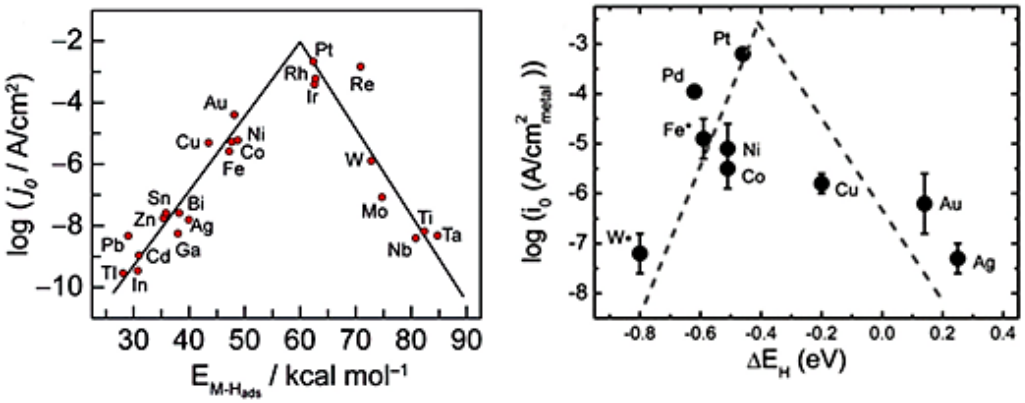

Fig 1.4: Volcano plots for HER in (a) acidic medium and (b) alkaline medium. Image reproduced from ref [30-32]

From the volcano plot, it can be observed that Pt is positioned at the top of the plot and it can be placed in the category of eminent catalyst for HER in both the medium because of its optimum binding energy and highest exchange current density. On contrary, the activity of HER in alkaline media is not convincing as in acidic medium [33]. This originates from the fact that the progress of the reaction is slowed down by the water dissociation step which declines the reaction rate. While rationalizing the design of the electrocatalyst it should be kept in mind that the catalyst should have the binding affinities for both hydrogen and dissociating water intermediates. The high cost and scarcity of noble metals limit their practicability on a larger scale. This has ignited the search for a new non-noble metal-based catalyst that can take up the challenge of replacing platinum-based catalyst. In the category of non-noble metal catalysts, various catalytic materials have been explored which include metal sulfides, metal carbides, metal nitrides, metal phosphides, and double layer hydroxides.

1.3.3 Oxygen Evolution Reaction

It is the counter-reaction four-electron process taking place at the anode. It has a more complex story as compared to the Hydrogen Evolution reaction. The kinetics in both the medium of electrolytes vary significantly. In the year 1969, a review article was published by Matsumoto and Sato13 Matsumoto [34] where all the OER mechanisms reported for both the electrolyte mediums are discussed. Out of them, the most widely and highly accepted pathways are oxide and electrochemical oxide pathways as represented in Fig below.

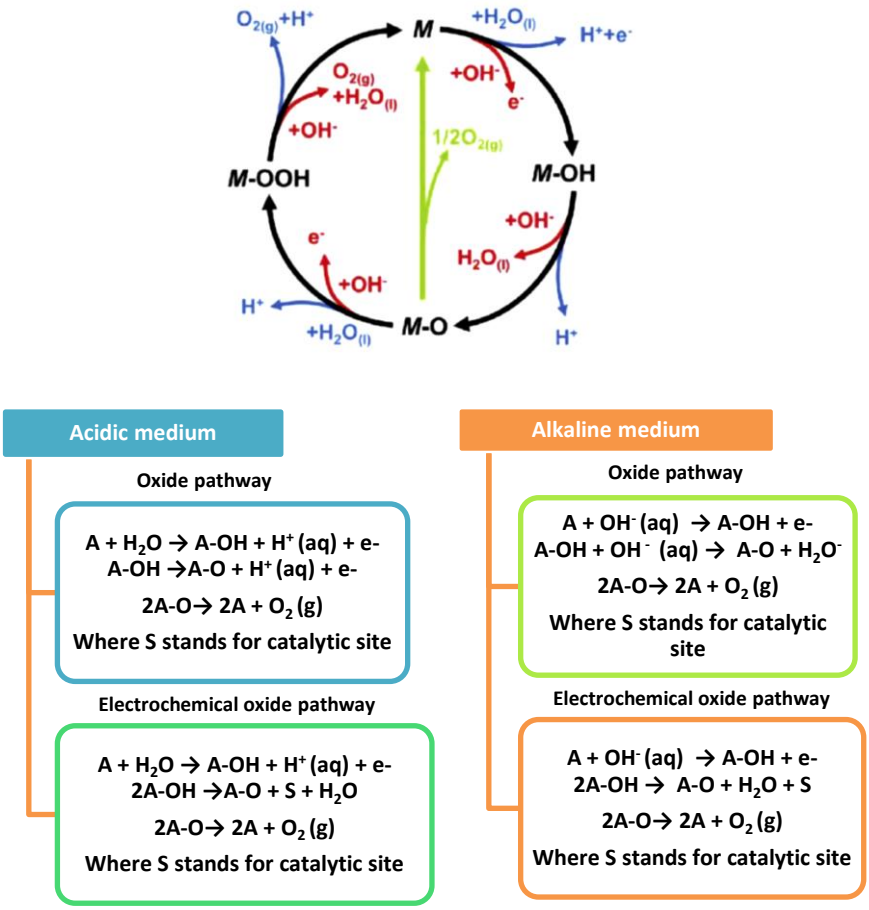

Fig 1.5: Mechanism of oxygen evolution reaction in acidic and alkaline medium

The primary step in all of them is the coordination of a hydroxide ion with the active site on the catalyst surface. Here it is important to visualize that in the acidic medium the water molecule is oxidized to oxygen gas molecule and hydrogen ion and in a basic and neutral electrolyte medium, the hydroxide ion present in the electrolyte is converted to oxygen molecule and water. The kinetic hurdle associated with each step raises the potential required to execute the reaction which indirectly increases the energy required to execute the reaction. The catalytic materials for OER mainly include oxides, and hydroxides, therefore, volcano plots for the broad range of oxides are obtained using the difference between the free energy

of O* and OH* intermediate for predicting the OER activity using $\Delta G_O - \Delta G_{OH}$ as an ideal descriptor for most of the oxides and hydroxides. This can be experimentally shown by Sabatier-based volcano relationship as shown in Fig below.

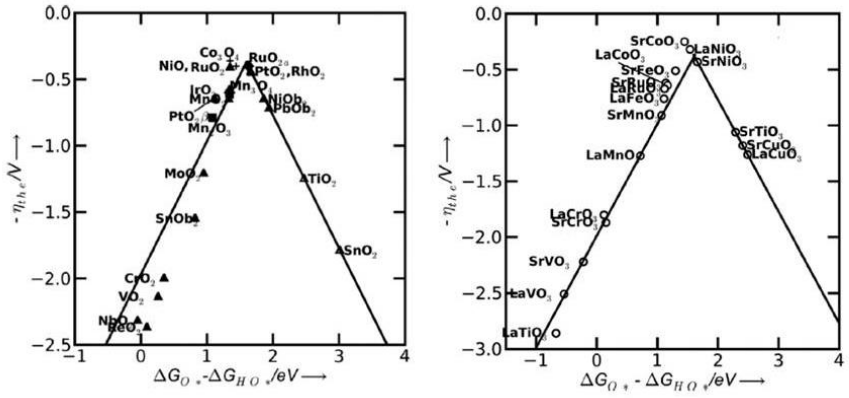

Fig 1.6: Volcano plot for OER

The catalyst surfaces to which oxygen binds too weakly, intermediates fail to react and the potential is hurdled by the oxidation of hydroxide intermediate whereas in the reverse case where intermediates adhere strongly the driving potential is lifted by the formation of OOH*. RuO_2, IrO_2, RhO_2, etc. are some of the metal oxides which are able to appear at the top of the volcano plot due to optimal binding strength thus proving their superior activity for OER [35]. They are also considered benchmark catalysts for Oxygen evolution reaction.

Besides this, another perilous factor of consideration is the selective adsorption of ions from the electrolyte can block the catalytic active sites which will further the performance of the catalyst material [35]. One of the recently highlighted issues in water electrolysis is the wettability of the electrode surface. Formation of hydrogen and oxygen results in the formation of gas bubbles that adhere to the electrode surface and block the active sites unless they are detached from the surface themselves. This can be avoided by detaching the bubbles mechanically by stirring the electrolyte solution and increasing the hydrophobicity of the catalytic material [36]. Optimizing the pore size and surface area can also be an effective method of minimizing the bubble growth and accelerating the detachment of bubbles [37]

1.4 Characteristics of a Good Electrocatalyst

Certain parameters are considered vital for analyzing the activities of the catalyst which are discussed in detail below.

1) **Overpotential (η):** An electrochemical reaction is always driven by a certain driving force in the form of applied potential. But whenever the reaction is carried out in the real experimental conditions then some additional driving force called overpotential needs to be applied to drive that reaction [35, 38]. Both HER and OER experience three types of kinetic barriers which give rise to three types of overpotential which are listed concentration overpotential, activation potential and the potential due to uncompensated resistance at the interface. The activation potential is directly linked to the efficiency of the catalyst. It can be removed by choosing a highly active material as a catalyst. Concentration potential arises due to the concentration difference of reactants and products in the bulk electrolyte and the interface due to delayed mass transport as the cell reaction proceeds. This can be rectified by stirring the solution. There is always some resistance at the surfaces and the interfaces of the measurement systems which causes an unavoidable voltage drop that adds to the measured value making it higher than the actual value. It can be corrected by doing an IR correction that is available in many workstations. Before reporting the values of overpotential for any catalyst it should always be iR corrected. In the hydrogen evolution reaction which has much simpler and faster kinetics the activation potential known as onset overpotential is an important tool [28]. This can be easily calculated with the help of the polarization curve which is obtained by plotting overpotential versus current density. Oxygen evolution reaction on other hand requires a couple of more factors for calculating the overpotential due to its complex and sluggish kinetics. As already discussed in the mechanism adopted by oxygen evolution reaction after the elementary step in which a water molecule coordinates in acidic medium and hydroxide ion coordinates in an alkaline medium a series of steps are followed. Each of these steps has definite kinetic hindrances that contribute in the overall activation over potential of the catalyst. Moreover with the variation in the catalyst their will huge variation in the kinetics of these materials due to differences in the adsorption tendencies of the intermediates involved with the different catalyst surfaces. Nowadays overpotential at fixed current density of 10ma/cm^2 is used as a chief factor for accessing the performance of the catalyst rather than onset potential for both of reactions [39] . In some special cases, the overpotential obtained at higher current density values such as 50 mA/cm^2 and 100 mA/cm^2 are reported [40, 41]. This happens when the redox peak falls in the potential window of gas evolution or the catalyst shows a very high current density reaching greater than 500 mA/cm^2. Lower is the value of overpotential at a particular current density more superior will be the catalyst.

2) Tafel slope and Exchange Current Density: Another set of important information about the catalyst is attained from Tafel plot analysis in the form of two physical considerations i.e. Tafel slope and exchange current density [21, 42]. Tafel plot is plotted between logarithmic value current density (log j) and the overpotential (η). The linear portion of the above plot gives the Tafel slope according to the equation

$$\eta = a + b \log j$$

Here η is overpotential, b is Tafel slope and j is the current density

The kinetic rate and type of mechanism followed are elucidated with the help of the Tafel slope. A lower value always reflects the superiority of the catalyst due to its faster kinetics.

After extrapolating the Tafel plot on a logarithmic scale at equilibrium potential that is at zero overpotential exchange current density is obtained. Usually, for the Tafel plot, the polarization curve is recorded at a slow scan rate. A lower scan rate sometimes leads to inaccurate values of exchange current density as in the case of capacitive materials. Secondly even after recoding the polarization curves at the lowest scan rate inaccuracy in the measurement of the Tafel slope still exists due to ohmic drop. To resolve this issue a new method was brought into the picture by Hu and co-workers [43] using electrochemical impedance spectroscopy. Nyquist plot at different potentials is obtained. After simulation and fitting of the obtained impedance curves with a circuit the values of charge transfer resistance are obtained and the slope of the plot of log Rct vs η is estimated which gives a more accurate and reliable value of the Tafel slope. Depending on the conditions and catalyst any of the methods can be used for determining the Tafel slope. Since hydrogen evolution displays similar kinetics for almost every type of catalyst thus a direct correlation between exchange current density and onset potential exists. Overall in the nutshell, it can be formulated that Tafel slope, exchange current density/onset overpotential are the main steps for HER where the catalyst should always be on top, and for OER since the kinetics is strongly affected by the type of catalyst and pH of the electrolyte medium Tafel slope and overpotential at fixed current density are the main deciding factors.

3) Stability: Anything that is not able to maintain its originality after a certain time is of no use. This thing is also applicable in the case of catalysts. Though a catalyst can be highly active by providing an efficient pathway for the reaction it can lose its quality if it is not able to sustain itself in the long durations. Thus it should be emphasized

that a good catalyst should always have high stability no matter what may be the experimental conditions. Different techniques are used for doing the stability studies of the catalyst such as cyclic voltammetry or linear sweep voltammetry and chronoamperometry or chronopotentiometry. For HER usually, CV or LSV curves are recorded for several thousands of cycles and after the completion difference in the onset cathodic potential and overpotential at 10 mA/cm^2 is noted. The durability of the catalyst is reflected if there is a minute difference between the two. The number of cycles for OER is limited to a few thousand. In recent reports, it has been observed that stability under a fixed potential or fixed current density for the time of several hours is a new tool for ensuring the stability of the catalyst. If the catalyst resists any large change in the current density and overpotential at 10 mA/cm^2 for an extended duration then it easily justifies its catalytic efficiency in all aspects

4) **Faradaic Efficiency:** Faradaic efficiency is defined as the competence of the electrocatalyst to push the electrons provided by the external potential across the interface barrier to the redox species involved in a particular electrochemical reaction. There are two sets of methods used for determining the faradaic efficiency [21]. The first method is the electrochemical method based on the RRDE technique and is typically applicable for oxygen evolution reactions. It is considered one of the accurate methods when the OER catalyst has two or more redox species in the working potential window or the catalyst can promote some other unwanted side electrochemical reactions. The electrocatalyst is coated on a Rotating ring disc electrode having a glassy carbon disc and Platinum ring. The potential window is set within OER limits at the disc side and constant potential for ORR is applied at the Pt ring. The faradaic efficiency is calculated as per the equations [44, 45].

$$\mathbf{FE} = I_R n_D / I_D n_R N_{CL}$$

I_R : current at the ring

n_D: no of electrons transferred at disc

n_R: no electrons transferred at the ring

I_D: current at disc

N_{CL} : collection efficiency of RRDE used

Collection efficiency is either known for the particular electrode or it can be estimated experimentally by collecting the data for standard Ferro/ferric redox couple at varying rotations. The second method is a widely used method both for HER and OER. Quantitatively the amount of gasses involved is calculated by integration either from chronoamperometric or chronopotentiometry analysis. The quantification, of the gasses involved practically using three different ways that are:

1) Water displacement method

2) Gas chromatography

3) Spectroscopic technique

The spectroscopic method is used in only those cases where the oxygen is excited to singlet state from triplet state and shows fluorescence. The amount of oxygen evolved can be directly correlated with the fluorescence intensity. The remaining two methods can be used depending on the resources available and catalyst material. Finally, the ratio of the amount of oxygen involved theoretically as well as experimentally gives what we call faradaic efficiency.

5) Turn Over Frequency: TOF is defined as no of molecules reacted at every catalytic active spot per unit time. It tells the inherent activity of the active site. It is calculated as per equation [46, 47]

$$\mathrm{T}OF = \frac{j\,A}{\alpha\,F\,N}$$

J is current density at defined overpotential from the LSV curve, A is the geometric area of the working electrode, α is the electron number of the catalyst, F is the Faraday constant of 96485.3 C /mol,n is the moles (mol) of covered metal atoms on the electrode. For heterogeneous catalysis, it is ambiguous to know the exact value of TOF for reaction particularly taking place at the surface of the electrode. The rational approach for this is to consider the involvement of only surface atoms or easily available active regions. Sometimes the value of TOF is calculated by assuming the participation of all active sites irrespective of the fact that they all are either equally /partially accessible or inaccessible. Besides the inaccuracy in the experimental or estimated value, TOF is calculated to have an awareness of catalytically active hotspots in the catalytic system.

6) **Mass activity and specific activity:** Mass activity and specific activity are two last things that are also important while evaluating catalyst performance. When the current is normalized with the loading of the catalyst on the electrode it is termed mass activity (A/g) and when it is normalized with electrochemical surface area (ESCA) or BET surface area it is called specific activity (A/cm^2). They are also defined in particular over potential. Both of these normalization methods have their own merits and demerits which are as follows. Depending on the nature of the catalyst any of the methods can be applied for normalization.

Table 1.2: Different methods of normalization

Method of normalization	Merits	Demerits
Geometric surface area	• **Widely and commonly used approach.** • **Easy comparison with reported literature**	• **Does not give accurate results.** • **The geometric area of the electrode is not exactly equal to the area of the catalyst involved**
ECSA	• **Reflects the actual and intrinsic activity of the catalyst.** • **It is highly sensitive to the loading of material**	• **It is difficult to determine ECSA accurately.** • **Existence of inaccuracies between different methods used for estimating ESCA such as CV and Impedance**
BET surface area	• **Easiest method because of the easy determination of the BET surface area of the catalyst.** • **Highly accurate in case of porous materials**	• **Does not reflect the real activity of the catalyst** • **Not all pores available in the catalyst are electrochemically participating in the electrochemical reaction**

Thus it can be concluded here that of all the parameters discussed above three of them which are Tafel slope, overpotential and stability are highly essential for judging the catalyst performance. It is also very interesting to note here that there is an in-built relation between all of these constraints which will be helpful in analyzing the overall performance of the

catalyst e.g. a polarization curve can give information both about current density and overpotential, information about Tafel slope and exchange current density can be simultaneously extracted with the help of Tafel equation, and turn over frequency can be correlated to overpotential and current density. Apart from this Electrochemical surface area is another important tool for a catalyst to show its efficacy. Till now the researchers have studied the activity of various catalysts at a particular pH but now it has been crucial to make such catalysts that can successfully catalyze the reaction with great efficiencies at the almost entire range of pH.

1.5 Understanding the importance of Heterostructures in Electrocatalysis

The active materials deployed to catalyze the assigned reactions often face difficulty due to agglomeration. They are usually decorated on 3D conductive commercial substrates such as Carbon cloth, Nickel foam, Titanium mesh, etc. They expose a large number of active sites due to three-dimensional architecture and also behave as good current collectors. Difficulties are faced while calculating the actual activity of the catalyst because neither the mass loading nor the surface area is precisely known. Now the focus has been shifted to nanostructured template decorated heterostructure materials like graphene, CNTs, C_3N_4, RGO etc. This kind of template material firstly provides the confinement zones which help in the formation of well-defined nanostructures and secondarily the presence of dopants can tune the electronic structure of carbonaceous supports which overall makes the catalyst more active. This belief has been successful in creating many efficient catalysts for hydrogen evolution reactions such as FeP/graphene [48], MoSe@ RGO [49], WS_2/RGO [50], and P doped WN@RGO [51]and CoP@NS doped RGO [52]etc.

Owing to their moderate binding energies all types of transition metal sulfides deliver good performances in hydrogen evolution reaction but when they are employed to form heterostructures they outshine as highly active catalysts for HER. Due to the synergistic effect and fast electron transfer among the different components of metal sulfides huge improvement in the activity is observed. Geo et al prepared $CoSe_2$/ MoS_2 [53] heterostructure which delivers very good performance with an overpotential of just 75mV and Tafel slope 36 mV/dec much close to the commercial Pt/C. Another composite based on CoSe/MoSe [54] shows fine performance for alkaline hydrogen evolution reaction with the overpotential of

218 mV. The progress in this class of materials is still going on to produce more efficient catalysts.

Moving on to other categories of heterostructures based on transition metal phosphides which also have excelled as good hydrogen evolution catalysts. Transition metal phosphides are the compounds of transition metal with the phosphorous atom. Almost all transition metals tend to form phosphides. They are divided into two categories one are metal-rich and the others are phosphorous-rich phosphides. The phosphorous atom being electronegative attracts the protons and thus promotes the hydrogen evolution. In the year 2015 Liu's group did DST calculations and found that the energy profile of HER on Ni_2P (001) surface resembles that of platinum proving that Ni_2P is a highly proficient catalyst for hydrogen evolution reaction [55]. After this Zhang et al carried out a detailed experimental study and discovered that nanoporous FeP is showing exceptionally good catalytic activity for HER. All these initial findings have inaugurated a platform for the development of new catalysts based on TMPS. Thus the thought of pairing TMP with other conductive and catalytic materials will be beneficial due to improved conductivities and abundant availability of active sites. For e.g. 3D self-supported Ni_5P_4-Ni_2P Nanosheet arrays on nickel foam were designed by Wang et al [56]. This composite shows high activity because of the synergistic effect between two phases of phosphides as well as the highly positively charged Ni atom and strong affinity of protons due to the P atom. Similarly, another combination of Ni_2P sheets on CoP wires assembled on Carbon cloth shows impressive performance with an overpotential of 55 mV and Tafel slope of 48 mV/dec [57].

Transition metal oxides have not shown any worthy performances for hydrogen evolution catalysis as transition metal phosphides and sulphides do due to the absence of active sites having a high affinity for protons and many of them lack adequate stability in the acidic environment due to corrosion. But few of the oxides-based heterostructures have shown good performances by overcoming these difficulties. A material composite based on MoS_2 & MoO_3 needs an overpotential of 250 mV for attaining a current density of 10 mA/cm^2 and was found to be stable for almost 10000 cycles [58]. In another case, MoS_2/MoO_2 composite synthesized by Yang et al group requires an overpotential of 240 mV with a Tafel slope of 76.1 mV/dec [59]. Many more improvisation is still needed to level up the activities of oxides-based heterostructures since many of the oxides does not bear good electrical conductivities and their tendency of getting corroded makes them a bad candidate as per the stability criteria of the catalyst is concerned.

Lately, it has been perceived that heterostructures based on double-layer hydroxides have also joined the race of developing an efficient catalyst for both acidic and alkaline hydrogen evolution reactions. They aid the water dissociation step which is the main reason of concern in the alkaline medium as per the latest reports. Almost in all kinds of reports, it has been studied theoretically as well as experimentally that they boost the activity of almost every type of catalytic material when used in the form of a composite material with them. They also work as a base to decorate the active species on the surface. Ni and Co-based double-layer hydroxides in combination with various transition metal ions such as V, Fe, Mn, Cu, Zn, etc. have shown their superiority in the water oxidation reaction. It has been noticed that poor conductivity and the limited number of active sites of these hydroxides have been huge hurdles in diminishing the activities of these types of catalysts. Thus different types of strategies are employed to enhance the activities.

1.6 Literature survey

Particularly for hydrogen evolution reaction Pt-based catalyst and for oxygen evolution reaction Ru and Ir based catalyst are considered as the most reliable and favorite catalysts but their popularity is often degraded by high cost and stability problems thus it has become mandatory to think and divert the approach towards non-noble metal-based catalyst for both the catalysis A lot of work has been published in recent tenure of few years that inspires us to change the tactic applied in developing and fabricating the new materials for catalysis applications. An overview of these findings has been discussed below in the table

Table 1.3 Showing recent literature studies

Electrocatalyst	Overpotential (V @ 10 mA/cm2)	Tafel slope (mV/dec)	Electrolyte	Reaction	Reference
NiO/β-Mo_2C/RGO	270 mV 237 mV	65.8 73.8	1 M KOH 0.5 H_2SO_4	HER	[60]
Cu/Cu_2O-CuO/rGO	105 mV	124 mV/dec	1 M KOH	HER	[61]
MoP@C@rGO	169 mV	79 mV/dec	0.5 H_2SO_4	HER	[62]
3D MoS_2 rGO@Mo	123 mV	62 mV/dec	1 M KOH	HER	[63]
Mo_2N–Mo_2C/HGr	157 mV 154 mV	55 mV/dec 68mV/dec	0.5 H_2SO_4 1 M KOH	HER	[64]
(Ni-MoS2)/ (RGO) hybrid aerogels	168 mV	69.5 mV /dec	1 M KOH	OER	[65]

NiCo2O4/NiO-rGO	350 mV	66 mV/dec	1 M KOH	OER	[66]
Ni-Bi/RGO	329 mV	79 mV /dec	1 M KOH	OER	[67]
rGO/Ni_2P	283 mV	43.6 mV	1 M KOH	OER	[68]
CoMnON/rGO	350 mV	70 mV/dec	1 M KOH	OER	[69]
$FeSe_2$@$CoSe_2$/rGO	260 mV	36 mV/dec	1 M KOH	OER	[70]
$NiPS_3$/graphene	294 mV	42.6 mV/dec	1 M KOH	OER	[71]
CoP@NG	354 mV	63.8 mV/dec	1 M KOH	OER	[72]
S-Co9–xFexS8@rGO	310 mV	105 mV/dec	1 M KOH	OER & ORR	[73]
ZnSe/$MoSe_2$	200 mV	73mV/dec	1 M KOH	HER	[74]
MoS_2 NDs/VS_2	291 mV	58.1 mV/dec	0.5 M H_2SO_4	HER	[75]
$Ni(OH)_2$/MoS_2	227 mV	105 mV/dec	1 M KOH	HER	[76]
MoS_2-WS_2 hetrostructure	129 mV	72 mV/dec	0.5 M H_2SO_4	HER	[77]
WS_2/CoS_2 @CC	175 mV	81 mV/dec	1.0 M phosphate buffer solution	HER	[78]
MoS_2/WTe_2	140 mV	40 mV/dec	0.5 M H_2SO_4	HER	[79]
$MoSe_2$-ts@MoS_2-t	186 mV	71 mV/dec	0.5 M H_2SO_4	HER	[80]
MoS_2/Co_9S_8@3DCarbon	177 mV	83.6 mV/dec	1.0 M KOH	HER	[81]
CoP(MoP)	198 mV	95 mV/dec	0.5 M H_2SO_4	HER	[82]
NiP_2/NiO NRs	131 mV	94 mV/dec	1 M KOH	HER	[83]
Ni-Fe phosphide	220 mV	41 mV/dec	1 M KOH	OER	[84]
Fe-Co-P alloy	252 mV	43 mv/dec	1 M KOH	OER	[85]
Ni_2P/FeP	250 mV 240 mV 295 mV	- 91 mV/dec 68.2 mV/dec	1 M KOH 0.5 M H_2SO_4 1 M KOH	HER HER OER	[86]
NiS/Ni_2P/CC	265 mV	76.1 mV/dec	1 M KOH	OER	[87]
Co/β-Mo_2C@N-CNTs	260 mV	67 mV/dec	1 M KOH	OER	[88]
NiCoFeP/NF	271 mV	45 mV/dec	1 M KOH	OER	[89]
MoS_2/CoSe	218 mV	76 mV/dec	1.0 M KOH	HER	[90]

1.7 Aim of the thesis

After going through the scenario of energy requirements, the importance of renewable sources of energy, and the commercialization of sustainable technologies there is utmost need to develop non-noble metal-based catalytic systems based on both oxygen evolution reaction and hydrogen evolution reaction which can replace the benchmark catalysts. Thus we aim to design and fabricate new nanomaterials which can superiorly catalyze the Electrocatalytic reactions and can maintain their performance throughout all the working conditions. Though we find a huge number of reports the foremost thing that needs to be understood here is that the methodology adopted for the synthesis of materials should be simple, cost-effective, and not time-consuming. Based upon all the considerations we have synthesized catalytic materials both for HER and OER based on elements such as Co, W, Ti, and V. Also by keeping in mind the importance of reduced graphene oxide as an integral support system for decorating nanomaterials and boosting activity we have devised a new and innovative method to synthesize reduced graphene oxide and did a systematic study both mechanistically as well as theoretically to have a deep understanding.

Chapter 3: This chapter covers the synthesis of reduced graphene oxide using a new strategy. Here the reduction of graphene oxide to reduced graphene oxide proceeds with the help of a solvated electron whose existence was proved theoretically for the first time.

Chapter 4: It involves the construction of a heterostructure based on TiO_2 and Co_3O_4 for oxygen evolution reaction. This work has highlighted the activity of titanium oxide for OER applications and opened new directions where the titanium oxide can be explored further by forming heterostructures with other metal oxides or hydroxides.

Chapter 5: This chapter is about the application of W doped CoV LDH that shows a great performance for alkaline hydrogen evolution reaction.

1.8 References

1. M. A. D. S. Bernardes, *Environmental impact of biofuels*, BoD–Books on Demand, 2011.
2. C. M. Drapcho, N. P. Nghim and T. Walker, *Biofuels engineering process technology*, McGraw-Hill Education, 2008.
3. M. Dresselhaus, G. Crabtree, M. Buchanan, T. Mallouk, L. Mets, K. Taylor, P. Jena, F. DiSalvo, T. Zawodzinski and H. Kung, *Basic Research Needs for the Hydrogen*

Economy. Report of the Basic Energy Sciences Workshop on Hydrogen Production, Storage and Use, May 13-15, 2003, DOESC (USDOE Office of Science (SC)); Argonne National Lab.(ANL), Argonne …, 2004.

4. S. Prasad, K. Sheetal, A. K. Chandel and M. Dhanya, *Sustainable Biofuels Development in India*, 2017, 435-458.
5. A. Pareek, R. Dom, J. Gupta, J. Chandran, V. Adepu and P. H. Borse, *Materials Science for Energy Technologies*, 2020, **3**, 319-327.
6. S. C. Doney, D. S. Busch, S. R. Cooley and K. J. Kroeker, *Annual Review of Environment and Resources*, 2020, **45**, 83-112.
7. U. Shahzad, *energy*, 2012, **2**, 16-18.
8. R. Saidur, N. Rahim, M. Islam and K. Solangi, *Renewable and sustainable energy reviews*, 2011, **15**, 2423-2430.
9. J. B. Holm-Nielsen and E. A. Ehimen, *Biomass supply chains for bioenergy and biorefining*, Woodhead Publishing, 2016.
10. P. G. V. Sampaio and M. O. A. González, *Renewable and Sustainable Energy Reviews*, 2017, **74**, 590-601.
11. M. Van der Hoeven, *International Energy Agency: Tokyo, Japan*, 2013.
12. M. Balat, *International journal of hydrogen energy*, 2008, **33**, 4013-4029.
13. B. Kroposki, J. Levene, K. Harrison, P. Sen, and F. Novachek, *Electrolysis: information and opportunities for electric power utilities*, National Renewable Energy Lab. (NREL), Golden, CO (United States), 2006.
14. M. Momirlan and T. N. Veziroglu, *International journal of hydrogen energy*, 2005, **30**, 795-802.
15. T. N. Veziroğlu and S. Şahi˙n, *Energy Conversion and Management*, 2008, **49**, 1820-1831.
16. G. Hoogers, *Fuel cell technology handbook*, CRC press, 2002.
17. S. Mekhilef, R. Saidur and A. Safari, *Renewable and Sustainable Energy Reviews*, 2012, **16**, 981-989.
18. J. Tabak, *Natural gas and hydrogen*, Infobase Publishing, 2009.
19. S. E. Hosseini and M. A. Wahid, *Renewable and Sustainable Energy Reviews*, 2016, **57**, 850-866.
20. K. Yamashita and L. Barreto, *Energy*, 2005, **30**, 2453-2473.
21. Y. Shi and B. Zhang, *Chemical Society Reviews*, 2016, **45**, 1529-1541.

22. Z. Chen, W. Wei, and B.-J. Ni, *Current Opinion in Green and Sustainable Chemistry*, 2021, **27**, 100398.
23. O. Diaz-Morales, F. Calle-Vallejo, C. de Munck and M. T. Koper, *Chemical Science*, 2013, **4**, 2334-2343.
24. J. Wang, X. Yue, Y. Yang, S. Sirisomboonchai, P. Wang, X. Ma, A. Abudula and G. Guan, *Journal of Alloys and Compounds*, 2020, **819**, 153346.
25. A. J. Bard and L. R. Faulkner, *Electrochemical methods*, 2001, **2**, 580-632.
26. J. Wei, M. Zhou, A. Long, Y. Xue, H. Liao, C. Wei and Z. J. Xu, *Nano-micro letters*, 2018, **10**, 1-15.
27. Y.-P. Zhu, X. Xu, H. Su, Y.-P. Liu, T. Chen and Z.-Y. Yuan, *ACS applied materials & interfaces*, 2015, **7**, 28369-28376.
28. P. C. Vesborg, B. Seger and I. Chorkendorff, *The journal of physical chemistry letters*, 2015, **6**, 951-957.
29. C. H. Lee and S. U. Lee, in *Electrocatalysts for Fuel Cells and Hydrogen Evolution-Theory to Design*, IntechOpen, 2018, p. 13.
30. S. Trasatti, *Journal of Electroanalytical Chemistry and Interfacial Electrochemistry*, 1972, **39**, 163-184.
31. T. R. Cook, D. K. Dogutan, S. Y. Reece, Y. Surendranath, T. S. Teets and D. G. Nocera, *Chemical reviews*, 2010, **110**, 6474-6502.
32. W. Sheng, A. P. Bivens, M. Myint, Z. Zhuang, R. V. Forest, Q. Fang, J. G. Chen and Y. Yan, *Energy & Environmental Science*, 2014, **7**, 1719-1724.
33. D. Strmcnik, M. Uchimura, C. Wang, R. Subbaraman, N. Danilovic, D. Van Der Vliet, A. P. Paulikas, V. R. Stamenkovic, and N. M. Markovic, *Nature chemistry*, 2013, **5**, 300-306.
34. Y. Matsumoto and E. Sato, *Materials chemistry and physics*, 1986, **14**, 397-426.
35. I. C. Man, H. Y. Su, F. Calle-Vallejo, H. A. Hansen, J. I. Martínez, N. G. Inoglu, J. Kitchin, T. F. Jaramillo, J. K. Nørskov and J. Rossmeisl, *ChemCatChem*, 2011, **3**, 1159-1165.
36. K. Zeng and D. Zhang, *Progress in energy and combustion science*, 2010, **36**, 307-326.
37. A. R. Zeradjanin, A. A. Topalov, Q. Van Overmeere, S. Cherevko, X. Chen, E. Ventosa, W. Schuhmann and K. J. Mayrhofer, *Rsc Advances*, 2014, **4**, 9579-9587.
38. E. Fabbri, A. Habereder, K. Waltar, R. Kötz and T. J. Schmidt, *Catalysis Science & Technology*, 2014, **4**, 3800-3821.

39. Y. Gorlin and T. F. Jaramillo, *Journal of the American Chemical Society*, 2010, **132**, 13612-13614.
40. S. Chen, J. Duan, M. Jaroniec and S. Z. Qiao, *Angewandte Chemie International Edition*, 2013, **52**, 13567-13570.
41. Y. Hou, M. R. Lohe, J. Zhang, S. Liu, X. Zhuang, and X. Feng, *Energy & Environmental Science*, 2016, **9**, 478-483.
42. I. Roger, M. A. Shipman, and M. D. Symes, *Nature Reviews Chemistry*, 2017, **1**, 1-13.
43. H. Vrubel, T. Moehl, M. Grätzel and X. Hu, *Chemical Communications*, 2013, **49**, 8985-8987.
44. T. N. Kumar, S. Sivabalan, N. Chandrasekaran and K. L. Phani, *Chemical Communications*, 2015, **51**, 1922-1925.
45. S.-X. Guo, Y. Liu, A. M. Bond, J. Zhang, P. E. Karthik, I. Maheshwaran, S. S. Kumar and K. L. N. Phani, *Physical Chemistry Chemical Physics*, 2014, **16**, 19035-19045.
46. Y. Guo, T. Park, J. W. Yi, J. Henzie, J. Kim, Z. Wang, B. Jiang, Y. Bando, Y. Sugahara and J. Tang, *Advanced Materials*, 2019, **31**, 1807134.
47. S. Anantharaj, P. E. Karthik, B. Subramanian, and S. Kundu, *ACS Catalysis*, 2016, **6**, 4660-4672.
48. Z. Zhang, B. Lu, J. Hao, W. Yang and J. Tang, *Chemical communications*, 2014, **50**, 11554-11557.
49. B. Hinnemann, P. G. Moses, J. Bonde, K. P. Jørgensen, J. H. Nielsen, S. Horch, I. Chorkendorff and J. K. Nørskov, *Journal of the American Chemical Society*, 2005, **127**, 5308-5309.
50. J. Yang, D. Voiry, S. J. Ahn, D. Kang, A. Y. Kim, M. Chhowalla and H. S. Shin, *Angewandte Chemie*, 2013, **125**, 13996-13999.
51. H. Yan, C. Tian, L. Wang, A. Wu, M. Meng, L. Zhao and H. Fu, *Angewandte Chemie*, 2015, **127**, 6423-6427.
52. Y. Lin, Y. Pan, J. Zhang, Y. Chen, K. Sun, Y. Liu and C. Liu, *Electrochimica Acta*, 2016, **222**, 246-256.
53. M.-R. Gao, J.-X. Liang, Y.-R. Zheng, Y.-F. Xu, J. Jiang, Q. Gao, J. Li, and S.-H. Yu, *Nature communications*, 2015, **6**, 1-7.
54. G. Zhao, P. Li, K. Rui, Y. Chen, S. X. Dou, and W. Sun, *Chemistry-A European Journal*, 2018, **24**, 11158-11165.

55. P. Liu and J. A. Rodriguez, *Journal of the American Chemical Society*, 2005, **127**, 14871-14878.
56. X. Wang, Y. V. Kolen'ko, X. Q. Bao, K. Kovnir and L. Liu, *Angewandte Chemie*, 2015, **127**, 8306-8310.
57. W. Tang, J. Wang, L. Guo, X. Teng, T. J. Meyer and Z. Chen, *ACS applied materials & interfaces*, 2017, **9**, 41347-41353.
58. Z. Chen, D. Cummins, B. N. Reinecke, E. Clark, M. K. Sunkara and T. F. Jaramillo, *Nano letters*, 2011, **11**, 4168-4175.
59. L. Yang, W. Zhou, D. Hou, K. Zhou, G. Li, Z. Tang, L. Li and S. Chen, *Nanoscale*, 2015, **7**, 5203-5208.
60. J. Ni, Z. Ruan, S. Zhu, X. Kan, L. Lu and Y. Liu, *ChemElectroChem*, 2019, **6**, 5958-5966.
61. L. Ye and Z. Wen, *Chemical Communications*, 2018, **54**, 6388-6391.
62. Y. Zhang, J. Yang, Q. Dong, H. Geng, Y. Zheng, Y. Liu, W. Wang, C. C. Li and X. Dong, *ACS applied materials & interfaces*, 2018, **10**, 26258-26263.
63. B. He, L. Chen, M. Jing, M. Zhou, Z. Hou and X. Chen, *Electrochimica Acta*, 2018, **283**, 357-365.
64. H. Yan, Y. Xie, Y. Jiao, A. Wu, C. Tian, X. Zhang, L. Wang and H. Fu, *Advanced Materials*, 2018, **30**, 1704156.
65. C. Lin, Z. Gao and J. Jin, *ChemSusChem*, 2019, **12**, 457-466.
66. Y. Wang, Z. Zhang, X. Liu, F. Ding, P. Zou, X. Wang, Q. Zhao, and H. Rao, *ACS Sustainable Chemistry & Engineering*, 2018, **6**, 12511-12521.
67. X. Cao, L. Cui, X. Wang, W. Yang and J. Liu, *ChemCatChem*, 2018, **10**, 2826-2832.
68. X. Tao, S. Luo, C. Tian, Y. Qing, X. Lu, N. Yan, and Y. Wu, *ACS Sustainable Chemistry & Engineering*, 2020, **8**, 1859-1867.
69. Z. Yan, H. Qi, X. Bai, K. Huang, Y.-R. Chen and Q. Wang, *Electrochimica Acta*, 2018, **283**, 548-559.
70. G. Zhu, X. Xie, X. Li, Y. Liu, X. Shen, K. Xu, and S. Chen, *ACS applied materials & interfaces*, 2018, **10**, 19258-19270.
71. S. Xue, L. Chen, Z. Liu, H.-M. Cheng and W. Ren, *ACS nano*, 2018, **12**, 5297-5305.
72. Y. Lu, W. Hou, D. Yang and Y. Chen, *Electrochimica Acta*, 2019, **307**, 543-552.
73. T. Liu, F. Yang, G. Cheng and W. Luo, *Small*, 2018, **14**, 1703748.
74. M. Wu, Y. Huang, X. Cheng, X. Geng, Q. Tang, Y. You, Y. Yu, R. Zhou and J. Xu, *Advanced Materials Interfaces*, 2017, **4**, 1700948.

75. C. Du, D. Liang, M. Shang, J. Zhang, J. Mao, P. Liu and W. Song, *ACS Sustainable Chemistry & Engineering*, 2018, **6**, 15471-15479.
76. B. Zhang, J. Liu, J. Wang, Y. Ruan, X. Ji, K. Xu, C. Chen, H. Wan, L. Miao and J. Jiang, *Nano Energy*, 2017, **37**, 74-80.
77. N. Huo, J. Kang, Z. Wei, S. S. Li, J. Li and S. H. Wei, *Advanced Functional Materials*, 2014, **24**, 7025-7031.
78. J. Wu, T. Chen, C. Zhu, J. Du, L. Huang, J. Yan, D. Cai, C. Guan and C. Pan, *ACS Sustainable Chemistry & Engineering*, 2020, **8**, 4474-4480.
79. Y. Zhou, J. V. Pondick, J. L. Silva, J. M. Woods, D. J. Hynek, G. Matthews, X. Shen, Q. Feng, W. Liu and Z. Lu, *Small*, 2019, **15**, 1900078.
80. M. D. Sharma, C. Mahala and M. Basu, *Inorganic chemistry*, 2020, **59**, 4377-4388.
81. M. S. Kim, C. Seo, H. Kim, J. Lee, D. H. Luong, J.-H. Park, G. H. Han and J. Kim, *ACS nano*, 2016, **10**, 6211-6219.
82. L. Yu, Y. Xiao, C. Luan, J. Yang, H. Qiao, Y. Wang, X. Zhang, X. Dai, Y. Yang and H. Zhao, *ACS applied materials & interfaces*, 2019, **11**, 6890-6899.
83. M.-Y. Wu, P.-F. Da, T. Zhang, J. Mao, H. Liu and T. Ling, *ACS applied materials & interfaces*, 2018, **10**, 17896-17902.
84. C. Huang, Y. Zou, Y.-Q. Ye, T. Ouyang, K. Xiao and Z.-Q. Liu, *Chemical Communications*, 2019, **55**, 7687-7690.
85. K. Liu, C. Zhang, Y. Sun, G. Zhang, X. Shen, F. Zou, H. Zhang, Z. Wu, E. C. Wegener and C. J. Taubert, *ACS nano*, 2018, **12**, 158-167.
86. H. Wang, X. Wang, B. Zheng, D. Yang, W. Zhang and Y. Chen, *Electrochimica Acta*, 2019, **318**, 449-459.
87. X. Xiao, D. Huang, Y. Fu, M. Wen, X. Jiang, X. Lv, M. Li, L. Gao, S. Liu and M. Wang, *ACS applied materials & interfaces*, 2018, **10**, 4689-4696.
88. T. Ouyang, Y. Q. Ye, C. Y. Wu, K. Xiao and Z. Q. Liu, *Angewandte Chemie*, 2019, **131**, 4977-4982.
89. Q. Zhang, D. Yan, Z. Nie, X. Qiu, S. Wang, J. Yuan, D. Su, G. Wang and Z. Wu, *ACS Applied Energy Materials*, 2018, **1**, 571-579.
90. M.-R. Gao, J.-X. Liang, Z. Ya-Rong, Y. Xu, J. Jiang, Q. Gao, J. Li and S.-H. Yu, *Nature communications*, 2015, **6**, 5982.

Chapter 2

Materials and Methods

2.1. Chemicals and Reagents used in experimental work

Chemical /Reagent	Company
Cobalt Nitrate Hexahydrate $(Co(NO_3)_2.6H_2O)$	CDH
Titanium Isopropoxide $Ti\ [OCH(CH_3)_2]_4$	Sigma
Ammonium Metavanadate (NH_4VO_3)	Himedia
Cobalt chloride	Loba Chemie
Melamine $(C_3H_6N_6)$	Loba Chemie
Urea (NH_2CONH_2)	Avra
Sodium hydroxide	Loba Chemie
Ammonia (NH_3)	Emparta
Sodium Borohydride $(NaBH_4)$	Avra
Ethanol (C_2H_5OH)	Honey Well
N, N- Dimethylformamide (C_3H_7NO)	CDH
Tetrahydrofuran $(CH_2)_4O$	Himedia
Hydrochloric acid (HCl)	Himedia
Graphite flakes	Sigma
Potassium Permanganate KMnO4	Merck
Diethyl Ether $(C_2H_5)_2O$	Merck
Hydrogen Per Oxide (H_2O_2)	Merck
Nafion Perfluorinated resin in (5 % lower aliphatic alcohols and 15-20 % water)	Sigma

2.2 Synthesis Methods

The methods used for synthesis in this thesis are:

1. Hydrothermal and Solvothermal process
2. Calcination process
3. Solvothermal process at high temperature and pressure using High-pressure reactor.

2.2.1 Hydrothermal and Solvothermal Process

Material science is a new field that requires constant development in the processes and the methodologies used for the synthesis of new materials with the processes which require low energy, simple protocols, and cause less pollution [1, 2]. Inorganic materials were synthesized by three types of methods which are solid phase, liquid phase, and gas-phase [3, 4]. Each one of them has its pros and cons as discussed below in Fig 2.1.

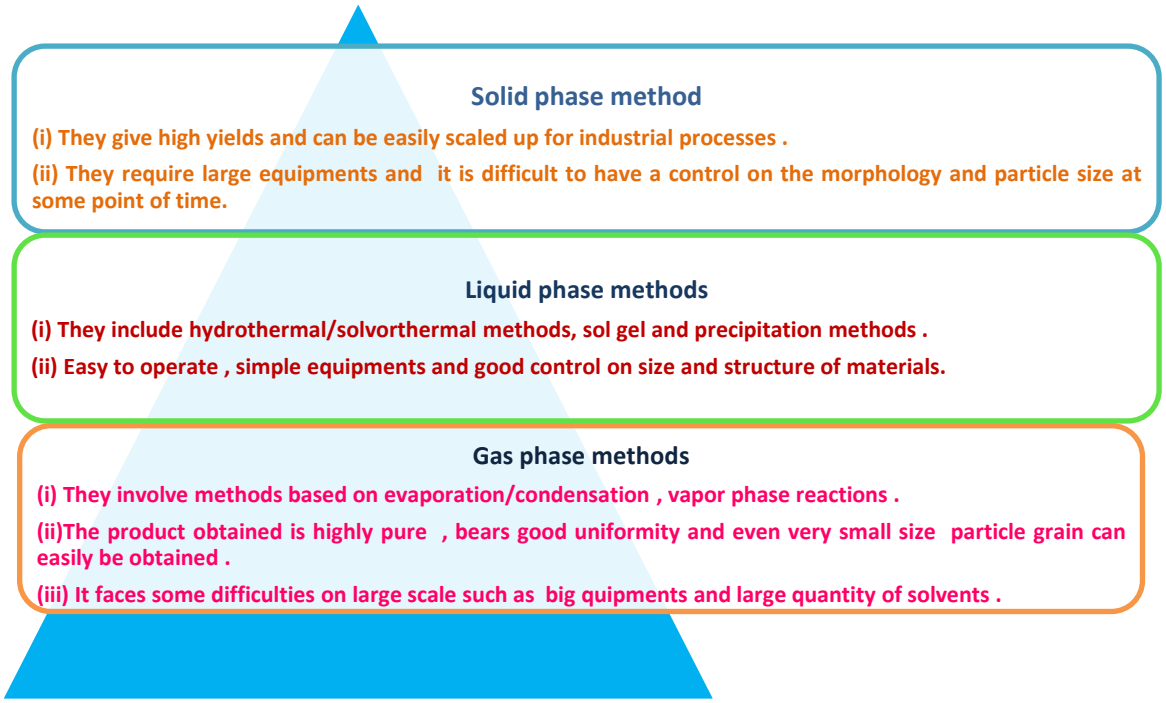

Fig 2.1: Comparison of solid phase, liquid phase, and gas-phase methods

Hydrothermal/solvothermal method is one such method that has been constantly attaining attention in recent years. Initially, this method was limitedly used in the manufacturing processes of ores from nature but slowly and steadily it has found a suitable place in many important branches of science such as material, chemistry, physics, etc. For making this

technique more economical and practical it has been hybridized with electric field[5], microwave [6, 7] which has improved the reaction kinetics to a large extent thereby reducing the time duration. It has been now widely used in the synthesis of inorganic materials. The beauty of this is that it provides control on crystal size, and morphology just by changing the experimental conditions such as pH, solvent, temperature, time, and varying ratios of starting ingredients, etc.

2.2.2 Details of Hydrothermal method

Hydrothermal method was used by the geologists previously for the formation of some rocks and minerals but later on, it was also applied for the growth of single crystals and powdered samples. In this method, the reactants are heated in a closed sealed vessel to create high temperature and pressure conditions on heating. This vessel is called a hydrothermal bomb which consists of a steel jacket and a Teflon container Fig 2.2 (a). When the reacting materials are heated at high temperature and pressure the density of ionic products, the viscosity of solvents used, and ionic products are subjected to huge variations thereby increasing the solubility and reactivity of the participating reactant molecules which are supposed to be unreactive or insoluble at room temperature conditions [8, 9]. This facilitates the formation of a variety of inorganic ceramic materials at low temperatures which are difficult to synthesize in simpler conditions. The sequence of steps involved in a typical hydrothermal synthesis are discussed in Fig 2.2(b)

Fig 2.2: (a) Hydrothermal vessel (b) Details of steps involved in hydrothermal synthesis.

Both hydrothermal and solvothermal are commonly used methods in inorganic synthesis. Both of them involve a similar strategy but the only difference between the two is that in hydrothermal the reaction is carried out in water solvent whereas in solvothermal it is done in a non-aqueous solvent. It has been witnessed during the hydrothermal reactions that some of the compounds are not soluble in water even when the reactions are performed at high

temperatures. To enhance the activity in those situations some additional substances called mineralizers are added to the reaction mixture to raise the solubility and promote the crystal growth. These substances are usually acids, bases, and salts [10-12]. The advantages of these mineralizers are:

- They elevate the activity of solute and modify the solubility coefficient.
- They tend to form complexes with crystalline substances which can catalyse the growth and nucleation rates.
- They can also direct the growth of nucleation sites in a particular direction or planes giving rise to different morphologies of the same inorganic material.

The Hydrothermal reaction can be divided into various categories as discussed below Fig 2.3

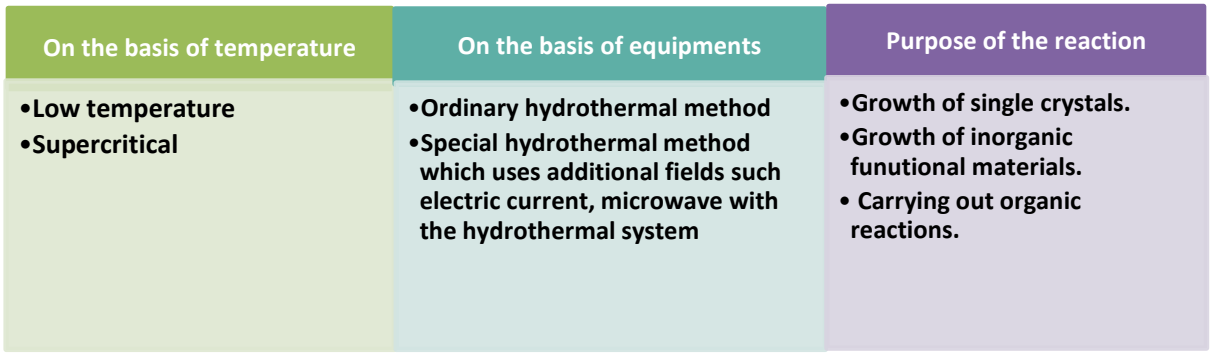

Fig 2.3: Categories of Hydrothermal reaction.

2.2.3 Calcination process

Calcination is a process of heating inorganic materials in the presence of air which causes thermal decomposition, phase transition, or removal of a volatile component. This has become a major step in the synthesis of a large number of oxide materials. The product obtained after calcination usually consist of small crystallite particles. As it removes the volatile component from the calcined product it can promote the development of cracks and cause sintering also. Mostly the oxides materials with high purity and suitable characteristics are obtained by the calcination of their crystalline/amorphous oxides, carbonates, organometallic salts, etc. Low-temperature sintering results in the generation of small size crystallites (2-10 nm) which are held by weak forces but the high-temperature sintering results in the formation of big crystallites (>100 nm) held strongly. The materials obtained

after hydrothermal reaction or liquid phase reaction are calcined in the presence of inert gasses at certain temperatures using a controlled program. This is usually applied for the synthesis of various compounds of transition metals such as nitrides, carbides, phosphides, and sulfides. During these reactions oxide particles either react with the solid precursors or gaseous source at specified temperatures or controlled rate of reaction to yield the required products. The texture, crystallite size, and surface area are highly affected by the temperature at which calcination is performed.

2.2.4 High-Pressure reactor

The High-pressure reactor is a specially designed vessel used to carry out chemical reactions which require specific pressure such as hydrogenation and polymerization etc. The pressure is generated internally or created by the use of an external source. This kind of vessel finds application in modifying the sample with hydrogen[13] or carbon dioxide. This system has several advantages over the conventional round bottom flask method because firstly it enables to carry out the reaction at high pressure and high temperature which are even greater than the boiling point of solvents involved in the reaction secondly it causes minimum decay of substrates as well as products thereby producing clean reaction profile.

2.3 Synthesis of Graphene oxide

Graphene oxide was synthesized by an improved method of synthesis of graphene oxide[14]. In brief 500 mg of graphite was dissolved in 60 ml of sulphuric acid and 6.5 ml of phosphoric acid. 3 g of potassium permanganate was added in the above solution slowly with vigorous stirring. After that, the above solution was stirred at 50^{o}C for 12 hours. The solution was cooled to room temperature after some time 100 ml of crushed ice was added into the above solution followed by slow addition of 1 ml of hydrogen peroxide. The solution becomes yellowish. The obtained solution was filtered and washed with distilled water, conc HCl, and diethyl ether. The solid obtained was vacuum dried overnight.

2.4 Characterization Techniques

2.4.1 Powder X-Ray Diffraction

X-ray diffraction is a basic analytical technique used to identify the phase and crystal structure of crystalline material. It gives important information about the phase of the synthesized material, crystallite size, and unit cell dimensions. It was discovered by Max von

Laue in the year 1912. In a typical X-ray diffractometer X-rays, a cathode ray tube is used to generate the X-rays which are further filtered to get monochromatic radiation. These rays are then directed towards the sample after collimation. These incident rays interact with the different crystal planes and get diffracted, when the brags law condition Bragg's Law ($n\lambda=2d \sin\theta$) is satisfied, a constructive interface takes place and a peak is observed in the diffraction pattern. The sample is scanned through a range of two angles to collect all possible diffraction directions. Once all the diffraction peaks are collected, the d spacing value of each peak is calculated which is matched with the standard pattern. This helps in the identification of material since each material has characteristic d spacing values due to different crystal structures.

Brag's Law

The principle of X diffraction is based on Brag's law which was explained by Sir W.H. Bragg and his son Sir W.L. Bragg which stated that when the x-ray falls onset of parallel planes of the crystal atom constructive interface will take place when the path difference between the two is a whole number multiple n of the incident ray wavelength.

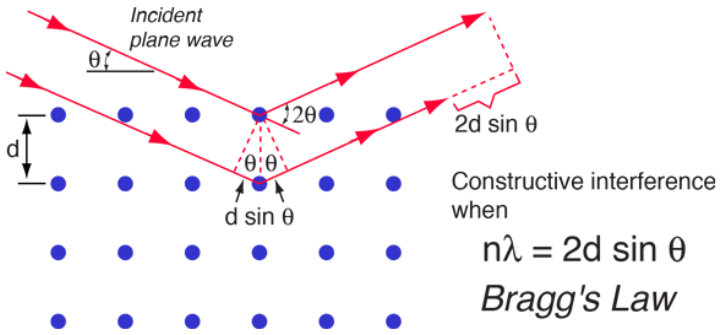

Fig 2.4: Image showing x-ray diffraction in a crystal lattice

X-ray diffraction patterns can be obtained either from a single crystal or the power of the material Powder X-ray diffraction is easier than single-crystal diffraction because the latter requires the synthesis of single crystals of high purity. A diffraction pattern plots intensity against the angle of the detector, 2θ.

Another set of important information that can be extracted from PXRD X-ray diffraction is crystallite size. It can be calculated using Scherrer formula [15] which is given as

$$L = \frac{K\lambda}{\beta \cos\theta} \qquad (1)$$

L: Crystallite size

K: Shape Factor

λ: Wavelength of X rays

β: Half-width at half maxima of the peak in radians

θ: diffracted angle of peak

Sometimes broadening in the peaks is observed which is related to physical broadening and instrumental broadening [18,19]. For minimizing the instrumental broadening instrument is usually calibrated with silicon as standard reference material.

In this thesis, the Powder X-ray diffraction of materials was done using the Bruker D8 Eco setup instrument

2.4.2 Scanning Electron Microscopy

Scanning Electron microscopy is a technique used to get topographical information about the material. The focused beam of high-energy electrons is directed on the surface of the solid sample. Data is collected by selecting a particular area of the sample and a two-dimensional image is created. Normally the regions having a width from 1cm to 5 microns are selected in the scanning mode of conventional SEM. From the SEM analysis of selected point locations we can also get qualitative as well as quantitative information about the chemical composition of the material using the EDX technique.

Working Principle of SEM

When the high-energy X-ray beam falls on the specimen sample variety of signals are produced mainly in the form of backscattered, secondary electrons and photons corresponding to the characteristics X rays from the surface of the sample. The secondary electrons show the topography and morphology of the sample whereas backscattered electrons are useful in creating contrast in a multiphase sample which helps in the phase detection. The X rays are produced when electrons of the beam interact with electrons present in the orbitals of atoms present in the sample causing their excitation when these excited electrons return to the ground states they emit x rays of fixed wavelength which are characteristic for each element present in the sample. The SEM technique is a non-destructive technique i.e. the sample used in SEM analysis can be used further for repeated analysis.

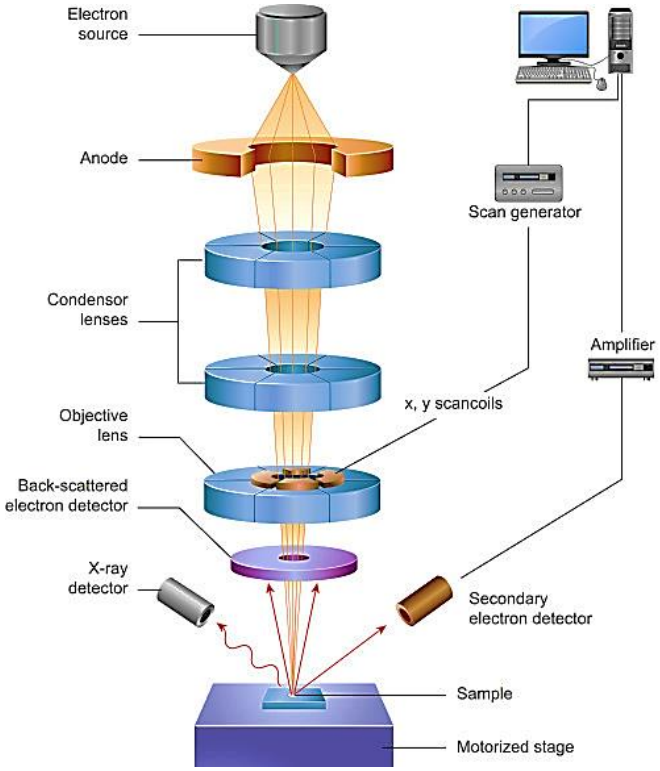

Fig 2.5: Representation of components of the Scanning Electron Microscope. Image produced with permission from [16]

2.4.3 Transmission Electron Microscopy

TEM is an important tool for structural characterization in the field of material science. In this technique, a high-energy beam of electrons is allowed to fall on a very thin layer of the sample and the interaction between the two gives detailed information about the crystal structure and some peculiar features like the presence of grain boundaries and dislocations. The basic principle of a transmission electron microscope and light microscope same but the only difference is that the former uses an electron beam and later one uses light as a source. The optical resolution of TEM is much higher than a light microscope which makes it capable of revealing the finest details of the structure

Working of TEM

A typical electron microscope consists of an electron gun that produces a high-energy beam of electrons using either V-shaped tungsten filament or lanthanum boride crystal as a source. A condenser lens converts the electron beam into a small, thin coherent beam. This beam then falls on the specimen sample. Some part of the beam is transmitted depending upon the thickness of the sample. An objective lens converts it into an image on a phosphor screen or

charge-coupled device (CCD) camera. The image is then magnified by the projector and intermediate lenses. Light is generated when the image strikes with a phosphor screen to make it visible to the user.

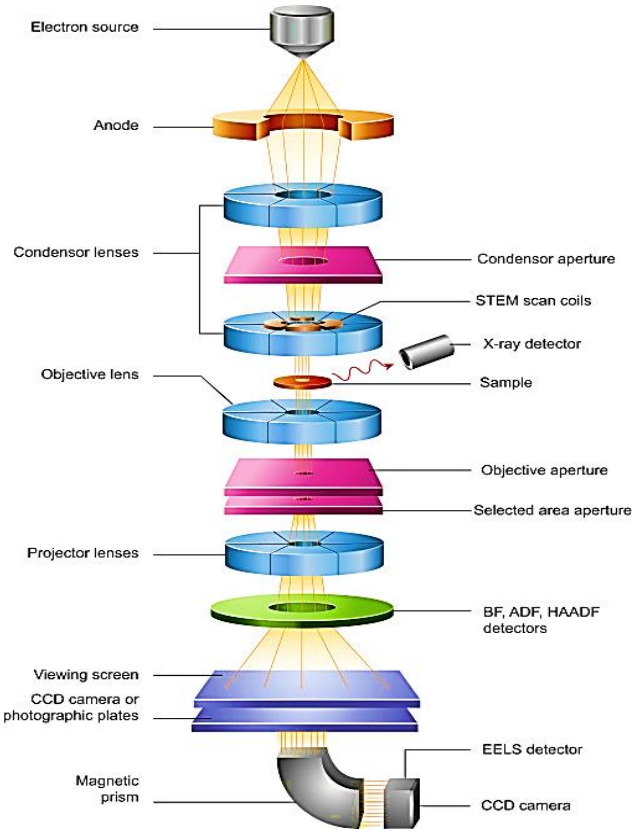

Fig 2.6: Representation of components of Transmission Electron Microscope. Image produced with permission from ref [16]

2.4.4 XPS

X-ray photon electron spectroscopy is a spectroscopic technique that is based on the fundamental phenomenon of the photoelectric effect. This technique is also called Electron Spectroscopy for Chemical Analysis (ESCA). The types of elements, their chemical states, and the overall structure of the material can easily be identified using XPS. Not only the presence of different types of elements as well as the information about the other chemically bonded elements can easily be conquered with the help of this technique. The sample is irradiated by low-energy x-rays (Kα lines of Mg (1.2536 keV) and Al (1.4866 keV) followed by the analysis of energies of emitted electrons. The XPS spectrum is obtained by plotting intensity (no of ejected electrons) with respect to their binding energies. The resulting spectrum shows a set of characteristic peaks that helps in the identification of elements and their chemical states present in the sample under observation.

The kinetic energy (K.E.) of the emitted electrons is expressed as:

$$K.E = h\nu - B.E - \phi s \qquad (2)$$

hν: Energy of the incident photon

B.E: Binding energy of the orbital from where the electron is ejected

Φs: Work function of the spectrometer

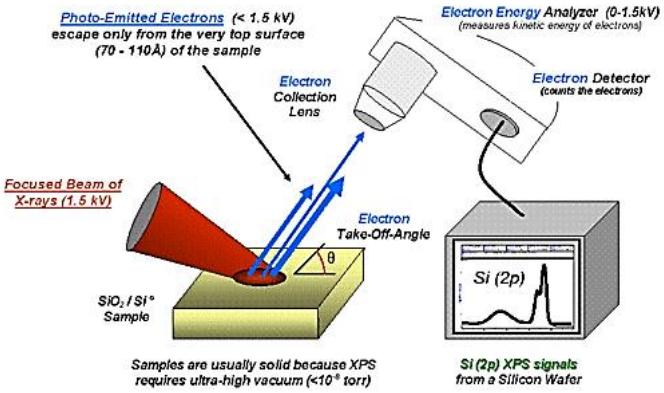

Fig 2.7: Basic components of XPS system (Image taken from Wikipedia)

The energy of the incident photon, work function are known and kinetic energy is measured by the detector which leaves only the binding energy as the unknown factor. Since the electrons in an atom are present in different orbitals thus possess different binding energies. The binding energy is also affected by the chemical environment of the atom. After analyzing the energies of each ejected electron the composition of the material can be easily analyzed.

2.4.5 BET

BET technique is used for the measurement of surface area as well as the pore size, pore volume of the materials. It is based on Brunauer- Emmett- Teller theory that explains the physical adsorption of gasses on the surface of solids. Three scientists Stephen Brunauer, Paul Hugh Emmett, and Edward Teller were the first to give an idea about this theory through an article. This theory is applicable to multilayer physical adsorption of chemically non-reactive gasses such as CO_2, N_2, Ar, etc. Mostly nitrogen gas is preferred as an adsorbate for the adsorption on the surface of solid materials. This theory is the extension of Langmuir theory applied to multilayer adsorption with the following assumptions:

(a) The Adsorption of gas molecules is not limited to the surface only. It can happen in layers infinitely.

(b) The layers of adsorption do not interact with each other.

(c) The Langmuir theory applies to each layer.

Based on these assumptions the BET equation is expressed as

$$\frac{1}{v/[(P_o/P)-1]} = \frac{1}{CV_m} + \frac{C-1}{CV_m} P/P_o \quad (3)$$

Here P and P_0 are the equilibrium and the saturation pressure, v is the adsorbed gas quantity in cm^3/g, v_m is the monolayer adsorbed gas quantity and c is the BET constant, which is expressed by (2):

This theory further suggests that when the adsorption isotherm is plotted at the relative pressure in the range of $0.05 < P / P_0 < 0.35$ a linear relationship is obtained between v / ([(P(o))/P)-1] and P/P_0. From the slope and intercept monolayer adsorbed volume v_m and c can be estimated using the following equations

$$\upsilon_m = \frac{1}{A+I} \quad (4)$$

$$c = \frac{1}{A+I} \quad (5)$$

After this surface area can be calculated as per equation

$$S_{total} = \frac{n_m N s}{V} \quad (6)$$

Apart from calculating surface area using BET analysis, it is also important to estimate the pore size and pore volume. BJH method is used for estimating the pore size and pore volume from adsorption and desorption isotherms using the kelvin model applicable for analysis of only mesopores and small size micropores. The kelvin model assumes that pores have cylindrical shapes and the pore radius is given by the sum of kelvin radius and thickness of the film. The calculations of BJH involve the use of the desorption branch of isotherm when the relative pressure is close to unity.

2.4.6 FTIR

FTIR is a widely used technique for both quantitative as well as qualitative analysis of organic as well as inorganic samples. In this technique, IR radiation is passed through the

sample. A part of infrared radiation is either transmitted or absorbed by the sample. A spectrum is obtained either from transmission or absorption mode displaying the fingerprint of the sample. No two molecules can have the same infrared spectrum. The older spectrometers use the dispersive method which involves the separation of individual frequencies of energy emitted from the spectrometer. Later on, FTIR spectroscopy was developed to solve the issues encountered with dispersive instruments where instead of monochromatic radiation a beam of light having multiple frequencies is shined upon the sample once, and the amount of light absorbed is measured. This is repeated a few times in a short time interval. The data is collected by the computer which works in the background to reveal the absorption at all the wavelengths.

A typical FTIR spectrometer consists of

- Source
- Interferometer
- Sample compartment
- Detector
- Amplifier
- A/D convertor
- Computer

The source generates the IR radiation which passes through the sample through the interferometer; the part of light either absorbed or transmitted reaches the detector. Amplifier and A/D convertor amplify the received signal and convert it into a digital signal which is sent to the computer further where Fourier transform analysis is carried out. The standard protocol adopted for preparing the sample of FTIR is using KBr. The small quantity of solid samples around 1 -2 mg and 100-150 mg of KBr are dried and grounded to a fine powder and further pelletized into thin transparent pellets which are directly used for the measurement. In the case of liquid samples, the liquid is poured between two NaCl pellets. The sample is further locked in the cell with help of skews and measurement is carried out. A gas cell equipped with KBr windows on both sides is used for the measurement of gaseous samples.

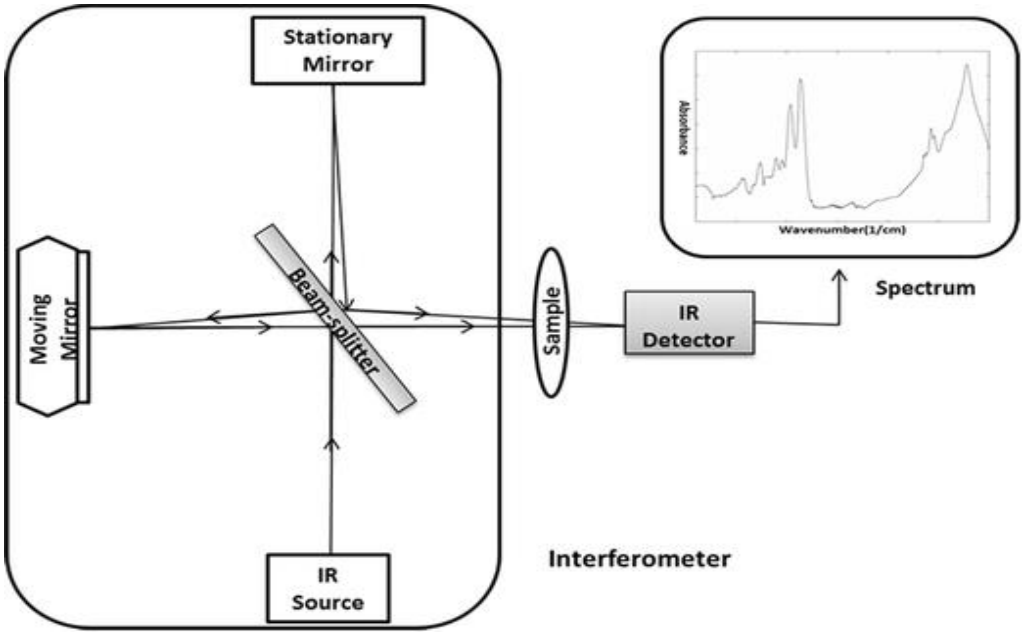

Fig 2.8: Schematic showing components of FTIR spectrometer image reproduced from Ref [17]

2.4.7 TGA

TGA is a quantitative thermal analysis technique where the mass of the sample is monitored as a function of time when it is heated under a steady flow of gas or under changing gas atmosphere in a controlled temperature program which includes steps such as heating, cooling, and isothermal stays [18]. This technique is widely used nowadays by researchers to understand the kinetics, conversions, and mechanisms which involve variation in mass by thermodynamic processes. The changes in the mass are observed due to decomposition of material or due to removal of volatile components.

The TGA analyzer consists of a microbalance attached with a sample plan located inside the furnace equipped with a programmer and controller. Balance weighs the sample in a closed furnace [19]. The sample is loaded either from the top, bottom or side. An inert gas is circulated over the sample at the flow rate of 20-200 ml per minute [20].

Data obtained after the TGA analysis is represented by the graph showing the variation of mass with time. The derivative of the above plot is also shown along with the TGA curve to identify the multiple regions having weight loss.

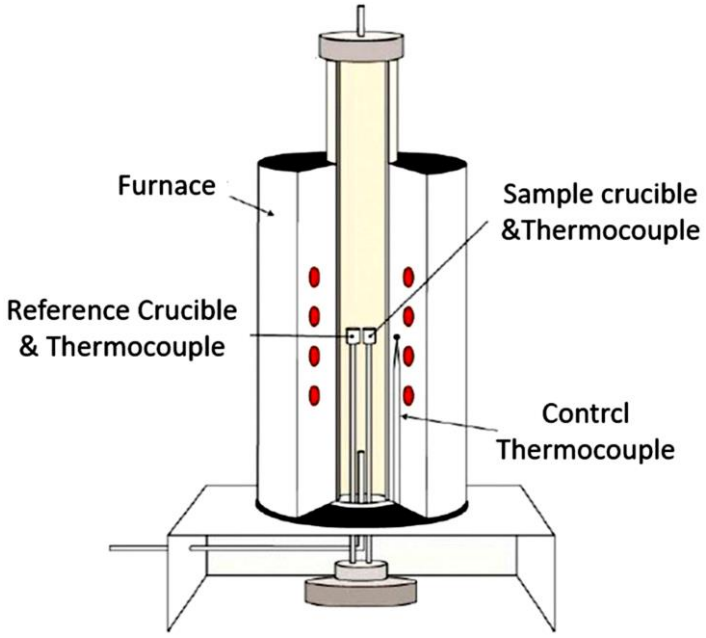

Fig 2.9: Schematic showing components of TGA. Image reproduced from Ref [21]

2.4.8 Atomic Force Microscopy (AFM)

AFM is a specialized microscopy technique that is capable of imaging any kind of surface such as biological samples, glass, and composites[22, 23]. As compared to an electron microscope that portrays a 2D image of a sample AFM is capable of giving a 3D image profile of the same, also their no special requirement of metal or carbon coatings that can modify the sample. The most important thing about AFM is that it does not require an ultra-high vacuum for the operation as in the case of an electron microscope rather it can be operated normally.

AFM contains a sharp tip of 10-20 nm held with the help of a cantilever. Both the tip and cantilever are composed of Si or silicon nitride Si_3N_4. Depending upon the interaction of tip and surface the movement of the tip is observed. Two kinds of modes are used to operate AFM. One is tapping mode in which the cantilever is vibrated over the sample so that there is mere contact of the tip with the surface. Second is the contact mode where there is direct contact between the surface and tip. For imagine purpose tapping mode is advisable while contact mode is used in specialized applications. The atom located at the peak of the tip interacts with the atoms present on the surface. These interactions modulate the frequency of the tip and help in their detection and mapping [24].

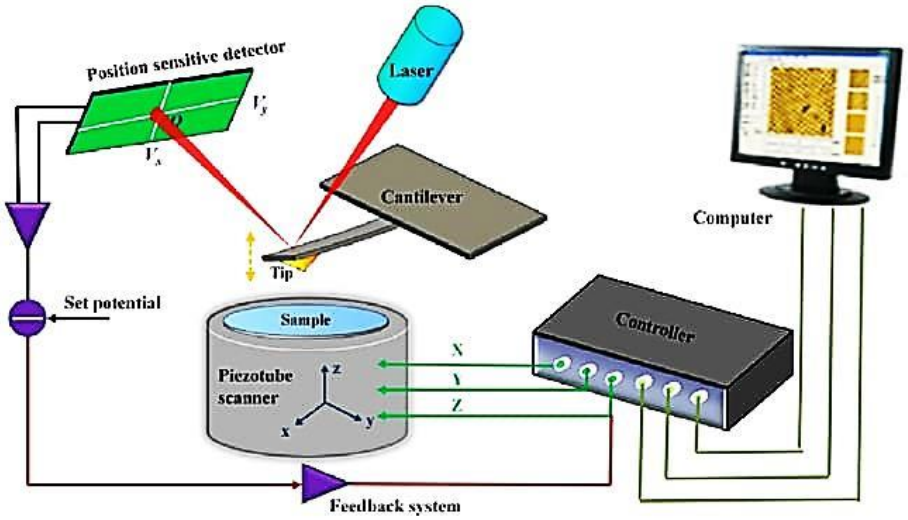

Fig 2.10: Image showing instrumentation of AFM. Fig reproduced from ref [25]

2.5. Electrode Fabrication

After the catalyst synthesis, the electrode of the material is fabricated for checking its performance in the desired application. The steps involved in electrode fabrication are as follows:

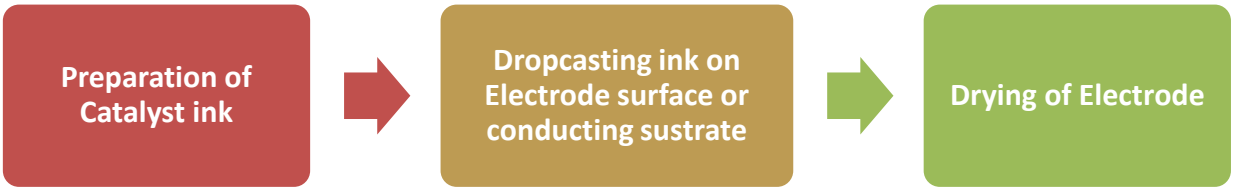

Fig 2.11: Steps involved in electrode fabrication

1) **Preparation of catalyst ink**: The catalyst ink is prepared by dispersing a known amount of catalyst in a particular solvent with the help of a bath Sonicator or probe Sonicator for varying time durations. The solvents used are DMF, Ethanol, Isopropanol, etc. Nafion is also added in ink in a very small amount which helps in adhering of the catalyst particles with the electrode surface.

2) **Drop casting on the electrode/substrate**: Once the ink is prepared known volume of the ink is drop cast on the specified area of conductive substrate or the electrode surface. Commonly used conductive substrates are Nickel foam, Graphite strip, Carbon cloth, titanium mesh, etc. A glassy carbon electrode is widely used in electrochemical studies. It is

important to activate it before using it. Activation of GC surface with micro-sized abrasives is a generally used method. It is very important to maintain clean conditions while polishing. Sonication is often done after polishing the surface but this is usually avoided because repeated sonication can destroy the seal between the carbon layer and outer material. A worthy approach to elude this is vacuum heat treatment [26] and the use of organic solvent [27] for polishing the surface. Both of these hinder the presence of oxygen functionalities on the surface that can interfere with the electron transfer processes [28]. In this thesis polishing kit from CHI is used for polishing of glassy carbon electrode. The polishing kit consists of 1.0-micron alumina powder, 0.3-micron alumina powder, 0.05-micron alumina powder, nylon, and micro cloth polishing pads. The nylon pad is used for 1 micron and 0.3-micron alumina powder and micro cloth is used for 0.05-micron alumina powder. For polishing small amount of alumina powder is placed on the polishing pad, few drops of water are added to make a slurry. Hold the electrode vertically and gently polish with soft hands following 8 patterns for 15-20 seconds. After that, the electrode is washed by holding the stream of water vertically. To assure the extent of activation the peak potential of the Ferro ferry redox couple can be noted using the cyclic voltammetry technique which should come close to 60 mV [29]. High-quality water should be used for carrying out the activation processes. To drain out the excess water from the surface of the electrode soft tissue paper-like Kim wipes should be used.

3) **Drying of electrode**: After drop-casting the ink on the catalyst surface resulting electrode or the substrate is vacuum dried overnight. As a precautionary step, the drying should be done slowly. The use of heating should be avoided because it can damage the electrode surface and cracks may appear in the coating after drying.

2.5.1. Reference Electrode

The choice and selection of the reference electrode and the counter electrode are really important while performing electrochemical measurements to avoid inaccuracy in the results. The most reliable reference electrode is a reversible hydrogen electrode. All the potentials measured with respect to other reference electrodes need to be converted w.r.t to R.H.E. most commonly used reference electrodes are

1) Saturated calomel electrode (SCE): This electrode is based on the half-cell reaction $Hg_2Cl_2 + 2e^- \longrightarrow 2Hg + 2Cl^-$ in saturated KCl solution with E^o value 0.241V.

2) Silver / Silver electrode (Ag/AgCl): This electrode is based on half-cell reaction $AgCl + e^- \longrightarrow Ag + Cl^-$ in defined concentration of KCl.

While using the above reference electrodes some vital considerations need to be considered very precisely such as concentration of electrolyte solution, Cl^- leaching[30], and intervention from the alkaline electrolyte. Potential of Ag/AgCl electrode in saturated KCl is 0.197 w.r.t to S.H.E [31] and it is 0.288 V in 0.1 M KCl solution[32] w.r.t to S.H.E at 25 ^oC. Interference from Cl^- ions and hydroxyl ion in alkaline medium[33] can be avoided either by modifying the cell design or by replacing the glass frit with the Nafion film or alkaline stable frit.

It is very necessary to report the potentials w.r.t to R.H.E because the potential of all reference electrodes varies with pH creating difficulties in comparison of results when different electrolytes are used. Thus the potential measured with any of the above reference electrodes should be transformed to the R.H.E scale by expression

$$E_{R.H.E} \longrightarrow E_{S.H.E} + 2.303\ RT/F$$

$E_{S.H.E}$ = Potential of reference electrode w.r.t to S.H.E

R = Universal Gas constant

F= Faradays constant

T= Temperature

From the above equation, it can be conveyed that the effect of pH is which eases the comparison of activities in different electrolyte mediums.

2.5.2. Counter Electrode

There is a huge significance of counter electrode therefore it should be selected wisely. The counter should be such that it should be able to transfer electrons to the working electrode quickly for a particular reaction. It should be properly positioned placed to provide a consistent electric field across the working and counter electrode. Lastly, it should not hamper the activity measurements. Platinum full fill all these requirements as a counter electrode as it provides sufficiently high current densities but the main loophole while using this is that it dissolves in the electrolyte either due to oxidation or reduction of PtOx and gets electrodeposited on the working electrode [34]. Even with slight amount of platinum deposited

on the surface of the working electrode may induce positive change in the activity leading to anomalous results [35]. Thus enhancement in the activity which is observed after the prolonged testing originates by-products from the counter electrode. Such kind of considerations can be avoided by separating the compartments of working and counter electrodes or replacing Pt electrodes with carbon-based graphite electrodes [34]. Though graphite electrode can remove ambiguity regarding platinum deposition it liberates CO and CO_2 in oxidizing conditions [36] and impurities might seep into the electrolyte thus the possibility of alteration in the activity from graphite should also be kept in mind.

2.6 Electrode processes

The field of electrochemistry deals with the processes that involve charge transfer and charge separation in the solutions or at the electrode-electrolyte interfaces. After the first experimental application of electrochemistry, a huge variety of electrochemical techniques are developed. In most of the techniques, we study the relationship between current and potential for the reactions taking place at the electrode and analyze them whereas in some we don't study the current potential relation but it serves as the basis of techniques. To have a deep and sound understanding of electrochemical techniques, it is necessary to study the basics of electrode reactions and the properties of the electrode-electrolyte interface. On the surface of the electrode, two kinds of processes are usually observed. The first type involves the movement of the electrons across the interface. This causes the oxidation and reduction of redox species present in the solution at certain potentials on the surface of electrodes. These reactions are monitored using Faraday's laws thus they are given the name of Faradaic processes. Sometimes at a specific range of potentials, the charge transfer reactions are banned because they involve thermodynamically or kinetically unfavorable reactions however some other processes involving the adsorption or desorption of reaction intermediates or ions can take place. Such processes are known as Non-faradaic processes. The reactions taking place on the electrode are a mixture of both faradaic and non-faradaic processes. Practically an electrochemical experiment is visualized in the way that a perturbation is applied to the system and the response is recorded. The understanding and analysis of electrode reactions are quite difficult because it's a group of heterogeneous reactions taking place only on the electrode-electrolyte interface. The rate of reaction is

highly dependent on the mass transfer to or from the electrode in addition to kinetic variables. It is usually expressed as:

$$\text{Rate (mole / s/cm}^2) = \frac{j}{nF} \qquad (7)$$

Here j is the current density in A/cm^2

Normally as a usual approach potential to study the electrode reaction potential is applied and the corresponding current is determined in the form of i-E curves (called polarization curves). Reactions proceed at certain fixed thermodynamic electrode potentials in such cases potential serves as an important reference point. The shift of electrode potentials from this actual value on passage of faradaic current is called polarization is often depicted by the term overpotential expressed as

$$\eta = E - E_{eq} \qquad (8)$$

Ideally, an electrochemical cell consists of two electrodes and an electrolyte solution. In the actual cell, the reaction takes place only at one electrode of interest called a working electrode and the other electrode a standard non-polarizable electrode having known potential called a reference electrode. This arrangement is called a two-electrode setup. Experimentally it has been observed that when the potential is measured against a standard non-polarizable electrode voltage drop given by iR_s (called as the ohmic potential drop is always added up where R_s is solution resistance across the electrodes. It should be kept in mind that this ohmic drop should not be considered as a part of over potential because it is a characteristic of the solution not a part of electrode reaction. Normally when this ohmic drop is a small two-electrode system can be used to collect polarization curves but when this ohmic drop is very high especially in the case of highly resistive non-aqueous solvents three electrodes are set up is preferred where a counter electrode is used along with the reference and working electrode. The counter electrode should be such that it does not produce species on passage of current that can interfere with the reactions taking place at the working electrode. It is separated from the working electrode either by placing it in a separate compartment or positioned in a sintered glass. The potential of the working electrode is monitored with respect to the reference electrode. Even with this arrangement, not all iR_s are removed thus it should always be considered while reporting the overpotential.

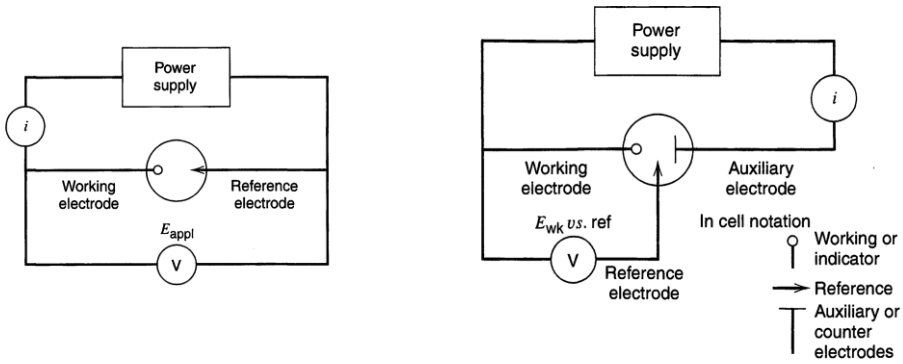

Fig 2.12: Schematic representation of two and three-electrode system

From equation 7, it can interpret that rate of reaction taking place at the electrode is controlled by the current. It also has been studied that current flows only at a certain range of potentials for a particular electrode reaction. Thus it is highly controlled by the potential. Therefore it is important to study the dependency of rate constants on the potential.

2.7 Electrode kinetics

Butler Volmer equation is the most fundamental equation on electrochemical kinetics [37]. It helps to understand how electric current obtained from an electrode is controlled by applied potential by a simple redox reaction by assuming that both the cathodic and anodic reactions are taking place at the same electrode. This equation is given as:

$J = j_o . \{\exp [\frac{\alpha_a \, z \, F)}{RT} (E\text{-}Eeq) - \exp [-\frac{\alpha_c \, z \, F)}{RT} (E\text{-}Eeq)\}$ (8)

J= Current density (A/cm^2)

J_0= Exchange current density (A/cm2)

F= Faraday constant (C/mole)

R= Universal gas constant

T = Absolute temperature (K)

E= Electrode potential (V)

E_{eq}= Equilibrium Potential (V)

α_a = Anodic charge transfer coefficient

α_c = Cathodic charge coefficient

2.8 Electrochemical techniques

A collection of electrochemical techniques are used for the systematic analysis of hydrogen evolution and oxygen evolution catalysis. These techniques are displayed below and discussed in detail in subsequent sections.

Fig 2:13 Types of Electrochemical techniques

2.8.1 Cyclic Voltammetry and Linear sweep voltammetry:

Both linear sweep voltammetry and cyclic voltammetry are two basic types of voltammetry techniques[38]. In linear sweep voltammetry, the potential between the working and reference electrode is changed linearly with the time the current is measured at the working electrode. The rate at which the potential changes with time is called as scan rate. When the direction of this potential scan is reversed back i.e. once the final set potential is attained the potential is again reverted to the initial set potential then it is called cyclic voltammetry. In other words, we can say that CV is the combination of two LSVs both in the forward and backward direction. Both of these techniques give primary information about the quality of materials designed for carrying out electrocatalysis in terms of current density and overpotential. By comparing the data obtained from CV and LSV curves with that of benchmark catalysts it is easy to get an idea about the efficiency of materials. CV and LSV studies performed for multiple cycles can also disclose the stability[39]. The electrochemical surface is often estimated with the help of cyclic voltammetry measurements performed in nor faradaic region at multiple scan rates [40]. After performing the measurements $\Delta j/2$ is noted down and plotted w.r.t to scan rate. After linear fitting of the above plot, C_{dl} is calculated which is used to evaluate ECSA using the equation i.e. ECSA= Cdl/Cs, where Cs is the specific capacitance of the material [41].

2.8.2. Impedance Spectroscopy:

EIS spectroscopy is a very important analytical tool for studying the materials employed for energy-related applications [42]. In this technique, AC potential is applied and modulated with

time at a small amplitude at a particular range of frequency (1 MHz to 10 kHz). The obtained current response is also in the sinusoidal form but lags by a phase angle φ. Once the data is collected it is often graphed either in the form of a Nyquist plot or bode plot. The EIS data is further fitted using equivalent circuit models which are the combinations of different kinds of elements such as resistors, capacitors, inductors, and diffusion elements to extract evocative information from the recorded data [43]. When it comes to HER and OER catalysis the impedance technique is highly useful in estimating the charge transfer resistance as well the capacitive behavior of the material [44]. The value of charge transfer resistance often reflects the barrier at the electrode-electrolyte interface for electron charge transfer. The smaller is the value of charge transfer resistance more superior will be the activity of the catalyst.

2.8.3 Chronopotentiometry and Chronoamperometry:

Chronopotentiometry is the technique in which constant current is applied and the change in potential with the duration of time is observed on other hand in Chronoamperometry at a fixed potential (the potential at which an electrochemical reaction occurs) the response of change in current with time is noted. Chronopotentiometery finds its use in charge-discharge experiments as well in electrodeposition. Chronoamperometry holds a special place in characterization techniques for HER and OER catalysis since the long-term stability of the materials under given experimental conditions is usually evaluated using this technique along with LSV and CV.

References

1. G. Yang and S.-J. Park, *Materials*, 2019, **12**, 1177.
2. O. H. Duparc, *International Journal of Materials Research*, 2007, **98**, 651-654.
3. R. J. White, R. Luque, V. L. Budarin, J. H. Clark, and D. J. Macquarrie, *Chemical Society Reviews*, 2009, **38**, 481-494.
4. N. Rajput, *International Journal of Advances in Engineering & Technology*, 2015, **7**, 1806.
5. M. Sheikholeslami, S. Soleimani, and D. Ganji, *Journal of Molecular Liquids*, 2016, **213**, 153-161.
6. R. Melo, F. Silva, K. Moura, A. De Menezes and F. Sinfrônio, *Journal of Magnetism and Magnetic Materials*, 2015, **381**, 109-115.

7. Z. Li, Y. Chen, J.-F. Li, H. Chen, L. Wang, S. Zheng, and G. Lu, *Nano Energy*, 2016, **28**, 78-86.

8. G. W. Morey and P. Niggli, *Journal of the American Chemical Society*, 1913, **35**, 1086-1130.

9. M. Yoshimura and H. Suda, in *Hydroxyapatite and related materials*, CRC Press, 2017, pp. 45-72.

10. G. Dell'Agli, A. Colantuono and G. Mascolo, *Solid State Ionics*, 1999, **123**, 87-94.

11. H. Cheng, J. Ma, Z. Zhao, and L. Qi, *Chemistry of Materials*, 1995, **7**, 663-671.

12. M. Roble, S. Rojas, R. Wheatley, S. Wallentowitz, A. Cabrera and D. Diaz-Droguett, *Journal of Solid State Chemistry*, 2019, **271**, 314-325.

13. R. Rai, Z. Ahmed, R. Kumar, R. L. Kumawat, K. Chordiya, T. Maruyama, M. E. Ali and V. Bagchi, *ACS omega*, 2018, **3**, 15112-15118.

14. D. C. Marcano, D. V. Kosynkin, J. M. Berlin, A. Sinitskii, Z. Sun, A. Slesarev, L. B. Alemany, W. Lu, and J. M. Tour, *ACS nano*, 2010, **4**, 4806-4814.

15. R. Kroon, *South African Journal of Science*, 2013, **109**, 1-2.

16. B. J. Inkson, in *Materials Characterization Using Nondestructive Evaluation (NDE) Methods*, eds. G. Hübschen, I. Altpeter, R. Tschuncky, and H.-G. Herrmann, Woodhead Publishing, 2016, pp. 17-43.

17. F. Faghihzadeh, N. M. Anaya, L. A. Schifman and V. Oyanedel-Craver, *Nanotechnology for Environmental Engineering*, 2016, **1**, 1.

18. S. Vyazovkin, A. K. Burnham, J. M. Criado, L. A. Pérez-Maqueda, C. Popescu and N. Sbirrazzuoli, *Thermochimica acta*, 2011, **520**, 1-19.

19. R. B. Prime, H. E. Bair, S. Vyazovkin, P. K. Gallagher and A. Riga, *Thermal analysis of polymers: Fundamentals and applications*, 2009, 241-317.

20. N. Saadatkhah, A. Carillo Garcia, S. Ackermann, P. Leclerc, M. Latifi, S. Samih, G. S. Patience and J. Chaouki, *The Canadian Journal of Chemical Engineering*, 2020, **98**, 34-43.

21. W. Li, X. Y. Tan, Y. M. Park, D. C. Shin, D. W. Kim, and T. G. Kim, *Frontiers in Materials*, 2020, **7**, 201.

22. G. Binnig, C. F. Quate, and C. Gerber, *Physical review letters*, 1986, **56**, 930.

23. F. J. Giessibl, *Reviews of modern physics*, 2003, **75**, 949.

24. H.-J. Butt, B. Cappella, and M. Kappl, *Surface science reports*, 2005, **59**, 1-152.
25. D. Guo, G. Xie, and J. Luo, *Journal of Physics D: applied physics*, 2013, **47**, 013001.
26. D. T. Fagan, I. F. Hu and T. Kuwana, *Analytical chemistry*, 1985, **57**, 2759-2763.
27. P. Chen and R. L. McCreery, *Analytical Chemistry*, 1996, **68**, 3958-3965.
28. S. Ranganathan, T.-C. Kuo and R. L. McCreery, *Analytical chemistry*, 1999, **71**, 3574-3580.
29. N. Wiener, *Invention: The care and feeding of ideas*, MIT Press, 1994.
30. G. K. Wiberg, K. J. Mayrhofer and M. Arenz, *Fuel cells*, 2010, **10**, 575-581.
31. A. J. Bard and L. R. Faulkner, *Electrochemical methods*, 2001, **2**, 580-632.
32. M. B. SHIMKIN, *SCIENCE*, **140**, 1366.
33. G. Schweitzer and L. Pesterfield, *New York*, 2010.
34. R. Wei, M. Fang, G. Dong, and J. C. Ho, *Sci. Bull*, 2017, **62**, 971-973.
35. J. Chen, C. Jones, S. Linic and V. Stamenkovic, *Journal*, 2017.
36. S. J. Ashton and M. Arenz, *Journal of Power Sources*, 2012, **217**, 392-399.
37. D. Aikens, *Journal*, 1983.
38. E. Parameters, *Princet. Appl. Res*, 1-15.
39. A. Méry, S. Rousselot, D. Lepage and M. Dollé, *Materials*, 2021, **14**, 3840.
40. B. Zhang, Y. H. Lui, L. Zhou, X. Tang, and S. Hu, *Journal of Materials Chemistry A*, 2017, **5**, 13329-13335.
41. T. Binninger, E. Fabbri, R. Kötz and T. J. Schmidt, *Journal of The Electrochemical Society*, 2013, **161**, H121-H128.
42. A. Brahme, *Comprehensive biomedical physics*, Newnes, 2014.
43. A. R. Bredar, A. L. Chown, A. R. Burton and B. H. Farnum, *ACS Applied Energy Materials*, 2020, **3**, 66-98.
44. H. Yuan, S. Wang, X. Gu, B. Tang, J. Li and X. Wang, *Journal of Materials Chemistry A*, 2019, **7**, 19554-19564.

Chapter 3

Environmentally Benign Metal-Free Reduction of GO Using Molecular Hydrogen: A Mechanistic Insight.

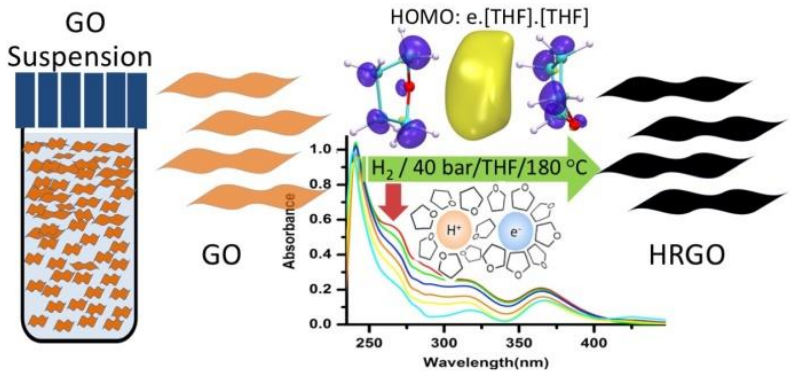

ABSTRACT: *A simple yet effective methodology to obtain high-quality reduced graphene oxide (RGO) using a tetrahydrofuran suspension of GO under hydrogen at moderate pressure has been demonstrated. The extent of reduction as a function of the pressure of hydrogen gas, temperature, and time was studied, where the abstraction of oxygen is achievable with the least mutilation of C-sp^2 bonds, hence upholding the integrity of the graphene sheet. Herein, the formation of a short-lived species is proposed, which is possibly responsible for such reduction. A detailed theoretical calculation along with in situ UV−visible experiments reveals the existence of a transient solvated electron species in the reaction medium. The hydrogen RGO (HRGO) achieved a C/Atomic ratio of 11.3. The conductivity measurements show that HRGO reached as high as 934 S/m, which indicates a high quality of RGO. The process is hassle-free, environmentally benign, and can be scaled up effortlessly without compromising the quality of the material.*

3.1 Introduction

Reduced graphene oxide (RGO) is one of the most intensively studied derivatives of graphene [1–3]. Ever since the extraordinary properties of graphene (e.g., mechanical, electrical, thermal, and optical properties as well as their high specific surface areas) were discovered, graphene and its derivatives have been at the forefront of material research till today [4,5]. RGO is one of the most promising materials used instead of graphene. The most common route used for the mass production of graphene is to reduce GO chemically into RGO. The process is well suited to versatile chemical functionalization and involves low material cost. Simplicity and suitability for large-scale production are among the few strong reasons for extensive use of this method [6,7]. The challenges associated with the chemical route were inadequate reduction, non-reproducibility, and formation of undesired defects. To date, the chemical reduction of GO has been performed with several reducing agents such as $NaBH_4$ [8], hydrazine, and its derivatives[9],[10] hydroquinone [11] hydriodic acids (HI) [12,13], sulfur-containing compounds [14], metal powders [15], and so forth. Among them, metal powders are the most powerful reducing agents achieving a high C/O atomic ratio of RGO. Nascent hydrogen, which is considered to be especially reactive and produced from the reaction of metals, such as Mg, Al, Fe, and Zn, with an acid or amphoteric metals (Al and Zn) and their alloys with the alkali solution, has been used by many groups for the reduction of GO [16–19]. However, achieving a high C/O ratio does not ensure a better quality RGO [20]. Herein, we have explored a new synthetic methodology and its mechanistic insights, which can reroute the procedure for the bulk production of RGO. Instances of mere diatomic hydrogen for the reduction of GO in tetrahydrofuran (THF) without a metal catalyst would be a new addition to the literature. Herein, we report a simple methodology to synthesize RGO under hydrogen in THF, which can be scaled up effortlessly without compromising the quality of the product. The procedure involves exposure of GO suspension in THF, to diatomic hydrogen at moderate pressure and temperature. The extent of reduction reaches a maximum at a pressure of 40 bars at 180 °C. The reaction is carried out in a stainless steel pressure vessel, resulting in excellent quality RGO. The method of extraction is very facile and imparts zero Impurity, and hence, no purification is needed after reduction. The hydrogen RGO (HRGO) using hydrogen achieves a C/O atomic ratio higher than 11.3 and the ID/IG ratio obtained higher than 1.6. It should be noted that a controlled experiment was carried out where THF dispersions of graphene oxide were reduced in an argon atmosphere by keeping the reaction conditions intact, i.e. (180 °C and 40 bar). The progress of the above reaction was determined

by using FTIR spectroscopy of the sample obtained at regular intervals of time. FTIR spectra were recorded on Carry 660 FTIR spectrometer from 400 cm $^{-1}$- 4000 cm^{-1}. The HRGO samples were pelletized into thin discs for recording the spectra. The FTIR spectra of the GO under the same reaction condition in argon is compared with GO (Graphene oxide) and HRGO (RGO reduced under hydrogen) as shown in Fig (3.1). From the figure, it can be seen that the GO is not reduced in argon atmosphere thus confirming the role of hydrogen in reduction under this reaction condition. A detailed theoretical calculation reveals the possibility of formation of solvated electrons in such reaction, which is shown for the first time.

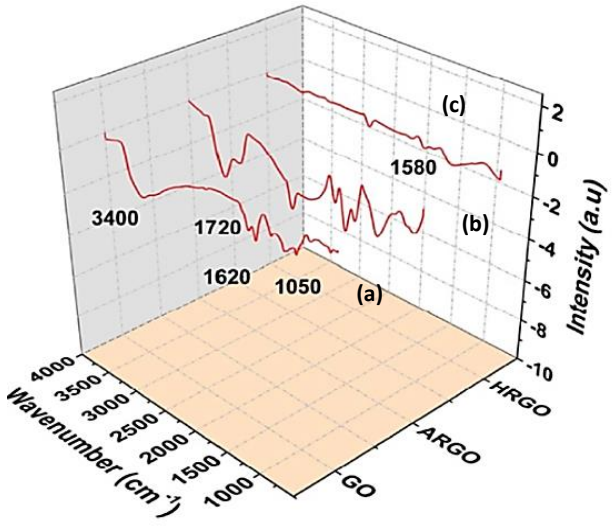

Fig 3.1: FTIR spectra of (a) Graphene oxide (b) ARGO (GO reduced in argon) (c) HRGO

3.2 Experimental Section

3.2.1 Materials

Major chemicals such as THF, hydrogen peroxide (H_2O_2), potassium permanganate ($KMnO_4$), sulphuric acid (H_2SO_4), and hydrochloric acid were purchased from Merck Chemicals unless mentioned otherwise and used as received without further purification. Graphite powder (<20 μm) was purchased from Sigma Aldrich.

3.2.2 Synthesis of Reduced Graphene oxide

GO was synthesized using an improved method as reported in the previous literature [21]. Reduction of GO was carried out in a pressure reactor autoclave using hydrogen gas under various pressures and temperatures to optimize the reaction condition. In brief, 50 mg of GO

was dispersed in 35 mL of THF. The above dispersion was then transferred to a 50 mL reactor vessel equipped with pressure and temperature sensors and heated to 180°C under H_2 (40 bar) for 2 h. The obtained reaction mixture was then centrifuged at 7000 rpm and washed with distilled water and acetone. The dispersion was then filtered using a 0.47 μm poly (tetrafluoroethylene) membrane, and the resulting solid was vacuum dried for 24 h and characterized further.

3.2.3 Characterizations

Powder X-ray diffraction (PXRD) of the resulting GO and RGO was carried out with Bruker Eco D8 advance with Cu Kα radiation (λ = 1.54056 Å). The data were collected from 10˚< 2θ< 50˚ with an increment of 0.019˚ Brunauer−Emmett−Teller (BET) surface area analysis was done with Autosorb IQ Qunatchrome instrument. UV−vis absorption spectra were recorded using a UV-2600 spectrophotometer (Shimadzu). TGA was carried out using STA-8000 (Perkin Elmer) under a nitrogen atmosphere at a scan rate of 5 °C/min. Atomic Force Microscopy was done with Bruker Multimode 8 AFM using taping mode. A very dilute uniform dispersion of HRGO (1mg/ml) in ethanol was obtained using Labsonic LBS2-10 BATH Sonicator for 60 min. An aliquot of 5 ul was drop cast on a clean silicon substrate (100) and air-dried. All the AFM images and the average height profile were analyzed by the Nano scope Analysis Software (Bruker). X-ray photoelectron spectroscopy (XPS, EscaLab: 220-IXL) measurements were performed with Mg-Ka nonmonochromated X-ray beam having photon energy 1253.6 eV (chamber pressure 6 5. 10 10 torrs). FTIR spectra were recorded on Carry 660 FTIR spectrometer from 400 cm $^{-1}$- 4000 cm^{-1}. The HRGO samples were pelletized into thin discs for recording the spectra. XRD measurements were done with Bruker Eco D8 advance X-Ray Powder Diffractometer using Ni filtered with Cu Kα radiation (λ=1.54056 °A). The data were collected from 10˚< 2θ< 50˚ with an increment of 0.019˚. WITEC Raman spectrometer with 532 nm laser was used to record the Raman spectra of GO, HRGO_1, and HRGO_2. SEM was done using JEOL 7600F FESEM equipped with an energy dispersive X-ray diffractometer. TEM was done using JEM -2100 TEM operated at 200 kV. For qualitative as well quantitative analysis GC-MS studies were done using GCMS-QP2010 Ultra Gas Chromatograph Mass Spectrometer (Shimadzu Corp 75520). The product profile was further quantified by the Response factor (R.F value) calculated using Dodecanese as an Internal Standard (I.S). The response factor of each product was calculated using the following formula.

$$\text{Response factor (R.F)} = \frac{\text{Peak area of product X Conc of I.S}}{\text{Peak area of I.S X Conc of product}}$$

3.2.4 Electrochemical measurements

Electrochemical measurements were carried out with an Autolab multichannel PGSTAT 204M electrochemical workstation using a three-electrode configuration involving platinum and Ag/AgCl as counter and reference electrodes, respectively. A glassy carbon electrode (3 mm diameter) coated with HRGO ink was used as a working electrode. A homogeneous ink was prepared by dispersing HRGO in dimethylformamide (1 mg/mL) by ultra-sonication for 2 hours and 10 μL of the above ink was drop cast on the glassy carbon electrode. It was vacuum dried and 5 μL of 5% Nafion solution was drop cast on the electrode surface, followed by further drying for 12 h. CV measurements were done in the potential window of (0 to 1 V) at various scan rates. GCD tests were also done in a similar potential window at various current densities ranging from 0.5, 1, 2, 4, and 6 A/g. All the measurements were done in an Argon purged system containing 1 M Na_2SO_4 as an electrolyte. The specific capacitance, C (F g−1), of the electrode material was calculated from the following equation:

$$C = \frac{I\,\Delta t}{m\Delta V} \qquad (1)$$

Where I (A) is the discharge current, Δt is the discharge time, ΔV is the potential window, and m (g) is the active mass. EIS was performed over a frequency range from 0.01 Hz to 100 kHz at an open-circuit potential with an ac perturbation of 5 mV

3.2.5 Computation Details

DFT-based AIMD simulations were performed at a finite pressure and temperature (1 atm & 400 K), and a 1 ps AIMD trajectory was generated to investigate the formation of the transient species. The molecular geometries were optimized using hybrid B3LYP functional and def2-TZVP basis sets. The TD-DFT calculations were performed to obtain electronic spectra by applying a long-range correlation including a hybrid exchange−correlation functional using the Coulomb-attenuating (CAMB3LYP) method [22]. An implicit solvation model such as the conductor-like polarizable continuum model was also adopted to incorporate the solvation effect in electronic spectra calculations (see Supporting Information S4). All the calculations were performed using VASP and ORCA quantum chemical codes [23].

3.3 Results and Discussion

The characterization and properties measurement of the obtained products were done using several techniques as mentioned in the subsequent sections. X-Ray Powder Diffraction of the resulting GO and RGO were carried out with Bruker Eco D8 advance, Cu Kα radiation (λ=1.54056 Å). The characteristic peak of graphite appears at 2Θ = 26.58° for the (002) plane. After the introduction of oxygen functionalities in the graphitic lattice, the characteristic peak of graphite disappears and a new peak arises at 2Θ =10.3°corresponding to (001) plane of graphene oxide and also the interlayer distance increased to 7.74 A°. The confirmation of the reduction of graphene oxide to reduced graphene oxide is further approved by the appearance of a broad peak at 2Θ = 23.5° in HRGO. The interlayer distance is 3.5A° which is due to remaining functional groups and structural defects Fig (3.2).

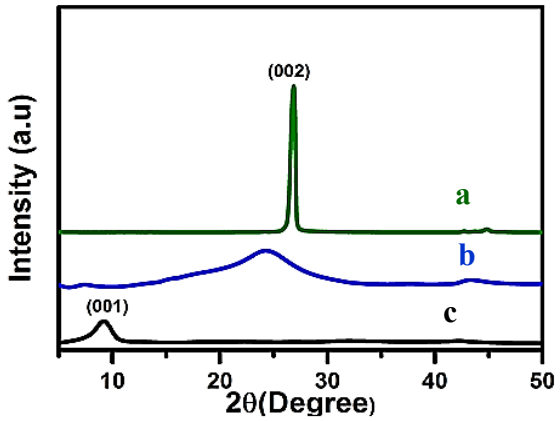

Fig 3.2: PXRD of (a) Graphite (b) HRGO (c) GO

The progress of reduction of graphene oxide using diatomic hydrogen was monitored by recording the UV–visible absorption spectra Fig (3.3) of RGO as a function of time. UV-vis absorption spectra were recorded using a UV-2600 spectrophotometer (Shimadzu). GO shows a maximum absorption peak at 232 nm which was attributed to the π–π* transitions of the aromatic C=C bonds and a weak shoulder at 300 nm due to n–π* transitions of C=O bonds. After complete reduction, a redshift of this characteristic peak was observed at 270.9 nm for C=C [24]. During the process of reduction, the optical absorption of RGO should have had increased as the intensity of UV–visible spectra is directly proportional to the concentration of the solute. But owing to the hydrophobic nature of the RGO, the intensity decreases as it shows the minimum amount which can form a stable dispersion of RGO in water.

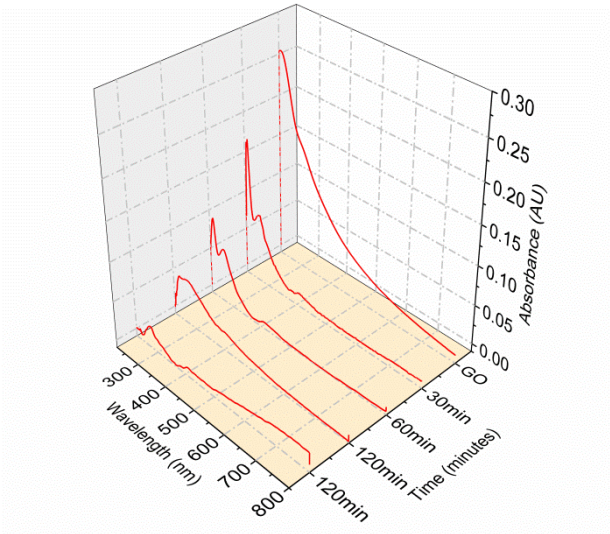

Fig. 3.3: UV-vis spectrum of GO, RGO at 30 min, RGO at 60 min, and RGO at 120 minutes formed in the reaction respectively.

The progress of reduction was also monitored using FTIR and Raman. All the plots for reduction reactions shown in Fig (3.4a) & (3.4b) were performed at 40 bar of H_2 pressure. The peaks Fig (3.4a) showing oxygen functionality almost vanishes at a 2-hour reaction and another peak generates at around 1578 cm^{-1} for the formation of C=C bonds. The degree of removal of oxygen functionalities of GO at different intervals of time can be observed in the plots shown below Fig (3.4a). Peak intensities corresponding to the O–H stretching (3400 cm^{-1}) and the vibrations for O–H deformation (1410 cm-1) were decreased gradually. Peaks intensities corresponding to the stretching of oxygen functionalities such as >C=O (1720 cm^{-1}), epoxy >C–O (1226 cm-1), carboxylic >C–O (1320–1210 cm^{-1}), and alkoxy C–O (1050 cm^{-1}) were also observed to decrease during the progress of the reaction, whereas C = C stretching vibration peaks for the pristine GO were detected at ca.1600 cm^{-1}, which is shifted to 1578 cm^{-1} for RGO's as reported by Y. Fang et al. The Raman spectra showing the D band and G band of GO were shifted to 1336 cm^{-1} and 1571 cm^{-1}, respectively, after its chemical reduction. The intensity ratio of the D and G bands, I_D/I_G, increases with time as depicted in Fig (3.4b). Such enhancement in the intensity ratio is attributed to the increased sp^2 domains in the system [25]. The thermal stability of GO and RGO were examined by TGA Fig (3.4c). GO and RGO showed no significant weight loss near 100 °C, as the samples were completely dried before testing to eliminate the influence of absorbed moisture on the test results. GO exhibits two steps of degradation; the first step commences at 175°C due to the loss of hydroxyl, epoxy functional groups, and remaining water molecules. The second step degradation (450–550 °C) involves the pyrolysis of the remaining oxygen-containing groups

as well as the burning of ring carbon. RGO exhibits only a 7–9 wt% loss up to 250°C, which was much lower than that of the GO, indicating a significantly decreased amount of oxygenated functional groups [24].

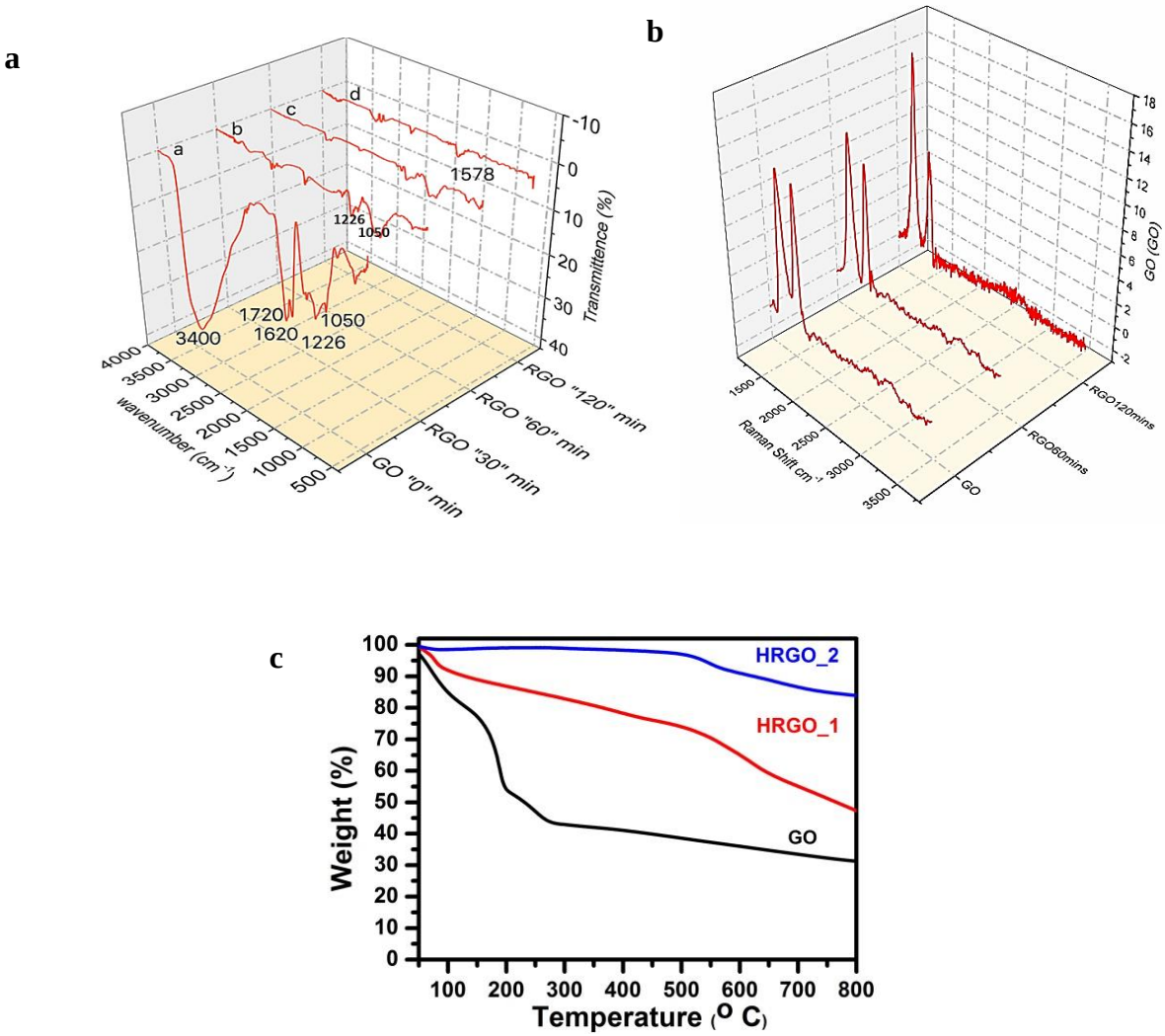

Fig 3.4: (a) Showing FTIR spectra of GO at different intervals of time shows the progress of the reaction. (b) Raman spectra of GO, RGO at 60 min reduction and RGO at 120-minute reduction respectively (c) TGA profile of GO, RGO@20 bar of H_2 (HRGO_1) and RGO @ 40 bar of H_2 (HRGO_2)

Further, the morphology was studied using TEM and SEM. FESEM image shows that HRGOs consisted of folded and wrinkled sheets randomly aggregated to form a disordered solid Fig (3.5b). The visual observation suggests that partial crystallinity of the HRGO sheets is achieved which depends on the extent of reduction (Shown SAED Fig

3.5d Inset). The more reduced HRGO had more folded and wrinkled sheets. Furthermore, the HRGOs so obtained were very clean, without residual metal or salt particles Fig (3.5c).

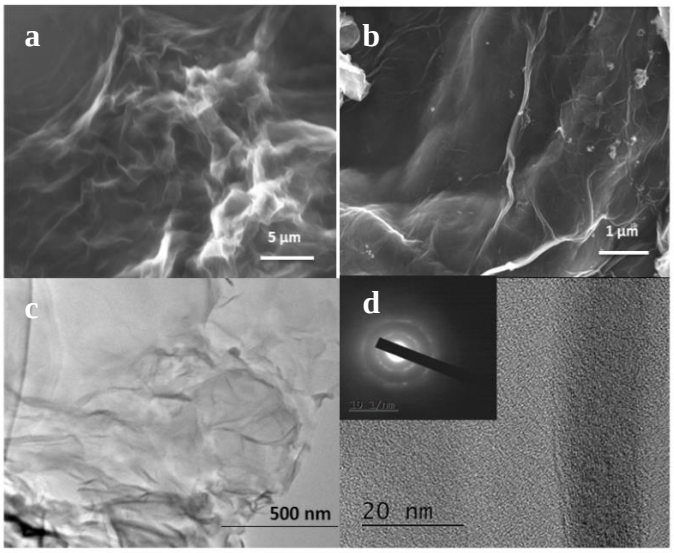

Fig 3.5 (a) shows SEM image of GO; (b), (c) & (d) are FESEM, TEM, and HRTEM images of HRGO/THF in 120 min reaction at 180 °C and 40 bar H_2. Inset in Fig.3.5d shows the SAED pattern of HRGO.

Analysis of BET isotherm of HRGO Fig (3.6) shows the presence of hysteresis loops at the middle. As evident from the BJH pore size distribution shown in the inset, there is a presence of micropores of size falling between 0 -1.7 nm and mesopores ranging from 2-20 nm. The specific surface as calculated from the isotherm is 709 m^2/g which is indicative of the desired parameter known for RGO. Availability of both micropores and mesopores pores proves the worth of hydrogen-reduced graphene oxide.

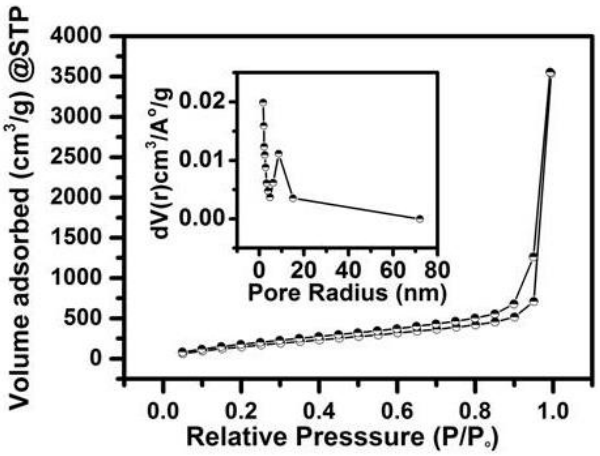

Fig 3.6: BET Plot of HRGO with inset showing BJH pore size distribution

The quality of synthesized RGO was evaluated using AFM and conductivity measurements. The height profile of RGO measured using atomic force microscopy (AFM) Fig (3.7a) shows the thickness of the RGO sheet to be 1.05 nm, revealing that the sheet has a single layer of RGO and is consistent with the previous literature reports. The conductivity for GO was found to be 0.04 S/m and the same for RGO was 934 S/m, which validates the claim regarding the quality of HRGO obtained using the aforementioned technique Fig (3.7b).

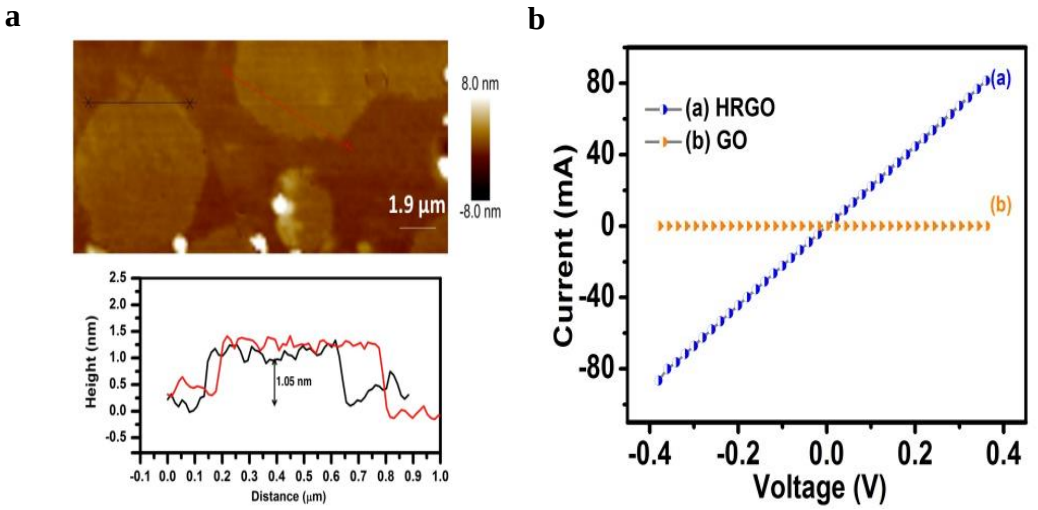

Fig 3.7: (a) AFM images showing height profile of HRGO (b) IV plots of (----) GO and (----) HRGO samples

X-ray photoelectron spectroscopy (XPS) analysis was carried out to provide direct evidence of reduction through the removal of oxygen functionality in graphene oxide. The C/O ratio of graphene oxide was calculated by taking the ratio of peak areas of C 1s to O 1s in XPS spectra Fig (3.8a) which increased from 2.5 to 11.3 after the reduction. The raw data of Carbon 1s XPS spectrum of graphene oxide was deconvoluted into four peaks which were assigned to four types of carbon (as shown in Fig (3.8b), with different chemical valences, including non-oxygenated ring carbon, C-C (284.8 eV), carbon in C–OH (286.5 eV), C-O-C (287.4 eV) and O-C=O (288.9 eV) respectively. After reduction, the decrease in the intensity of all C 1s peaks corresponding to the oxygenated carbon and the corresponding increase in the intensity of sp^2 carbon reconfirms the efficacy of this methodology in restoring the conjugated graphene network and removal of functional groups Fig (3.8c)

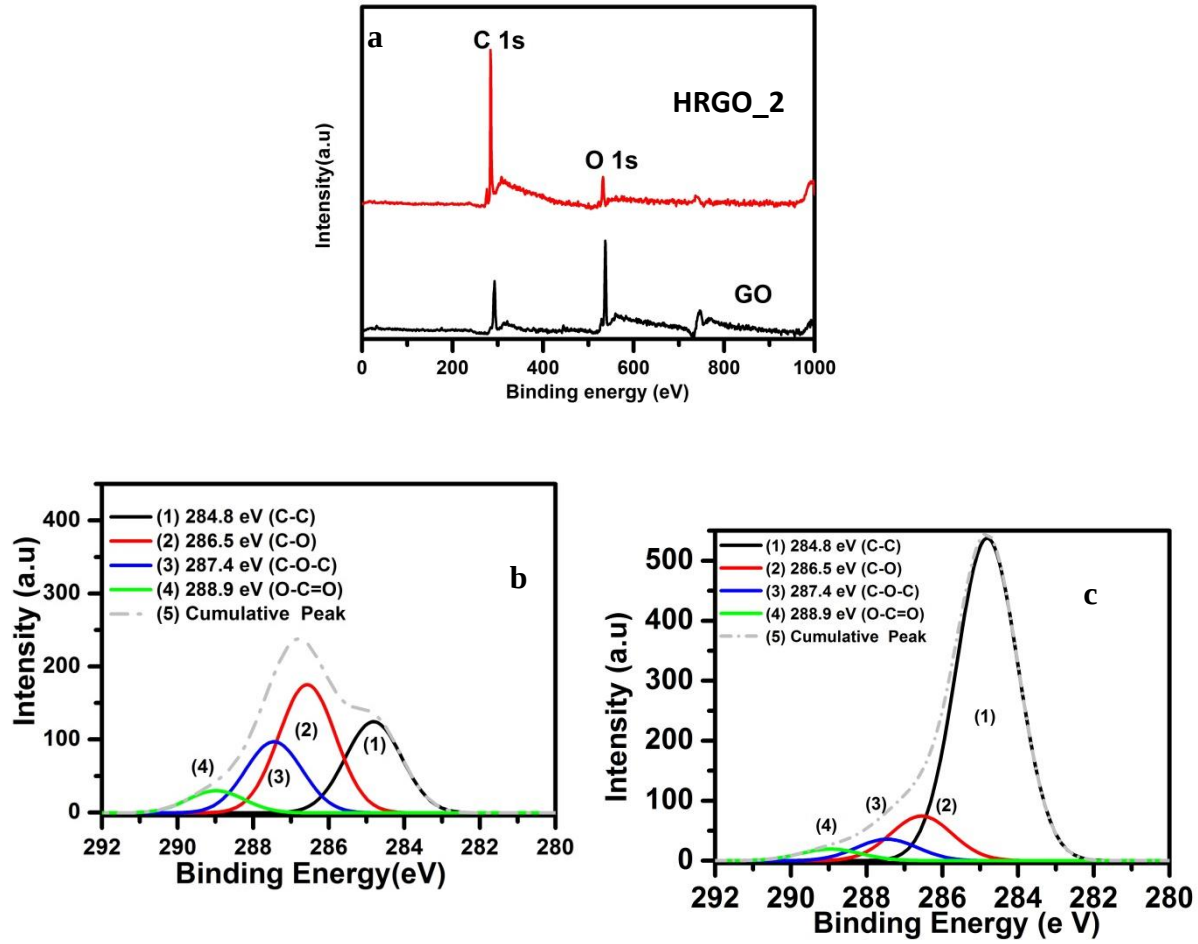

Fig 3.8: (a) Survey spectra of XPS of Graphene oxide and HRGO, Deconvulated XPS spectra of (b) Graphene Oxide (GO) (c) Hydrogen Reduced Graphene Oxide

The capacitive behavior of as-synthesized HRGO samples was evaluated using several electrochemical measurements. Cyclic voltammetry (CV) measurements were done in the potential window of 0−1 V, at various scan rates as shown in Fig (3.9a). Capacitive performance was indicated by an increase in current response with an increasing scan rate. The Galvanostatic charge−discharge (GCD) curve at various current densities is shown in Fig (3.9b). Charge−discharge curves are almost symmetrical, indicating the contribution of both double-layer capacitance and pseudocapacitance. At a current density of 0.5 A/g, HRGO showed a capacitance of 179 F/g. As the current density increases to 6 A/g, the HRGO retains only 48% of initial capacitance Fig (3.9b inset), which is due to the low penetration of ions in the inner pore induced by the fast potential changes [26]. In general, the capacitance is primarily proportional to the surface area of the electrode materials. Graphene has a very high electrical conductivity and an exceptionally large specific surface area (theoretical value, ~2650 m^2/g)

[27]. It was reported that such a high theoretical surface area can provide a gravimetric capacitance of a supercapacitor (SC) as high as 550 F/g [28]. Despite this promising interpretation, when prepared in the form of RGO using established solution processes (via Hummer's method), typical graphene SCs exhibit only 100 to 120 F/g in organic electrolytes [29] and around 135 F/g with aqueous electrolytes [30]. These smaller specific capacitances are attributed to irreversible restacking of the individual RGO sheets during the reduction and drying processes [31]. Graphene SCs are largely dependent on the detailed characteristics of graphene such as its functional groups, size, pore structure, and surface accessibility [32]. Lack of porosity in RGO makes substantial surfaces unavailable for charge storage.

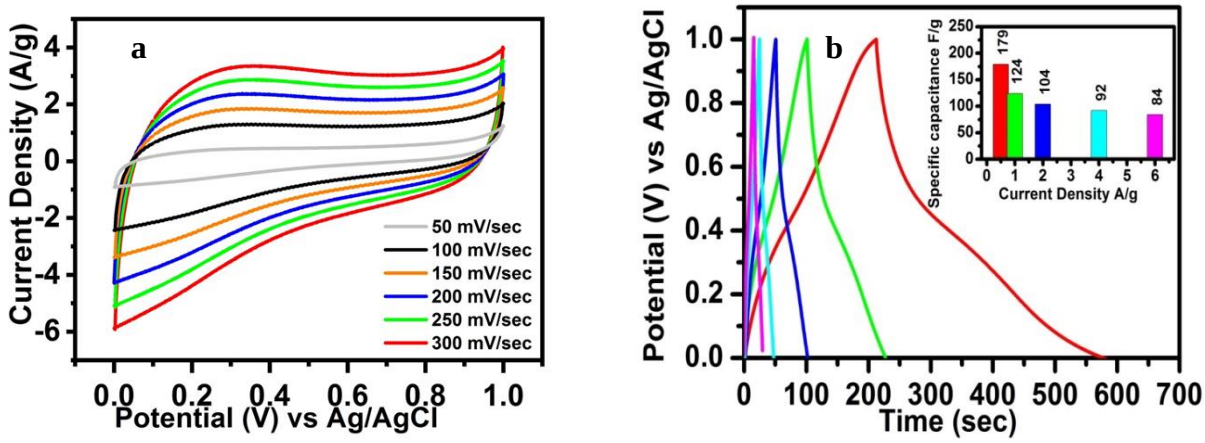

Fig 3.9:(a) CV curves at various scan rates (b) Galvanic charge-discharge curves at various charge densities with inset showing the variation of specific capacitance with current density 6 A/g

Nyquist plots at various amplitudes are shown in Fig (3.10a). The plot exhibited two distinct regions, that is, a semicircle in the high-frequency region and a slope line in the low-frequency region. Appropriate fitting of the obtained electrochemical impedance spectroscopy (EIS) spectra with the equivalent circuit diagram is shown in the inset, and the charge transfer resistance appears to be 7 Ω, which reveals the superior quality of HRGO. Furthermore, the cyclic rate performance of specific capacitance from charge−discharge measurements was evaluated. At a current density of 6 A/g, HRGO retained 93% of capacitance after 2000 cycles as shown in Fig (3.10b). The GCD curves are almost symmetrical in shape even after prolonged cycling as depicted in the inset Fig (3.10b)

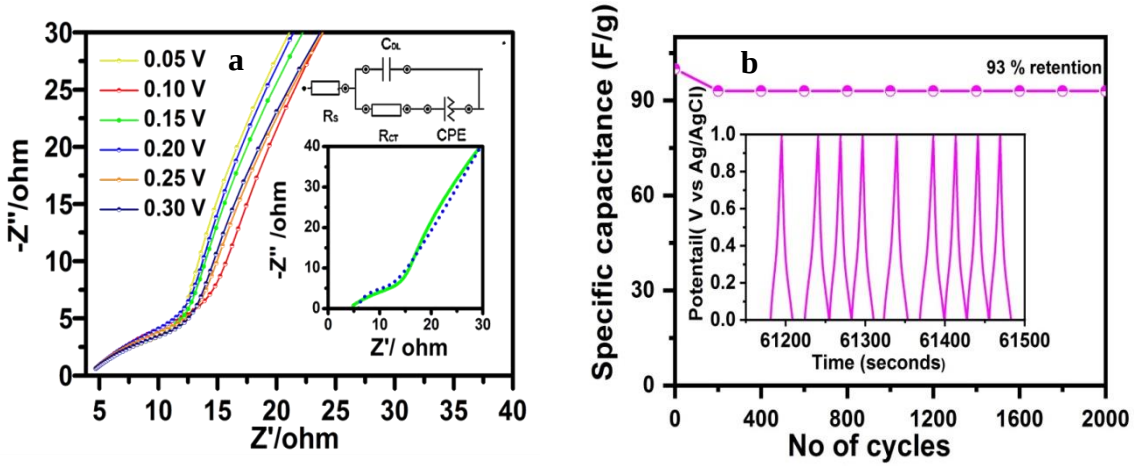

Fig 3.10 (a) Nyquist plots with inset showing high-frequency part and equivalent circuit diagram using for fitting EIS (b) Cyclic stability of HRGO at current density 6A/g with inset showing corresponding GCD for last 9 cycles of the stability plot.

3.4. Mechanistic studies

A two-way approach was attempted to understand and detect the reactive intermediate responsible for such GO to RGO reduction. The first approach involved the use of a probe substrate in the same reaction condition. The second approach was to monitor the reaction mixture during the progress of the reaction using a UV−visible spectrophotometer connected to the reactor.

In the first study, styrene oxide was used as the probe substrate in the same reaction condition to see the fate of the epoxide functionality that exists in the graphitic lattice of GO. Interestingly, peaks of all the products are visible in the spectra obtained from gas chromatography (GC) and GC−mass spectrometry Fig (3.11) with 81.9 % of conversion as shown below in table 3.1, and these are very much aligned with the products formed using traditional reducing agents reported in the previous literature [33] This evidence strongly supports the possibility of the formation of a transient reducing species responsible for such a reaction.

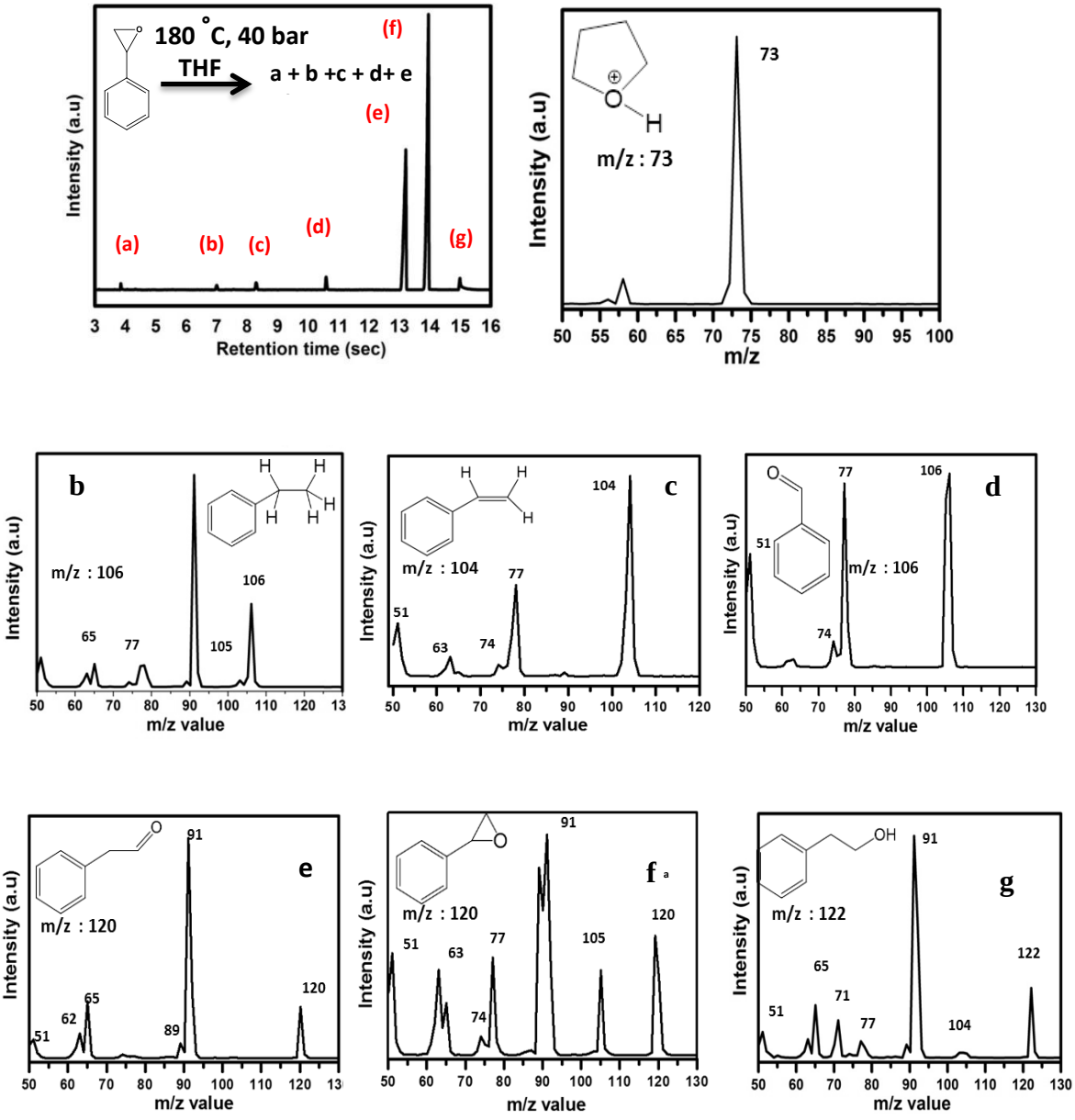

Fig 3.11: (a) GC spectra of styrene oxide after the reduction (b-g) Mass spectra of products obtained from the reaction of styrene oxide

3.4.1 Product profile

Total initial amount = 12.5 mM

Total unreacted amount = 0.23 mM

Actual amount of reactant = 12.5 mM-0.23 mM= 12.27 mM

Total amount product formed =10.05

% of conversion = 10.05/ 12.27= 81.9 %

Table 3.1: Product profile obtained after the reaction

Product	Peak area of product	Peak area of I.S	Rf value	Conc	Percentage of product formed
Ethyl benzene	**7978614**	**47444609**	**0.67**	**0.3 mM**	**6.8 %**
Styrene	**77808305**	**47444609**	**0.70**	**3 mM**	**30.54 %**
Benzaldehyde	**8747485**	**47444609**	**0.63**	**0.32 mM**	**3.25 %**
Phenyl acetaldehyde	**204637049**	**47444609**	**11.0**	**4. 4.7 mM**	**47.86 %**
Styrene oxide	**8414701**	**47444609**	**0.81**	**0.23 mM**	**Reactant**
Phenyl ethanol	**53733520**	**47444609**	**0.81**	**1.5 mM**	**15.2 %**

A possible mechanism Fig (3.12) for such reduction is shown below. Kindly note that the reactive intermediate proposed in the Reaction involving the probe substrate is purely based on the products obtained, and no claim has been made on the proof of the formation of the organic reactive intermediate.

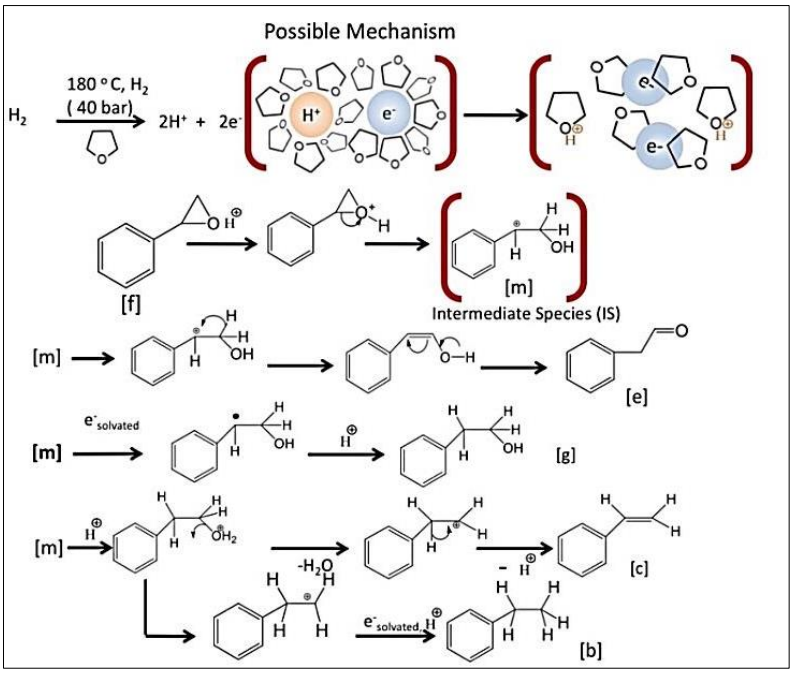

Fig 3.12 Schematic representation of the mechanism of the reaction.

The second approach is the In-situ monitoring of the reaction was done using a portable UV-Visible instrument from Ocean Optics, attached to the reactor through a connecting valve revealed the formation of a transient species generating peaks at 241 nm, 267 nm, 315 nm,

364 nm as shown in Fig (3.13). An aliquot of the reaction mixture was pumped out from the reactor through a 4 mm SS tube which directly connects the spectrometer cuvette. The time-dependent studies were carried out at room temperature (22°C) to see the decay of the species formed in the reaction.

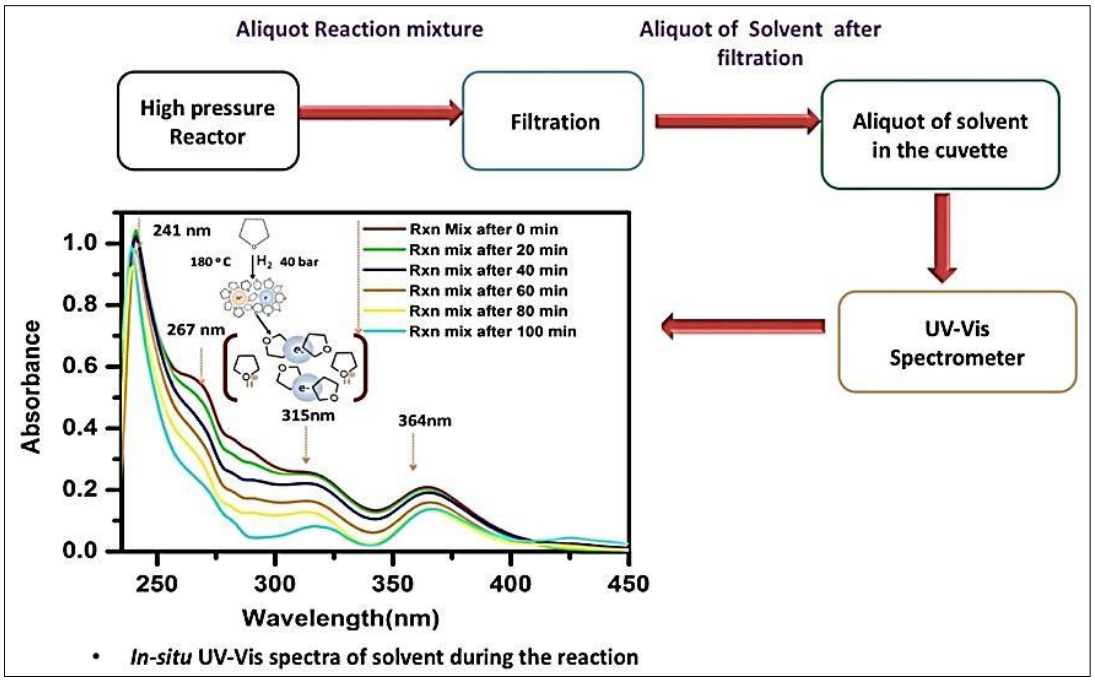

Fig 3.13: Showing UV-Visible spectra of the reaction mixture taken In-situ from the reactor. The sample was then monitored after a regular interval of time, which shows the decay of the shoulder peaks at 267 nm, 315 nm 364 nm.

Indeed, there was a detrimental change observed on the aforementioned peaks. This might be due to the decay of transient species generated during the reaction. In the UV-vis experiment, we observed a peak at 364 nm (Fig 3.13) that is nearly independent of time. From our absorption spectra calculations, we also noticed that there is no absorption peak beyond 250 nm for neutral THF. The UV-Vis spectra for THF in the controlled experiments also confirmed this observation, thus the peak at 364 nm cannot be originated from THF (solvent). To investigate this further, we computed the absorption spectra of anionic THF i.e. [THF]-, which clearly shows multiple peaks between 335 to 427 nm. Thus the peak at 364 nm could be attributed to the anionic species of THF [34]. Interestingly the peak at 267 diminishes in intensity within the time, which indicates the existence of a transient species in the reaction

mixture when observed in-situ. Further investigation of the anionic THF spectra was carried out but could not identify any absorption around 267 nm, except a very weak peak at 281 nm. We also could not identify the peak in the controlled experiments thus we are sure that this could not be only the anionic species, it has to be associated with a transient species. The reduction of THF-suspended GO at high (H_2) pressure indicates the formation of H+ + e− from H_2, which might lead to the formation of the solvated electron in THF. The role of THF in these reactions is extremely significant. An important structural aspect of THF is that it is a polar molecule which, we believe, may induce polarity in hydrogen molecules at that temperature and pressure. Apprehending the possibilities of the formation of such species, a DFT calculation directly correlating with the experimental results was performed to evaluate the electronic structure and properties of solvated electrons for anionic, solvated, and neutral forms of THF.

3.5 Computational study

3.5.1Genesis of the solvated electron

From the experimental results, we understood that reduction of GO takes place in THF in presence of "molecular hydrogen" only. Low hydrogen pressure reduces the extent of reduction. The role of THF in these reactions is extremely significant. An important structural aspect of THF is that it is a polar molecule which, we believe may induce polarity in hydrogen molecules at that temperature and pressure [35]. To further understand how it might happen, the density functional theory (DFT) based ab initio molecular dynamics simulations (AMID)simulations were performed at finite pressure and temperature (1 atm & 400 K) and 1 ps AIMD trajectory was generated. The initial analysis provides a very encouraging understanding that the molecular H2 dynamically interacts with the THF solvent at finite pressure and temperature. These THF (O)—H2 interactions might be the reason for knocking out an electron from the entire complex (THF—H2) and the latter eventually results in a very weekly bound electron in the system which we call here as 'solvated electron' Fig (3.14).

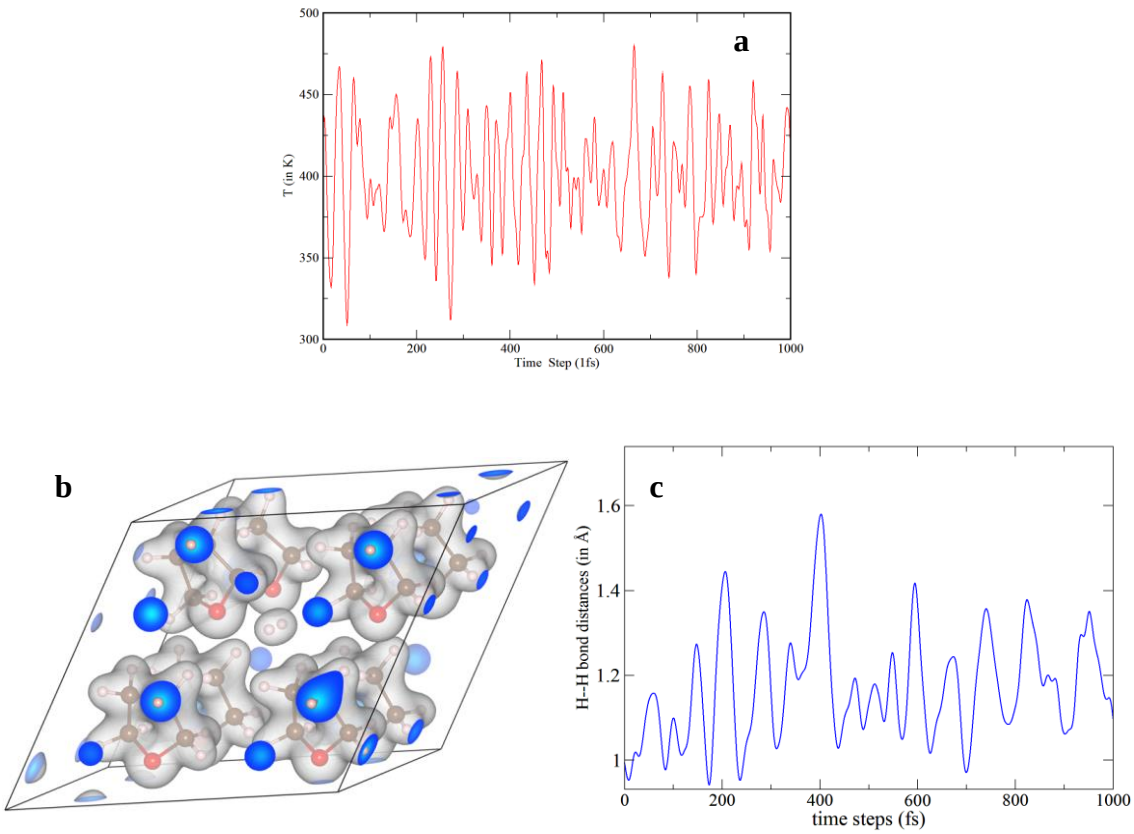

Figure 3.14: (a) The temperature fluctuations as obtained in the MD simulations, the average fluctuations at around 400 K indicate that the systems have reached the thermal equilibration state. (b) It depicts the fluctuations of H—H bonds at finite pressure and temperature. The large fluctuations indicate a high probability of temperature and pressure-assisted dissociation of the H—H bonds and generation of the solvated electrons. (c) Indicates the charge density distributions of the optimized structure at the gas phase when H2 is intercalated in the THF and does not interact with any of the THF.

3.5.2 Theoretical explanations of experimental results:

All the DFT calculations were performed employing Orca 4.0 quantum chemical code [35]. The molecular geometries were optimized using B3LYP functional and the electronic absorption spectra were computed adopting time-dependent density functional theory (TD-DFT). The long-range correction included hybrid exchange-correlation CAM-B3LYP along with the def2-TZVP basis sets that were used for the TD-DFT calculations [36]. The UV-Vis absorption spectra were calculated for the single-molecule in the gas phase and using the conductor-like polarizable continuum model (CPCM). The conductor-like polarizable continuum model (CPCM) was used with a dielectric constant value of 7.25 to address the solvent effect [37]. The

origin of all the individual peaks was analyzed by looking into the corresponding orbital transitions in the TD-DFT calculations [37]. The significant peaks observed in the experiment are at 364 and 267 nm that correspond to the transient species are lucidly explained from the TD-DFT calculations Fig (3.15).

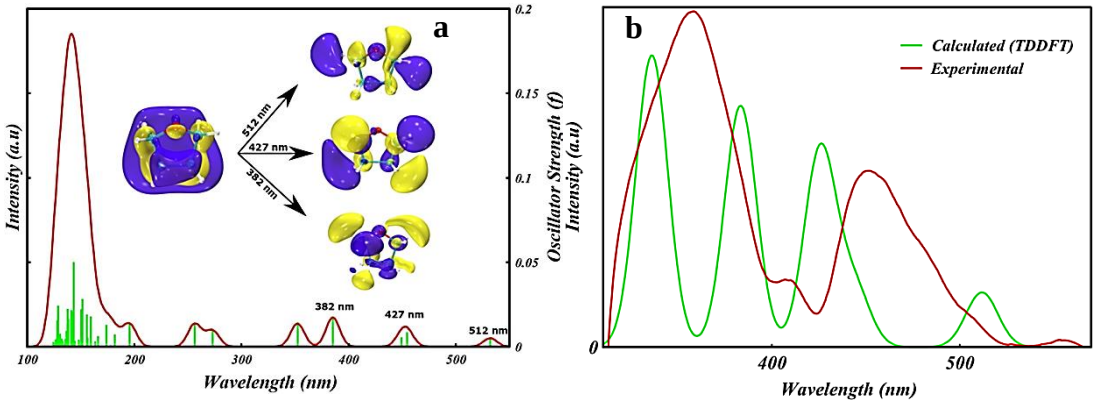

Figure 3.15**:** (a) UV-Vis absorption spectra for [e-.THF]. The orbital transitions that are responsible for the marked peaks at 382, 427, 512 nm. (b) The comparison of the UV-Vis spectra for $[THF]^-$ as obtained in experiments and also in TD-DFT calculations. The experimental absorption spectrum was obtained using 1mM of the $NaBH_4$ sol in the THF solvent, while the TDDFT spectrum was obtained using the CAM-B3LYP/def2-TZVP method.

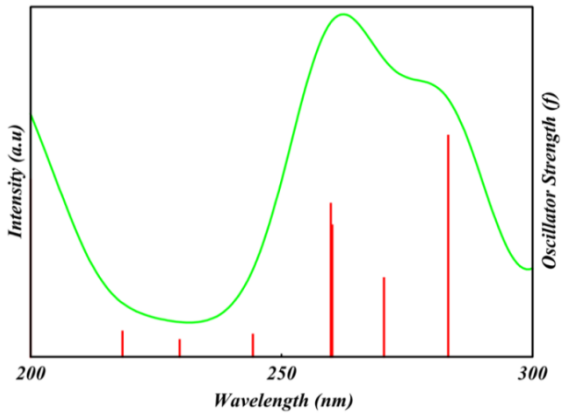

Fig 3.16**:** The computed UV-Vis spectra obtained from the TD-DFT calculations for the simplest model of the solvated electron with THF i.e. [e-].$[THF]_2$.

The transient species i.e. [e-]. $[THF]_2$, the simplest solvated electron model, was studied to find out the origin of the peak of the excitation observed at 264 nm in the experiment. The

absorption spectra observed between 200 to 300 nm are shown in Fig (3.16). While the molecular orbital contributions for the electronic excitation is tabulated in Table 3.2.

Table 3.2: The details of the orbital contributions for the important and selected electronic transitions for the anionic THF i.e. $[THF]^-$.

Absorption (nm)	Orbital Contributions in the electronic transitions	Oscillator Strength (*f*)
512 .00	**HOMO → LUMO+3 (94%)**	**0.002**
426.35	**HOMO → LUMO+5 (56%)**	**0.009**
	HOMO → LUMO+6 (42%)	
381.90	**HOMO → LUMO+6 (41%)**	**0.012**
	HOMO → LUMO+5 (56.9%)	
334.98	**HOMO → LUMO+7 (96%)**	**0.014**
273.25	**HOMO → LUMO+8 (96.2%)**	**0.007**
254.73	**HOMO → LUMO+9 (98.8%)**	**0.013**

The observed peaks at 315, 364, 412 nm in the UV-Vis experiment were concluded to be originated from the electronic transitions of THF anion. The molecular orbital contributions to each excitation are tabulated in Table 3.3. The major contributions for the aforementioned transitions arise from the HOMO→LUMO+7, HOMO→LUMO+5 and HOMO→LUMO+3 electronic transitions respectively. The observed experimental peak at 267 was correlated with peaks observed for the simplest solvated electron model of $[e^-].[THF]_2$.

Table 3.3: Molecular orbital contribution in the electronic transitions observed at 262 nm and 284 nm.

Absorption (nm)	Orbital Contributions in the electronic transitions	Oscillator Strength (*f*)
262	**HOMO →LUMO+15 (29%)**	**0.024**
	HOMO→LUMO+16 (52%)	
284	**HOMO→LUMO+13 (35%)**	**0.041**
	HOMO→LUMO+14 (49.6%)	

We hypothesized that the transient species is the *solvated electron* in THF. In presence of suspended GO in THF at high-pressure, H_2 generates H^+ and e^-. The generated e^- undergoes different non-equilibrium relaxation processes. It could reduce a neutral THF to $[THF]^-$. The other possibility is the generated electron could be solvated by the THF solvent molecules.

Here we would like to emphasize that the electron is a fundamental quantum particle and thus any classical picture of solvation (e.g. ions solvated in water) will certainly not hold. Rather, it's an additional electron that loosely bounds with multiple THF molecules and none of these solvent (THF) molecules that form the solvation shell can have exclusive access to that additional electron. Such special sharing of an electron between the THF molecules provides additional stability to be detected as the transient species. We speculate that over the time period such a solvation picture starts to diminish as one that THF molecules start to get the exclusive access of the electron and turns into $[THF]^-$ (anion) from the solvated electron $[e^-].[THF]_n$ picture. As a proof-of-concept, we have investigated the single anionic dimer i.e $[e^-].[THF]_2$ indicated that the additional electron gets trapped between the two [THF] species as the HOMO is localized in between spatial regions Fig (3.17). The TD-DFT spectra also confirm a prominent peak at 262 nm that is originated from HOMO to LUMO+16 (52%) electronic transition. This is commensurate with the transient peak observed in the experiments. We further observed that the neutral THF and anionic $[THF]^-$ have dipole moments opposite to each other (see Fig 17). Thus the solvent dynamics will play a crucial role in stabilizing the 'solvated electron', however, the detailed studies of dynamics are beyond the scope of the current work, they will be communicated elsewhere.

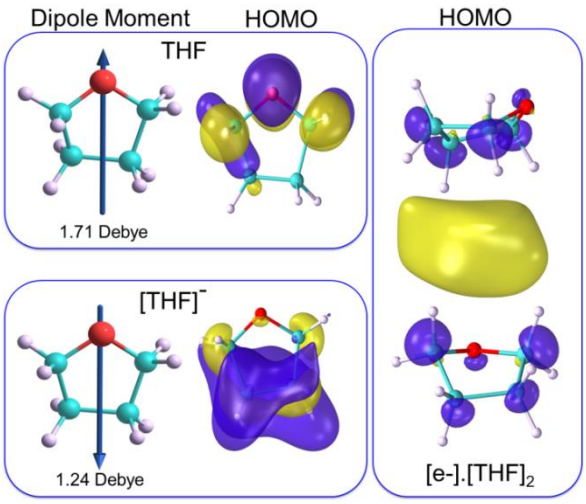

Fig 3.17: Calculated dipole moments for THF and [THF]- that orients opposite to each other are shown in the left panel along with the corresponding HOMOs. In the right panel the HOMO for [e-].[THF]2 indicates that the additional electrons do not reside within the molecules themselves. However, it localizes in a space enclosed by the two THF species. This entrapment of the electron in the space could be visualized as the solvation of the electron rather than the anionic form in cases of THF.

3.6 Conclusion

Herein, we have developed a new environment-friendly synthetic methodology to effectively reduce GO using molecular hydrogen at moderate pressure and temperature. Mechanistic studies with a two-way approach, along with theoretical analysis, reveal the possibility of the formation of a transient species, hypothesized as “solvated electron”. The RGO so formed has achieved a C/O atomic ratio greater than 11.3 and a bulk electrical conductivity of as high as 934 Sm−1. The combination of XPS and TGA analyses suggested that most of the labile oxygen functional groups were removed during hydrogen reduction. Compared to other methods using reducing agents, such as hydrazine, NaBH4, HI, and so forth, this process is less time-consuming and hassle-free as post purification of the product is not required. There is a huge possibility to explore and optimize the procedure for industrial applications.

References

1 Y. Zhu, S. Murali, W. Cai, X. Li, J. W. Suk, J. R. Potts, and R. S. Ruoff, *Adv. Mater.*, 2010, **22**, 3906–3924.

2 K. S. Novoselov, V. I. Fal, L. Colombo, P. R. Gellert, M. G. Schwab and K. Kim, *Nature*, 2012, **490**, 192–200.

3 Q. He, S. Wu, S. Gao, X. Cao, Z. Yin, H. Li, P. Chen and H. Zhang, *ACS Nano*, 2011, **5**, 5038–5044.

4 M. J. Allen, V. C. Tung and R. B. Kaner, *Chem. Rev.*, 2010, **110**, 132–145.

5 X. Huang, Z. Yin, S. Wu, X. Qi, Q. He, Q. Zhang, Q. Yan, F. Boey and H. Zhang, *small*, 2011, **7**, 1876–1902.

6 S. Park and R. S. Ruoff, *Nat. Nanotechnol.*, 2009, **4**, 217–224.

7 H. Bai, C. Li, and G. Shi, *Adv. Mater.*, 2011, **23**, 1089–1115.

8 Y. Si and E. T. Samulski, *Nano Lett.*, 2008, **8**, 1679–1682.

9 V. C. Tung, M. J. Allen, Y. Yang and R. B. Kaner, *Nat. Nanotechnol.*, 2009, **4**, 25–29.

10 D. Li, M. B. Müller, S. Gilje, R. B. Kaner and G. G. Wallace, *Nat. Nanotechnol.*, 2008, **3**, 101–105.

11 D. Van Thanh, N. Van Thien, B. H. Thang, N. Van Chuc, N. M. Hong, B. T. Trang, T. Dai Lam, D. T. T. Huyen, P. N. Hong and P. N. Minh, *J. Electron. Mater.*, 2016, **45**, 2522–2528.

12 I. K. Moon, J. Lee, R. S. Ruoff, and H. Lee, *Nat. Commun.*, 2010, **1**, 1–6.

13 H. D. Pham, V. H. Pham, T. V. Cuong, T.-D. Nguyen-Phan, J. S. Chung, E. W. Shin, and S. Kim, *Chem. Commun.*, 2011, **47**, 9672–9674.

14 C. Zhang, W. Lv, W. Zhang, X. Zheng, M. Wu, W. Wei, Y. Tao, Z. Li, and Q. Yang, *Adv. Energy Mater.*, 2014, **4**, 1301565.

15 Y. Liu, Y. Li, M. Zhong, Y. Yang, Y. Wen and M. Wang, *J. Mater. Chem.*, 2011, **21**, 15449–15455.

16 V. H. Pham, H. D. Pham, T. T. Dang, S. H. Hur, E. J. Kim, B. S. Kong, S. Kim and J. S. Chung, *J. Mater. Chem.*, 2012, **22**, 10530–10536.

17 Z.-J. Fan, W. Kai, J. Yan, T. Wei, L.-J. Zhi, J. Feng, Y. Ren, L.-P. Song and F. Wei, *ACS Nano*, 2011, **5**, 191–198.

18 R. Krishna, E. Titus, L. C. Costa, J. C. Menezes, M. R. P. Correia, S. Pinto, J. Ventura, J. P. Araújo, J. A. S. Cavaleiro and J. J. A. Gracio, *J. Mater. Chem.*, 2012, **22**, 10457–10459.

19 H. Feng, R. Cheng, X. Zhao, X. Duan and J. Li, *Nat. Commun.*, 2013, **4**, 1–8.

20 O. C. Compton, B. Jain, D. A. Dikin, A. Abouimrane, K. Amine, and S. T. Nguyen, *ACS Nano*, 2011, **5**, 4380–4391.

21 D. C. Marcano, D. V Kosynkin, J. M. Berlin, A. Sinitskii, Z. Sun, A. Slesarev, L. B. Alemany, W. Lu, and J. M. Tour, *ACS Nano*, 2010, **4**, 4806–4814.

22 T. Yanai, D. P. Tew, and N. C. Handy, *Chem. Phys. Lett.*, 2004, **393**, 51–57.

23 F. Neese, *Wiley Interdiscip. Rev. Comput. Mol. Sci.*, 2012, **2**, 73–78.

24 S. Thakur and N. Karak, *Carbon N. Y.*, 2012, **50**, 5331–5339.

25 A. C. Ferrari and J. Robertson, *Phys. Rev. B*, 2000, **61**, 14095.

26 S. Kannappan, K. Kaliyappan, R. K. Manian, A. S. Pandian, H. Yang, Y. S. Lee, J.-H. Jang and W. Lu, *arXiv Prepr. arXiv1311.1548*.

27 Y. Zhu, S. Murali, M. D. Stoller, K. J. Ganesh, W. Cai, P. J. Ferreira, A. Pirkle, R. M. Wallace, K. A. Cychosz, and M. Thommes, *Science (80-.).*, 2011, **332**, 1537–1541.

28 J. Xia, F. Chen, J. Li and N. Tao, *Nat. Nanotechnol.*, 2009, **4**, 505–509.

29 C. Liu, Z. Yu, D. Neff, A. Zhamu and B. Z. Jang, *Nano Lett.*, 2010, **10**, 4863–4868.

30 M. Jana, S. Saha, P. Khanra, P. Samanta, H. Koo, N. C. Murmu and T. Kuila, *J. Mater. Chem. A*, 2015, **3**, 7323–7331.

31 J. H. Lee, N. Park, B. G. Kim, D. S. Jung, K. I'm, J. Hur and J. W. Choi, *ACS Nano*, 2013, **7**, 9366–9374.

32 B. G. Choi, M. Yang, W. H. Hong, J. W. Choi and Y. S. Huh, *ACS Nano*, 2012, **6**, 4020–4028.

33 A. A. Dabbawala, N. Sudheesh and H. C. Bajaj, *Dalt. Trans.*, 2012, **41**, 2910–2917.

34 R. M. Young, M. A. Yandell, M. Niemeyer and D. M. Neumark, *J. Chem. Phys.*, 2010, **133**, 154312.

35 H. G. Holland and R. J. W. Le Fevre, *J. Chem. Soc.*, 1950, 2166–2169.

36 M. Cossi, N. Rega, G. Scalmani and V. Barone, *J. Comput. Chem.*, 2003, **24**, 669–681.

37 D. Jacquemin, V. Wathelet, E. A. Perpete and C. Adamo, *J. Chem. Theory Comput.*, 2009, **5**, 2420–2435.

Chapter 4

Ultrathin Co_3O_4 Nanosheets wrapped Mesoporous TiO_2 for Oxygen Evolution Reaction

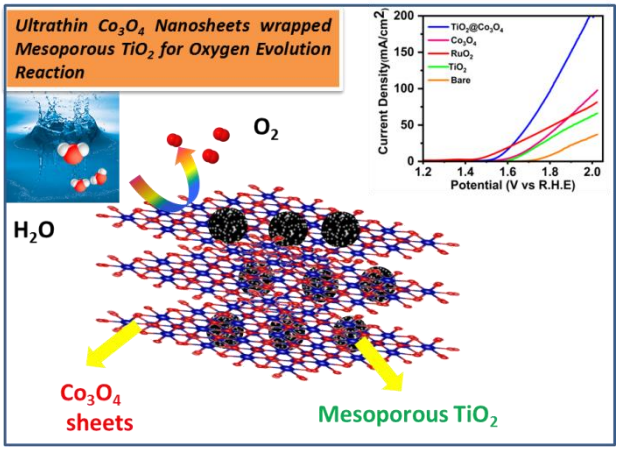

Abstract: *If carbon emissions continue at this rate in the foreseeable future, human life may be jeopardised. To address the dual problems of CO_2 emissions and fossil fuel exhaustion, a clean energy alternative is required. In this sense, hydrogen may be a viable carbon-neutral alternative for alleviating global energy issues and paving the way for a long-term solution. Large-scale hydrogen generation via electrochemical water splitting, on the other hand, remains a problem, since it requires a complex four-electron transfer mechanism of the oxygen evolution process (OER) at the anode. The synthesis of efficient, long-lasting, earth-abundant, and inexpensive electrocatalyst for the oxygen evolution reaction is a contentious topic of research. Herein the Co_3O_4 Nanosheets entrapping the Mesoporous TiO_2 particles deliver a noticeable performance for OER in an alkaline medium. The catalyst is synthesized using a simple, cost-effective approach, and the obtained catalyst showcases an overpotential of 340 mV at a current density of 20 mA/cm^2 with the good long-term durability of 20 hr. The catalyst also shows a lower value Tafel slope of 70 mV/dec with turn over frequency of 0.025sec -1 at an overpotential of 400 mV. The superior activity of the heterostructure can be witnessed due to the cooperative interaction between the two at the interface*

4.1. Introduction

An enormous chunk of iceberg, which is roughly 105 miles long and 15 miles wide, larger than Rhode Island, recently broke off from the western side of Antarctica's Ronne Ice Shelf, according to the European Space Agency. The "Doomsday Glacier," was noticed to be melting much faster than expected as reported by Live Science. The warm-water current from the east cut away at the vital "pinning points" that hold the shelf to the land. The collapse of this glacier could potentially take the rest of the West Antarctic Ice-Shelf with it, causing a rise of 10-feet in the global sea levels. The increased heat stress on the earth's surface as a consequence of the exponential increase in CO_2 emission is one of the major reasons for such environmental deterioration. Therefore, a sustainable solution to resolve these problems is highly desirable in the present time.[1, 2] The renewable energy sources namely solar, wind, tidal, etc., can be coupled with electrochemical technologies for energy conversion and storage applications.[3-6] The oxygen evolution reaction (OER), is the anodic reaction of water electrolyzers, which has an enormous potential towards air-battery/fuel cell applications (Scheme 1).[7, 8] However, the development of a highly active, stable, inexpensive OER catalyst is still a challenge in the pathway of these techniques.[8, 9] In general, OER is a four-electron transfer process in which high overpotential is required to achieve a desired current density.[10, 11] Precious metals such as Ir, Ru, and their oxides carry the tag of most efficient electrocatalyst for OER by offering a low overpotential yet their applicability on commercial platforms is restricted due to their higher cost and poor stability.[12-15] Therefore, constant efforts have been devoted to the development of new, low cost and efficient electrocatalysts based on non-noble earth-abundant metals for OER. The transition metal-based materials for instance oxides,[16-18] hydroxides,[19-21] phosphides,[22-24] nitrides,[25-27], and sulphides[28-30] have marked their presence in the race of Electrocatalytic activities efficient towards OER. However, out of these transition metal-based catalysts, oxides have shown superior stability under the OER conditions, highlighting their prominent behaviour. Although the transition metal oxides have shown significant potential towards OER application, there are several aspects associated with the stability and activity, where improvements are required to make them suitable for commercial applications. Mostly Oxides and hydroxides of Ni, Co, and Fe have appeared as a favourable class of catalysts.[31] Out of the extensive range of transition

metal oxides, cobalt oxide spinel has acquired firm attention because of the possession of d-band electrons similar to noble metals as well as the occurrence of mixed-valence states.[32-34] In recent literature reports, Co_3O_4 has been clubbed with other transition metal oxides[35] doped with electron donors or supported on carbon or heteroatom doped high surface area and conductive carbon substrates to refine and further enhance the catalytic activity.[36] On the other hand, TiO_2 has never been highlighted for oxygen evolution catalysis though it is a highly robust and efficient photocatalyst for water splitting. Having advantages of large surface areas, and wide range of pore size distributions recently Mesoporous TiO_2 catalysts have shown an extensive range of applications in the electro catalysis and other energy storage applications [37, 38] . Several improvisations have been reported to enhance the activity of this candidate that mainly includes the doping with other transition metals cations.[39, 40] Nevertheless, these hybrid combinations still fail to deliver low over potentials as compared to benchmark catalysts.[9] Combinations of TiO_2 with other transition metal oxides is a new a method where the interface between the two phases play a vital role in accelerating the OER activity without involving conductive carbon substrates as an integral support system. Herein, we have fabricated a hybrid nanostructure with Mesoporous TiO_2 embedded on Co_3O_4 Nanosheets. The amalgamation of Mesoporous TiO_2 with Co_3O_4 interfaces indeed accelerates OER activity even in absence of any carbonaceous components. The hetrostructure shows a OER activity with an overpotential of 340 mV at 10 mA/cm^2 with a long-term stability of 20 hours at current density 20 mA/cm^2. The electrochemical active surface area (ECSA) also indicates a higher activity for TiO_2@Co_3O_4.

4.2. Experimental Section

4.2.1. Materials

The chemicals used in this work were used without further purification. Cobalt nitrate hexahydrate Co $(NO_3)_2.6H_2O$ with 99% purity and $NaBH_4$purchsed from CDH, Urea (CH_4N_2O, 99%) from SRL chemicals, Ammonia from Merck, Tetrabutyl isoporopoxide TTIP and Nafion per fluorinated resin solution (manufactured by: Sigma Aldrich). In all synthesis procedures, deionized water was used.

4.2.2. Synthetic Procedures

4.2.2.1. Synthesis of Mesoporous TiO_2

The Mesoporous TiO_2 was synthesized using the reported procedure with minor modification. In brief 0.5 g of octadecylamine, 1 ml of ammonia solution, 1.0 ml of TTIP were dissolved in 25 ml of ethyl alcohol and stirred for 30 mins followed by the addition of 30 ml of distilled water. The above solution was transferred into a 100 ml Teflon vessel and heated at 200°C for 6 h. The obtained precipitates were dried at 50°C in a vacuum oven after washing several times with water for further use. In the end, the white precipitates were calcined at 550°C for 4 hours in the air to obtain the Mesoporous TiO_2.

4.2.2.2. Synthesis of Catalyst

For the synthesis of catalyst firstly 20 mg of Mesoporous TiO_2 was dispersed in 10 ml of distilled water. After this 0.3 mole of Co $(NO)_3.6H_2O$ was added to the above dispersion and stirred overnight. To this 1 M solution of $NaBH_4$ was added which results in the formation of black precipitates. The above precipitates were washed with distilled water and further dried at 50°C in a vacuum oven. The resulting precipitates were calcined at 600°C for 2hrs in the air to obtain Mesoporous TiO_2 spheres wrapped in Co_3O_4 sheets. As a supporting catalyst pure Co_3O_4 was also synthesized using the above protocol excluding the addition of Mesoporous TiO_2.

4.3 Characterization

4.3.1. Physical Characterization:

PXRD spectra of the TiO_2 @ Co_3O_4 catalyst, TiO_2 and $Co_3O_4$was recorded on Bruker Eco D8 advance with Cu Kα radiation (λ = 1.54056 Å), from 2θ 10^o to 80^o and step size of 0.019^o. Scanning electron microscopy was done using JSM 7610 FPlus JEM -2100. TEM operated at 200 kV was used to capture the TEM images. BET analysis was done using Autosorb IQ Qunatchrome Instrument. XPS studies were done using ESCA Lab: 220-IXL equipped with Mg Kα nonmonochromated X-ray beam having photon energy 1253.6 eV.

4.3.2. Electrochemical Measurements:

OER catalytic properties of the TiO_2 @ Co_3O_4 catalyst along with Mesoporous TiO_2, Co_3O_4, and the commercial RuO_2 catalyst were also examined on electrochemical workstation CHI660E using graphite electrode and the standard Ag/AgCl electrode as counter and reference electrodes. The catalyst ink was prepared by dispersing 5 mg of TiO_2 @ Co_3O_4 catalyst in 490 ul of 1:1 water-ethanol solution and 10 ul of Nafion using Labsonic LBS2-10 BATH Sonicator for 60 min. Graphite strip serves the purpose of working electrode here. 40 ul of ink was drop cast on a 0.25 cm^2 area of 1x1 graphite strip whereas the remaining area was used for making the contact. Polarization curves were collected at a low scan rate of 2 mV/s in 1M KOH and the overpotential were reported w.r.t to R.H.E and also iR corrected. Tafel plot is obtained by plotting overpotential against logarithmic current density. The linear section of the Tafel plot was fitted to the Tafel equation ($\eta = b \log (j) + a$) to obtain the Tafel slope. The impedance spectra were obtained at different overpotentials, that is, 100, 150, and 200 mV, and a frequency range of 100000-0.1 Hz. At an applied potential of 340 mV chronoamperometry measurement of the TiO_2 @ Co_3O_4 catalyst was done to evaluate the stability under the prolonged duration. For the estimation of ESCA cyclic voltammetry was done at different scan rates i.e. (20mV/s to 120mV/s) in the potential window of 1.02 V to 1.11 V. The values of TOF for OER was calculated using the given formula

TOF = $j * A4 * F * n$

Where j denotes the current density (mA /cm2), F is Faraday's constant (96485.3 C mol^{-1}), A is the geometric surface area of the electrode and n is the moles of the catalyst.

4.4. Results and Discussion:

The catalyst was synthesized using a simple and cost-effective approach as shown in scheme 1. The reduction route using $NaBH_4$ results in the formation of Co_3O_4 Nanosheets around Mesoporous TiO_2. The structural analysis of the TiO_2 @ Co_3O_4 catalyst along with Co_3O_4 and TiO_2 was carried out firstly with the help of PXRD as presented in Fig (4.1a) where all the peaks at 2θ values 25°, 37.7°, 48°, 53.9°, 55.1°, 62.7°, 68.5°, 70.3°, 75.09° can be marked to Anatase phase of TiO_2 whereas the peaks at 2θ 31.2°, 36.8°, 38.5°, 44.8°, 55.6°, 59.3 °,

65.2 ° can be indexed to the cubic phase of Co_3O_4. The peaks obtained in the case of Co_3O_4 and TiO_2 spectra can be indexed to the cubic phase of Co_3O_4 and Anatase phase of TiO_2 respectively Fig (4.1b) & (4.2).

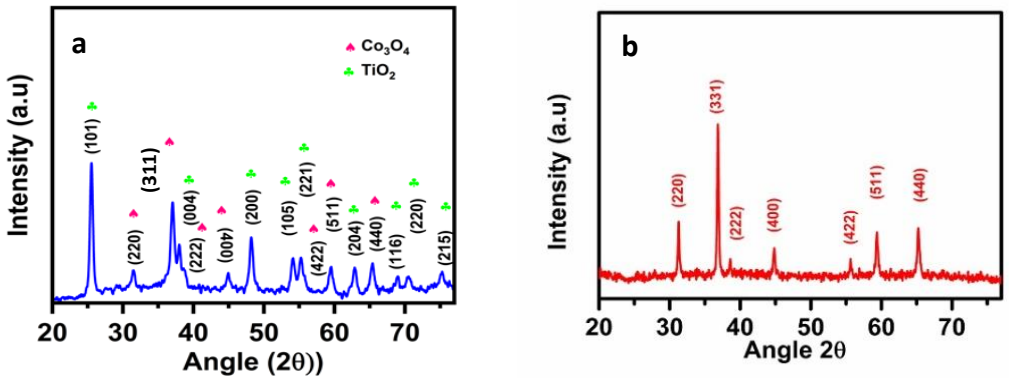

Fig 4.1: PXRD spectra of (a) TiO_2 @ Co_3O_4 (b) Co_3O_4

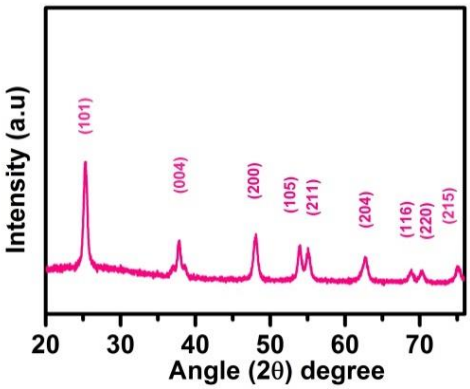

Fig 4.2: PXRD spectra of TiO_2

After PXRD chemical state of the catalyst was analysed using XPS. The survey scan spectra were shown in (Fig 4.3a) where the appearance of characteristic peaks of Co 2p, O 1s, and the 2p confirms the presence of Co, Ti, and O in the catalyst. The high-resolution spectra of Co 2p confirm the presence of two key peaks at 781.1 eV (Co 2p ½) and 797 eV (Co 2p 3/2) separated by an energy difference of˜ 15 eV along with a satellite peak at higher binding energy which approves the existence of two valence state (Co^{+2} and Co^{+3}) of Co_3O_4 in the catalyst Fig (4.3b). After deconvolution, the peak at 781.1 eV and 796.7 eV correspond to Co^{+3} whereas peaks at 782.7 eV and 799.6 eV correspond to Co^{+2} [41]. On the quantification of peak area, the ratio of Co^{+3} /Co^{+2} comes out to be 1.9. The higher percentage of Co^{+3} in the catalyst facilitates the adsorption of OH^- ions which in turn enhances the OER activity. The O

1s spectra can be Deconvulated into peaks at 529 eV, 530.4 eV, 531.5 eV, and 532.4 eV. The first two peaks correspond to lattice oxygen i.e. Co-O bond and Ti-O bond respectively Fig (4.3c). Further, the peak at 531.5 eV and a weak shoulder at 532.4 eV correspond to surface adsorbed oxygen. As shown in Fig (4.3d) in Ti 2p spectra two peaks at 459 eV and 465.28 appeared which can be nominated to Ti 2p $_{1/2}$ and Ti 2p $_{3/2}$ spin states of Ti 2p in the catalyst [42].

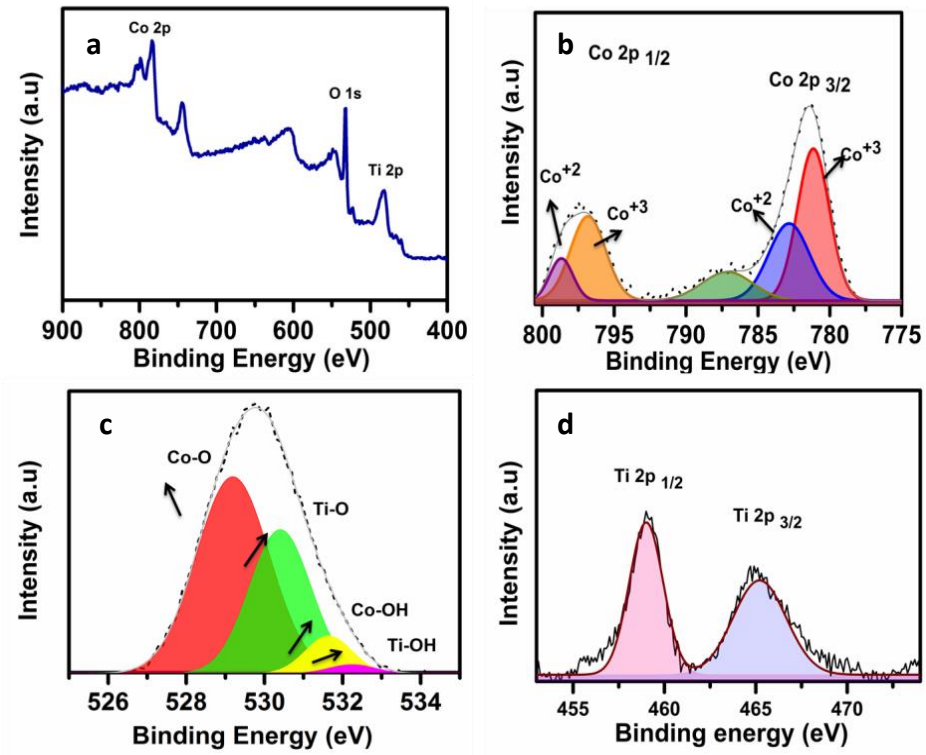

Fig 4.3: (a) Wide scan spectra of TiO_2 @ Co_3O_4 catalyst (b) High resolution spectra of Co 2p (c) O 1s and (d) Ti 2p

The morphology and detailed structural analysis of the catalyst was done using FESEM, TEM, and HRTEM. Fig (4.5a) displays the FESEM image of the Mesoporous titanium dioxide particles. The FESEM image shows the porous nature of titanium oxide particles with a surface area of 67.04 m^2/g and pore size 6.2 nm as analysed from BET isotherm Fig (4.4a). Benifited from this the catalyst also posses high surface area of 77.03 m2/g and pore size of nm Fig (4.4b). From the TEM image as shown in Fig (4.5b) it can be observed that Mesoporous TiO_2 was wrapped in Co_3O_4sheets. The HRTEM images shown in Fig (4.5c) reveal the presence of lattice fringes with a d spacing of 0.24 nm and 0.35 nm which can be endorsed to the (311) plane of $Co_3O_4$and (101) plane of TiO_2 respectively. Furthermore, from elemental mapping Fig (4.5(a-d)) and EDX spectra Fig (4.5e) the presence of both TiO_2 and Co_3O_4 is confirmed which is in line with the aforesaid TEM and HR-TEM results.

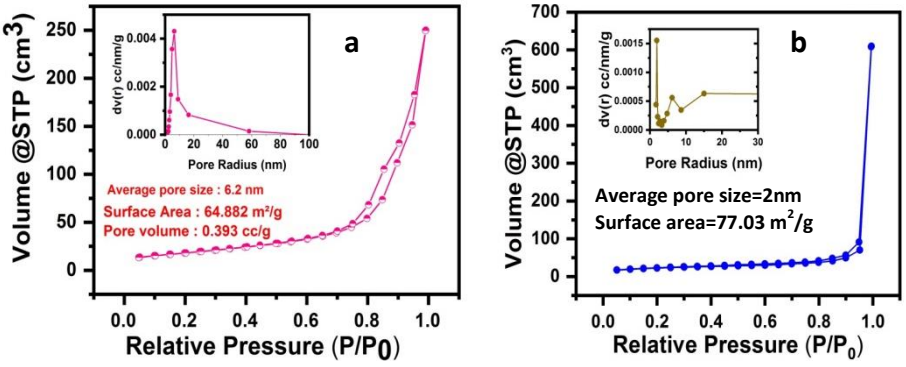

Fig 4.4: (a) BET isotherm of TiO_2 (b) BET isotherm of TiO_2 @ Co_3O_4 catalyst along with pore size distribution shown in the inset for both.

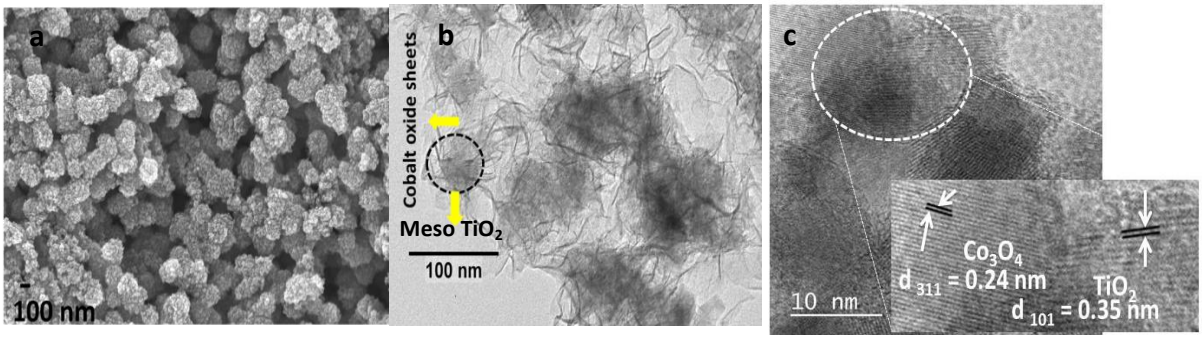

Fig 4.5(a) FESEM image of (b) TEM image of the catalyst (c) HRTEM image of the catalyst

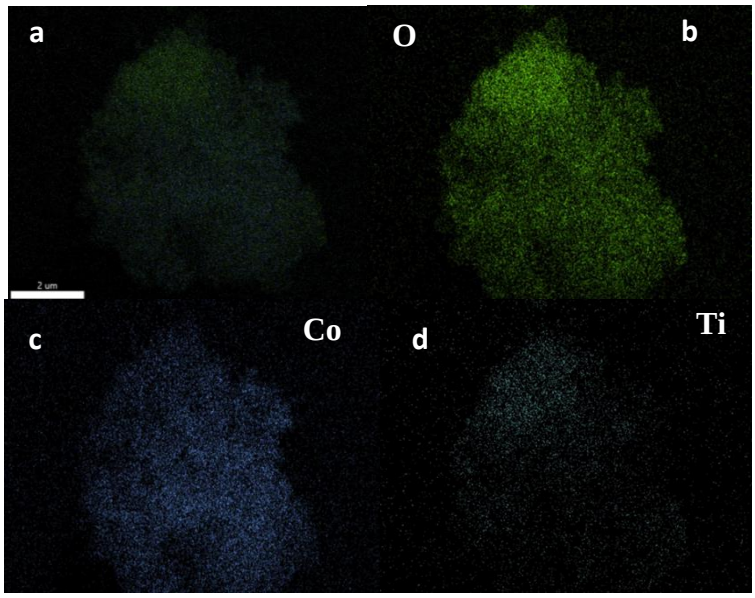

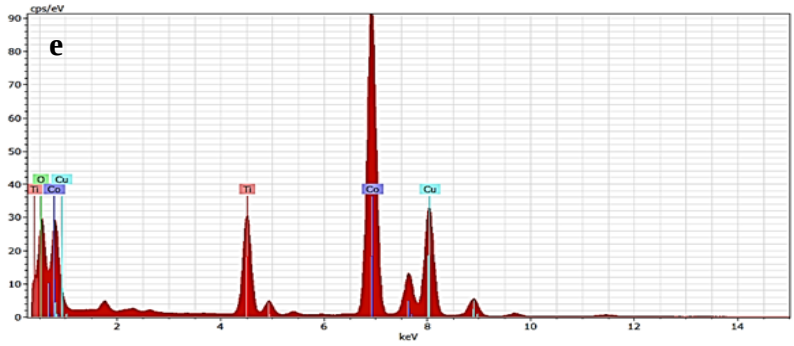

Fig 4.6: (a-d) SEM images corresponding to the elemental mapping of the catalyst (e) EDX spectra of catalyst

After the structural as well as morphological characterization The OER activity of TiO_2 the $TiO_2@Co_3O_4$ catalyst was examined in O_2 saturated 1 M KOH at room temperature. The catalytic activity of TiO_2, Co_3O_4, and commercially available RuO_2 was also studied under similar conditions. From the polarization curves as presented in Fig (4.6a), it can be perceived that the performance of the catalyst is more superior as compared to TiO_2, Co_3O_4, and commercially available RuO_2. With an onset potential of 250 mV, the catalyst $TiO_2@Co_3O_4$ shows overpotential of 340 mV at current density 10 mA/cm^2 whereas for TiO_2 and CO_3O_4 the minimum overpotential at current density 10 mA/cm^2 is 440 mV and 420 mV respectively as shown in Fig (4.6b).

To get a clear vision of OER kinetics and mechanistic parameters the Tafel slopes were obtained using LSV curves. OER reaction in the alkaline medium typically follows a multi-step reaction pathway which is defined as follows: The values of Tafel slope can provide perceptive information about the rate-determining step of the OER process.

$M + OH^- \rightarrow M{-}OH + e^-$ (1)

$2MOH \rightarrow MO + H_2O$ (2)

$MO + OH \rightarrow M{-}OOH$ (3)

$2M{-}OOH \rightarrow MO + M + HO + O_2$ (4)

It is believed that if the first step of the OER which involves the transfer of electron is rate-determining then the appropriate value of Tafel slope is 120 mV/Dec on the other hand if the value is around 60 mV/Dec then the rate of reaction is governed by the complex second step rather than the first step which involves electron transfer. From Fig (4.7a) it can be observed

that the value of Tafel slope in case of catalyst is 70 mV/Dec which is even lower than the value for RuO_2 110mV/dec indicating that in this case, the electron transfer step is no longer a rate-determining step emphasizing the massive availability of electrons on the catalyst surface. On contrary, the values of the Tafel slope for TiO_2 and Co_3O_4 are 110 mV/dec and 120 mV /dec inferring that the rate of reaction is controlled by the first step in both the cases. To get the insight of charge transfer at the interface EIS technique was performed and impedance spectra at applied potentials 100 mV and 150 mV were acquired for the catalyst as well as supporting catalysts. The simulated version of a plot measured at 150 mV and the circuit used for simulation is shown in the inset. From the fitting data as shown in Fig (4.7b), it can be noticed that the catalyst bears very low charge transfer resistance (7 ohms at 150 mV) as compared to the supporting catalysts highlighting the faster electron migration at the interface.

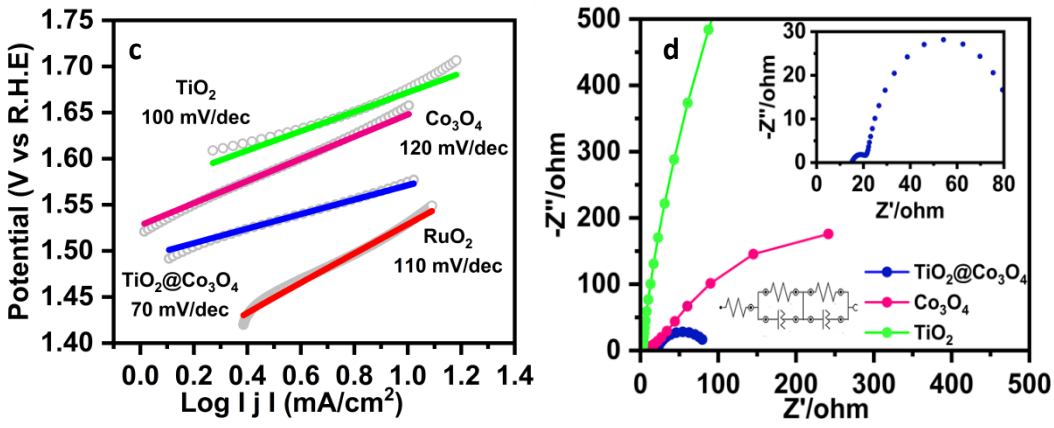

Fig 4.7 (a) Linear sweep voltammetry curves of TiO_2@ Co_3O_4 catalyst along withMesoporous TiO_2, Co_3O_4 and the commercial RuO2 catalyst (b) Comparison of overpotential of TiO_2@ Co_3O_4 catalyst, Co_3O_4 and TiO_2 at 10 mA/cm^2 (c) Tafel slopes obtained from LSV curves of all aforementioned catalyst (d) Nyquist plot of TiO_2@ Co_3O_4 catalyst, Co_3O_4 and TiO_2 at 150 mV with equivalent circuit shown in inset.

Another important landmark that the catalyst has to achieve is long-term durability which was checked by the chronoamperometry technique Fig (4.8a). The experiment was performed at a current density of 20 mA/cm2 for over 20 hrs, where it can be inferred that there is no significant change in the current density even after such a long duration with catalyst retaining 85 % of the initial current density. By doing the HRTEM and after stability studies,

the original crystal structure and morphology were obtained, which unfolds its integrity after the catalyst shown in Fig (4.8b).

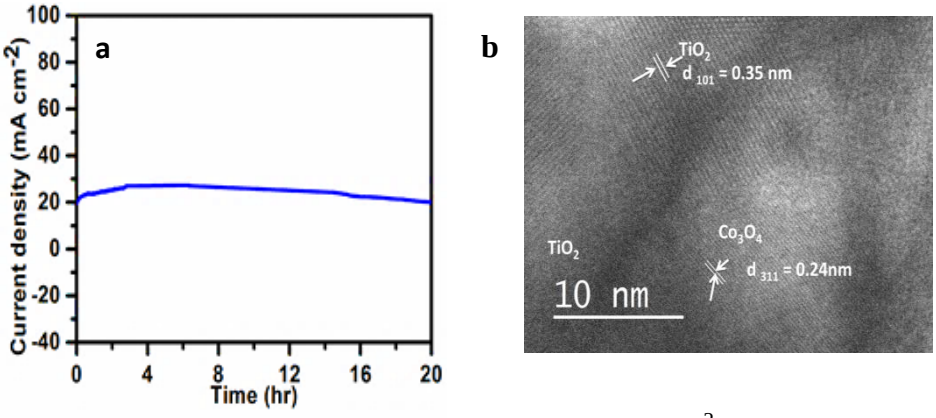

Fig 4.8: (a) Chronoamperometry curve for catalyst at 20 mA/cm^2 for 15 hours (b) HRTEM after the stability studies

The electrochemical active surface area (ECSA) helps to get an impression and idea about the abundance and availability of the catalytic active sites on the catalyst surface. The double-layer capacitance is obtained by performing the Cyclic voltammetry measurements preferably in the non-periodic region, i.e. (1.02 V to 1.14 V vs R.H.E) for the catalyst as well as supporting catalyst as shown in Fig (4.9 (a-c)). A plot of scan rate versus Δj was assembled Fig (4.9d) and the slope of the curve obtained gave the value of double-layer capacitance per unit area from which ECSA is estimated. The Cdl value of the catalyst, Co_3O_4, and TiO_2 are 8 mF/cm^2, 3.6 mF/cm^2, and 2.4 mF/cm^2 respectively. The higher value of Cdl for the catalyst suggests the abundant availability of active sites which results in higher activity as compared to the other catalysts.

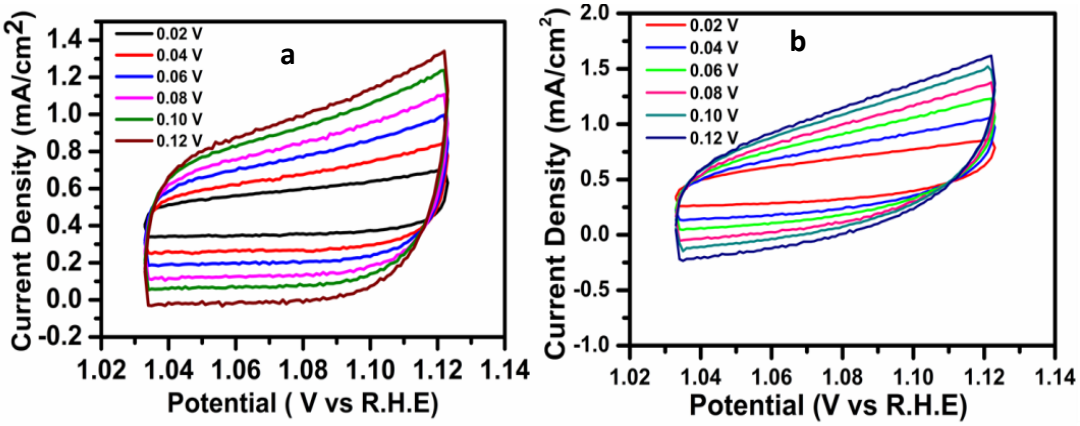

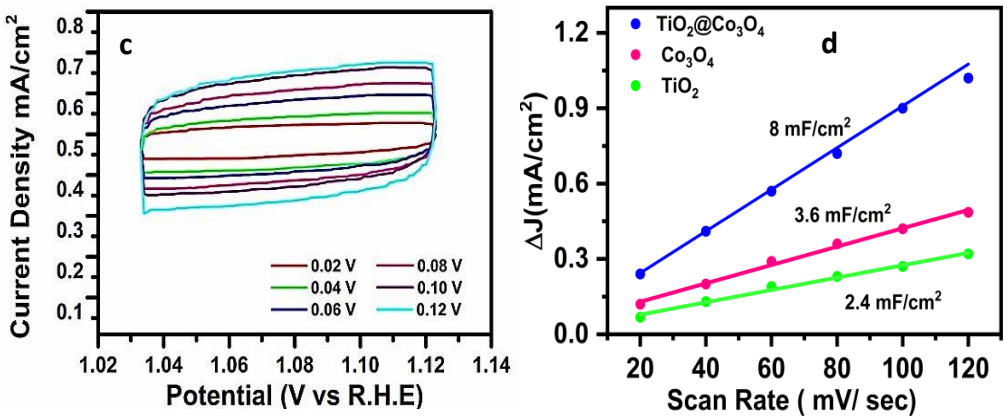

Fig 4.9: CV of (a) $TiO_2@Co_3O_4$ catalyst (b) Co_3O_4 (c) TiO_2 (d) Cdl of $TiO_2@Co_3O_4$ catalyst, TiO_2 and Co_3O_4

The faradic efficiency of the catalyst was calculated using the water displacement method Fig 5a) where the amount of oxygen liberated was determined. The volume of oxygen gas evolved is calculated theoretically as well as experimentally where the ratio of above two accounts for 97.9 % of faradaic efficiency for $TiO_2@$ Co_3O_4 catalyst. The specific activity of the catalyst is further proven with the help of turnover frequency. By supposing the active participation of each site the $TiO_2@Co_3O_4$ catalyst has TOF of 0.025 sec^{-1} at 400 mV which is larger than the 0.007sec^{-1} and 0.003 sec^{-1} for Co_3O_4 and TiO_2 respectively Fig (5b).

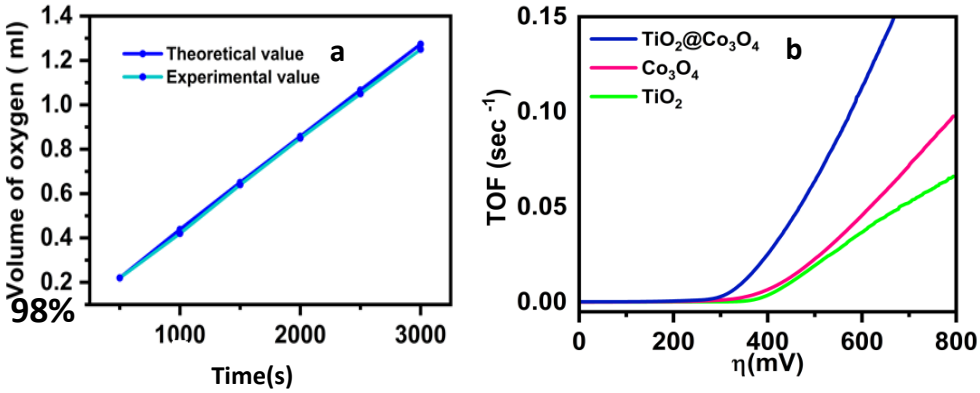

Fig 5.0: (a) Faradaic efficiency of $TiO_2@$ Co_3O_4 catalyst (b) TOF plot of $TiO_2@$ Co_3O_4 catalyst, TiO_2, and Co_3O_4

4.5. Conclusion:

In summary, the TiO_2@Co_3O_4 catalyst was synthesized using a simple two-step methodology. A hybrid nanostructure with Mesoporous TiO_2 embedded on the Co_3O_4 Nanosheets was fabricated. Amalgamations of TiO_2 with other transition metal oxides (TMOs) is a new methodology where the interface between the two phases plays a crucial role in accelerating the OER activity without involving conductive carbon substrates as an integral support system. This is the first time we have reported how Mesoporous TiO_2 can be used for the enhancement of the OER activity for a sheet-like Co_3O_4. Such synergistic effect is not been reported for OER activity yet. The catalytic activity of Co_3O_4 Nanosheets simply gets enhanced in presence of Mesoporous titanium oxide. The hetrostructure displays an OER activity with overpotential of 340 mV at 20 mA/cm^2 with the long-term stability of 20 hrs. The double-layer capacitance (C_{dl}) also indicates a higher activity for TiO_2@Co_3O_4 to the corresponding individual phased catalysts.

Catalyst	**η @10 mA/cm^2**	**Electrolyte**	**Ref**
Co_3O_4 / w MWCNTs	390 mV	0.1M KOH	[43]
Co_3O4/N-CNTs grafted carbon polyhedron	420 mV	1M KOH	[44]
C-NiOx/polypyrole	341 mV	1M KOH	[45]
Cu@NiFe LDH	310 mV	1M KOH	[46]
$Fe(OH)_3$:$Cu(OH)_2$	310 mV	1M KOH	[47]
Ni-Co BPTC MOF	348 mV	1M KOH	[48]
Ni-BDC MOF/NF	320 mV	1M KOH	[49]
$Ni_{0.75}Fe_{0.25}$-LDHs	350 mV	1M KOH	[50]
$Ni_{0.75}V_{0.25}$-LDHs	310 mV	1 M KOH	[51]
Ni@BCN	470 mV	1 M KOH	[52]
NiCo-NS	334 mV	1.0 M KOH	[53]
NiFe(CoTSPc)/G	330 mV	1.0 M KOH	[54]
Exfoliated NiFe nano sheets for 8h	290 mV	1.0 M KOH	[55]
Exfoliated NiCo LDH nanosheets	367 mV	1.0 M KOH	[56]
$Ni_2Co^{III}Fe$-LDH/N-GO	314 mV	1.0 M KOH	[57]

CMN-500	290 mV	1 M KOH	[58]
$NixCo_{1-x}OOH$	350 mV	1 M KOH	[59]
$CoSe_{0.85\ 1}$	324 mV	1 M KOH	[60]
TiO_2@Co_3O_4	**340 mv**	**1.0 M KOH**	**This work**

References

1. N. S. Lewis, *Science*, 2016, **351**, aad1920.
2. K. Zeng and D. Zhang, *Progress in energy and combustion science*, 2010, **36**, 307-326.
3. T. Hisatomi, J. Kubota and K. Domen, *Chemical Society Reviews*, 2014, **43**, 7520-7535.
4. E. L. Miller, *Energy & Environmental Science*, 2015, **8**, 2809-2810.
5. G. M. Joselin Herbert, S. Iniyan, E. Sreevalsan and S. Rajapandian, *Renewable and Sustainable Energy Reviews*, 2007, **11**, 1117-1145.
6. A. Malik and A. H. Al-Badi, *Energy*, 2009, **34**, 1573-1578.
7. Y. Li and J. Lu, *ACS Energy Letters*, 2017, **2**, 1370-1377.
8. N.-T. Suen, S.-F. Hung, Q. Quan, N. Zhang, Y.-J. Xu and H. M. Chen, *Chemical Society Reviews*, 2017, **46**, 337-365.
9. C. C. L. McCrory, S. Jung, J. C. Peters and T. F. Jaramillo, *Journal of the American Chemical Society*, 2013, **135**, 16977-16987.
10. Q. Qian, Y. Li, Y. Liu, L. Yu and G. Zhang, *Advanced Materials*, 2019, **31**, 1901139.
11. C. C. L. McCrory, S. Jung, I. M. Ferrer, S. M. Chatman, J. C. Peters and T. F. Jaramillo, *Journal of the American Chemical Society*, 2015, **137**, 4347-4357.
12. J. Nai, Y. Lu, L. Yu, X. Wang and X. W. Lou, *Advanced Materials*, 2017, **29**, 1703870.
13. Y. Lee, J. Suntivich, K. J. May, E. E. Perry and Y. Shao-Horn, *The Journal of Physical Chemistry Letters*, 2012, **3**, 399-404.
14. Y. Zhang, Y. Wang, H. Jiang and M. Huang, *Small*, 2020, **16**, 2002550.
15. J. Zhao, J.-J. Zhang, Z.-Y. Li and X.-H. Bu, *Small*, 2020, **16**, 2003916.

16. B. Sidhureddy, J. S. Dondapati and A. Chen, *Chemical Communications*, 2019, **55**, 3626-3629.
17. H. J. Lee, S. Back, J. H. Lee, S. H. Choi, Y. Jung and J. W. Choi, *ACS Catalysis*, 2019, **9**, 7099-7108.
18. P. Peng, X.-M. Lin, Y. Liu, A. S. Filatov, D. Li, V. R. Stamenkovic, D. Yang, V. B. Prakapenka, A. Lei and E. V. Shevchenko, *ACS Applied Materials & Interfaces*, 2018, **10**, 24715-24724.
19. Z. Yan, H. Sun, X. Chen, H. Liu, Y. Zhao, H. Li, W. Xie, F. Cheng and J. Chen, *Nature Communications*, 2018, **9**, 2373.
20. W. Liu, R. Yin, W. Shi, X. Xu, X. Shen, Q. Yin, L. Xu and X. Cao, *ACS Applied Energy Materials*, 2019, **2**, 579-586.
21. W.-D. Zhang, X. Yan, T. Li, Y. Liu, Q.-T. Fu and Z.-G. Gu, *Chemical Communications*, 2019, **55**, 5467-5470.
22. K. Liu, C. Zhang, Y. Sun, G. Zhang, X. Shen, F. Zou, H. Zhang, Z. Wu, E. C. Wegener, C. J. Taubert, J. T. Miller, Z. Peng and Y. Zhu, *ACS Nano*, 2018, **12**, 158-167.
23. J. Liu, J. Nai, T. You, P. An, J. Zhang, G. Ma, X. Niu, C. Liang, S. Yang and L. Guo, *Small*, 2018, **14**, 1703514.
24. J. Wang, C. Chen, N. Cai, M. Wang, H. Li and F. Yu, *Nanoscale*, 2021, **13**, 1354-1363.
25. Y. Yuan, S. Adimi, X. Guo, T. Thomas, Y. Zhu, H. Guo, G. S. Priyanga, P. Yoo, J. Wang, J. Chen, P. Liao, J. P. Attfield and M. Yang, *Angewandte Chemie International Edition*, 2020, **59**, 18036-18041.
26. R.-Q. Yao, H. Shi, W.-B. Wan, Z. Wen, X.-Y. Lang and Q. Jiang, *Advanced Materials*, 2020, **32**, 1907214.
27. Y. Liang, X. Xiong, Z. Xu, Q. Xia, L. Wan, R. Liu, G. Chen and S. L. Chou, *Small*, 2020, **16**, 2000030-2000030.
28. P. Cai, J. Huang, J. Chen and Z. Wen, *Angewandte Chemie International Edition*, 2017, **56**, 4858-4861.
29. A. Gaur, P. K. Sachdeva, R. Kumar, T. Maruyama, C. Bera and V. Bagchi, *Sustainable Energy & Fuels*, 2021, **5**, 801-807.
30. P. Thangasamy, S. Oh, S. Nam, H. Randriamahazaka and I.-K. Oh, *Small*, 2020, **16**, 2001665.
31. L. Han, S. Dong and E. Wang, *Advanced Materials*, 2016, **28**, 9266-9291.

32. Y. Li, F.-M. Li, X.-Y. Meng, S.-N. Li, J.-H. Zeng and Y. Chen, *Acs Catalysis*, 2018, **8**, 1913-1920.
33. L. Li, Z. Hu, L. Tao, J. Xu and J. C. Yu, *ACS Applied Energy Materials*, 2020, **3**, 3071-3081.
34. C. Xie, Y. Wang, D. Yan, L. Tao and S. Wang, *Nanoscale*, 2017, **9**, 16059-16065.
35. X. Hu, T. Li, Y. Tang, Y. Wang, A. Wang, G. Fu, X. Li and Y. Tang, *Chemistry–A European Journal*, 2019, **25**, 7561-7568.
36. M. Zhu, S. Yu, R. Ge, L. Feng, Y. Yu, Y. Li and W. Li, *ACS Applied Energy Materials*, 2019, **2**, 4718-4729.
37. K. Zhu, Q. Li, Z. Xue, Q. Yu, X. Liu, Z. Shan and K. Liu, *ACS Applied Nano Materials*, 2020, **3**, 1019-1027.
38. Y. Liang, X. Xiong, Z. Xu, Q. Xia, L. Wan, R. Liu, G. Chen and S.-L. Chou, *Small*, 2020, **16**, 2000030.
39. L.-N. Han, L.-B. Lv, Q.-C. Zhu, X. Wei, X.-H. Li and J.-S. Chen, *Journal of Materials Chemistry A*, 2016, **4**, 7841-7847.
40. S. L. Zhang, B. Y. Guan, X. F. Lu, S. Xi, Y. Du and X. W. Lou, *Advanced Materials*, 2020, **32**, 2002235.
41. L. Liu, Z. Jiang, L. Fang, H. Xu, H. Zhang, X. Gu and Y. Wang, *ACS applied materials & interfaces*, 2017, **9**, 27736-27744.
42. J. Si, S. Xiao, Y. Wang, L. Zhu, X. Xia, Z. Huang and Y. Gao, *Nanoscale*, 2018, **10**, 2596-2602.
43. X. Lu and C. Zhao, *Journal of Materials Chemistry A*, 2013, **1**, 12053-12059.
44. J. Yang, J. K. Cooper, F. M. Toma, K. A. Walczak, M. Favaro, J. W. Beeman, L. H. Hess, C. Wang, C. Zhu and S. Gul, *Nature materials*, 2017, **16**, 335-341.
45. D. V. Morales, C. N. Astudillo, Y. Lattach, B. F. Urbano, E. Pereira, B. L. Rivas, J. Arnaud, J.-L. Putaux, S. Sirach and S. Cobo, *Catalysis Science & Technology*, 2018, **8**, 4030-4043.
46. L. Yu, H. Zhou, J. Sun, F. Qin, F. Yu, J. Bao, Y. Yu, S. Chen and Z. Ren, *Energy & Environmental Science*, 2017, **10**, 1820-1827.
47. C.-C. Hou, C.-J. Wang, Q.-Q. Chen, X.-J. Lv, W.-F. Fu and Y. Chen, *Chemical Communications*, 2016, **52**, 14470-14473.
48. Q. Liu, L. Xie, X. Shi, G. Du, A. M. Asiri, Y. Luo and X. Sun, *Inorganic Chemistry Frontiers*, 2018, **5**, 1570-1574.

49. V. Maruthapandian, S. Kumaraguru, S. Mohan, V. Saraswathy and S. Muralidharan, *ChemElectroChem*, 2018, **5**, 2795-2807.
50. D. Zhou, Z. Cai, Y. Jia, X. Xiong, Q. Xie, S. Wang, Y. Zhang, W. Liu, H. Duan and X. Sun, *Nanoscale Horizons*, 2018, **3**, 532-537.
51. J. Jiang, F. Sun, S. Zhou, W. Hu, H. Zhang, J. Dong, Z. Jiang, J. Zhao, J. Li and W. Yan, *Nature communications*, 2018, **9**, 1-12.
52. S. Tang, X. Zhou, T. Liu, S. Zhang, T. Yang, Y. Luo, E. Sharman and J. Jiang, *Journal of Materials Chemistry A*, 2019, **7**, 26261-26265.
53. F. Song and X. Hu, *Nature communications*, 2014, **5**, 1-9.
54. Y. Liu, M. Zhang, D. Hu, R. Li, K. Hu and K. Yan, *ACS Applied Energy Materials*, 2019, **2**, 1162-1168.
55. B. Chen, Z. Zhang, S. Kim, S. Lee, J. Lee, W. Kim and K. Yong, *ACS applied materials & interfaces*, 2018, **10**, 44518-44526.
56. H. Liang, F. Meng, M. Cabán-Acevedo, L. Li, A. Forticaux, L. Xiu, Z. Wang and S. Jin, *Nano letters*, 2015, **15**, 1421-1427.
57. D. Zhou, Z. Cai, X. Lei, W. Tian, Y. Bi, Y. Jia, N. Han, T. Gao, Q. Zhang and Y. Kuang, *Advanced Energy Materials*, 2018, **8**, 1701905.
58. J. Bai, J. Mei, T. Liao, Q. Sun, Z. G. Chen and Z. Sun, *Advanced Energy Materials*, 2022, **12**, 2103247.
59. L.-a. Huang, Z. He, J. Guo, S.-e. Pei, H. Shao and J. Wang, *Nano Research*, 2020, **13**, 246-254.
60. H. Liu, X. Li, C. Peng, L. Zhu, Y. Zhang, H. Cheng, J. Cui, Q. Wu, Y. Zhang and Z. Chen, *Journal of Materials Chemistry A*, 2020, **8**, 13150-13159.

Chapter 5

Self-supported $CoVW_{0.025}LDH$ as Hydrogen Evolution Catalyst in Alkaline medium.

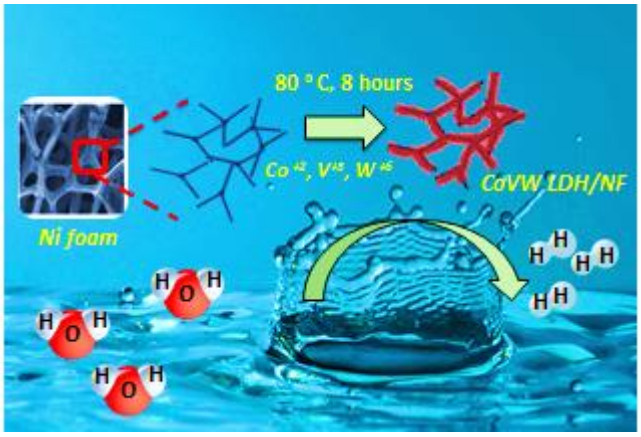

ABSTRACT

Self-supported $CoVW_{0.025}LDH$ Nanosheets were grown on nickel foam which acts as a superior catalyst for hydrogen evolution reaction in an alkaline medium. W on being introduced as a dopant into the lattice of CoVLDH Nanosheets tunes the electronic structure that enhances the activity thereby decreasing the overpotential from 200 mV to 127 mV. Moreover, the catalyst has a low value of Tafel slope indicating faster kinetics which is also reflected by a low value of charge transfer resistance. The catalyst was also found to be stable for 20 hours at a current density of 10 mA/cm^2.

5.1. Introduction

Rapidly increasing energy demands and severe environmental concerns have outstretched the demand for developing renewable energy systems [1-3]. In this context, hydrogen turns out to be an appropriate cleaner substitute owing to its high energy density and environment-friendly combustion products [4-6]. Electrochemical water splitting involving hydrogen evolution reaction is one of the most convenient routes for the production of hydrogen where hydrogen is produced from water either in an acidic medium ($2H^+ + 2e^- \longrightarrow H_2$) or alkaline/neutral medium ($H_2O + 2e^- \longrightarrow H_2$). The kinetics of HER reaction in an alkaline medium is greatly confronted by the Volmer step which carries the necessity of optimum adsorption and desorption of water molecules. The dissociation of water molecules creates an additional energy barrier which slows down the overall reaction [7]. Surprisingly, platinum which is considered the ideal catalyst for hydrogen evolution reaction in an acidic medium fails to showcase its superior performance in an alkaline medium [8]. Thus it is highly desirable to develop a catalyst for alkaline hydrogen evolution water reaction which has the competency to cross the barrier of water oxidation. Double layer hydroxides based on Co, Ni, Fe, and Mn have recently emerged as an efficient catalyst for OER due to high conductivity and novel structures. They are represented as $[M^{2+}_{1-x}M^{3+}_{x}(OH)_2]^{x+}(A^{n-})_{x/n}\cdot mH_2O$ consisting of positively charged host layers interlayered by exchangeable negative anions [9, 10]. However, the layered double hydroxides (LDHs) show enormously poor HER activity imparting high voltage for overall water splitting in an alkaline medium [11]. It has been noticed from the literature that LDH material show enhancement in HER activity when clubbed with carbon-based materials with or without heteroatom [12]. E.g. Jia et al showed that Ni Fe LDH shows improvement in the HER activity in an alkaline medium on combining with defect-rich graphene sheets [13]. A similar kind of enhancement was also witnessed in Fe Co LDH on combining with graphdyine by Hui et al where the current density reached 500 mA/cm^2 [14]. Incorporating third metal into the bimetallic LDH lattice was also found to be an interesting approach by the researchers in elevating the alkaline HER activity which is sometimes designated as trimetallic hydroxides LTH [15]. Barber et al reported better activity of FeNiCo LDH as compared to NiCo LDH [16]. They further inferred that such an improvement in activity was observed due to an increase in the abundance of metal sites. In the chain of trimetallic LDH. Dinh et al introduced less explored vanadium into the NiFe LDH system and claimed a similar kind of enhancement [17]. Lately, Mo was introduced in the NiCo LDH system by Hao et al which again displayed better performance than the bimetallic LDH

system [18]. Although Cobalt and vanadium, hydroxides have also shown interesting results for oxygen evolution reaction as reported recently by Mingyang et al.[19] and Juzhe et al.[20] But they fail to show satisfactory performance for hydrogen evolution reaction thereby limiting their applicability as a catalyst for overall water splitting. In a recent report made by Dang and his co-workers, W doped NiFe LDH shows remarkable activity for alkaline water splitting [21]. With the help of theoretical calculations, they have claimed that the synergistic effect between W and Ni Fe decreases the kinetic barrier for HER. Enthused by the above considerations and to understand how W can play a beneficiary role in modulating the HER activity of Cobalt vanadium-based LDH, we have synthesized self-supported W doped CoV LDH Nanosheets on Ni foam. By varying the ratio of W in the reaction mixture three different samples of $CoVW_x$LDH were obtained where x is 0.025mmol, 0.5mmol, and 0.125 mmol. The sample $CoVW_{0.025}$/LDH displays a low overpotential of 127 mV at a current density of 10 mA/cm^2. This simple methodology can be further extended to other self-supported CoVM (M is Ni, Fe, and Mn) LDH electrocatalysts which can catalyze the electrochemical reactions efficiently.

5.2 Experimental Section

5.2.1 Materials and Chemicals

Cobalt chloride hexahydrate ($CoCl_2 \cdot 6H_2O$), sodium tungsten dihydrate ($Na_2WO_4.2H_2O$), Potassium hydroxide (KOH), Nafion (5 %) per fluorinated resin, Pt/C all purchased from Sigma Aldrich. Ammonium metavanadate (NH_4VO_3, HI media), sodium hydroxide (NaOH, Loba Chemie), All the chemicals were used without purification. Distilled water was used to make aqueous solutions. Nickel foam of (1X1 cm^2) was cleaned by sonication in with 6 M HCl followed by ethanol and distilled water for 10 minutes to remove the surface impurities.

5.2.2 Synthesis Procedures

5.2.2.1 Synthesis of $CoVW_{0.025}$ LDH catalyst

The catalyst was synthesized on nickel foam. Before use, nickel foam was activated using a standard protocol. Nickel foam was cut into the desired dimension and first dipped in 3 M HCl solution and sonicated for 15 minutes followed by sonication in acetone and distilled water and then oven-dried. The catalyst was synthesized in one pot using the precipitation method. In detail, 3 mmol of $CoCl_2.6\ H_2O$ was dissolved in 20 ml of distilled water in one

beaker, and in another beaker 1 mmol of ammonium metavanadate, 0.025 mmol of sodium tungstate, 0.1mole of sodium hydroxide was dissolved in 20 ml distilled water. Cobalt chloride solution was slowly added into another solution in an oil bath maintained at 80 deg. The resulting solution was stirred for 30 minutes. Pre-washed nickel foam was added to the above solution and kept overnight for growth of $CoVW_{0.025}$ LDH. Other series of samples were synthesized by adopting a similar procedure and varying the amount of sodium tungstate in the reaction i.e. 0.0125 mmol and 0.05 mmol. The optimized concentration showing the best activity is 0.025 mmol, other concentrations show poor CoVLDH was synthesized by a similar protocol except for the addition of sodium tungstate.

5.2.2.2 Synthesis of CoVLDH

CoVLDH was synthesized by a similar procedure as above except for the addition of sodium tungstate.

5.3 Characterization

5.3.1 Physical Characterization

PXRD spectra of the $CoVW_{0.025}$LDH catalyst and CoVLDH were recorded on Bruker Eco D8 advance with Cu Kα radiation (λ = 1.54056 Å), from 2θ 10^o to 80^o and step size of 0.019^o; Scanning electron microscopy was done using JSM 7610 FPlus; JEM-2100 TEM was operated at 200 kV to capture the TEM images. XPS studies were done using ESCA Lab: 220-IXL equipped with Mg Kα nonmonochromated X-ray beam having photon energy 1253.6 eV.

5.3.2 Electrochemical Studies

The electrochemical measurements were performed on Auto lab multichannel M 204 PGSTAT (Metrohm) in a three-electrode configuration. $CoVW_{0.025}LDH$ (1 x 1 cm^2) NF was used as the working electrode, and Ag/AgCl (3 M) and graphite rod were used as the reference and counter electrodes**.** 1 M KOH (pH =13.7) was used as an electrolyte and all the potentials were reported to (RHE) as per the equation:

$$E_{(RHE)} = E\ (Ag/AgCl) + 0.197 + 0.0591 * pH$$

Linear sweep voltammetry curves were recorded at a low scan rate of 5 mV/sec. Electron impedance spectra were recorded from 0.01 Hz to 100000 Hz at -1.10 V vs Ag/AgCl. Chronoamperometry curves were recorded at a current density of 10 mA/cm^2 for 20 hours and 50 mA/cm^2 for 15 hours. The electrochemical surface area was analyzed from double-layer capacitance. For the evaluation of Cdl cyclic voltammetry studies were performed at different scan rates in the non- faradaic region. i.e. from 0.86 V to 0.98 V vs R.H.E. Cdl was further calculated from the slope of the plot obtained by Δj (j_a-j_c) vs scan rate where ECSA is given by ECSA = Cdl/Cs where Cs is surface capacitance which is 1.7 mF /cm^2 for Ni foam.

5.4 Results and Discussion

The $CoVW_{0.025}LDH$ samples were obtained by the one-pot precipitation method. The precipitates were collected after the reaction and used for PXRD analysis. The powder X-ray diffraction (XRD) pattern of the $CoVW_{0.025}LDH$, as well as CoVLDH, is shown in Fig (5.1a). Peaks obtained at 11.8^o, 22.7^o, 34.4^o, 39.3^{o,} and 64.9^o are indexed to (003), (006), (102), (105), and (116) crystal planes of CoVLDH structure.

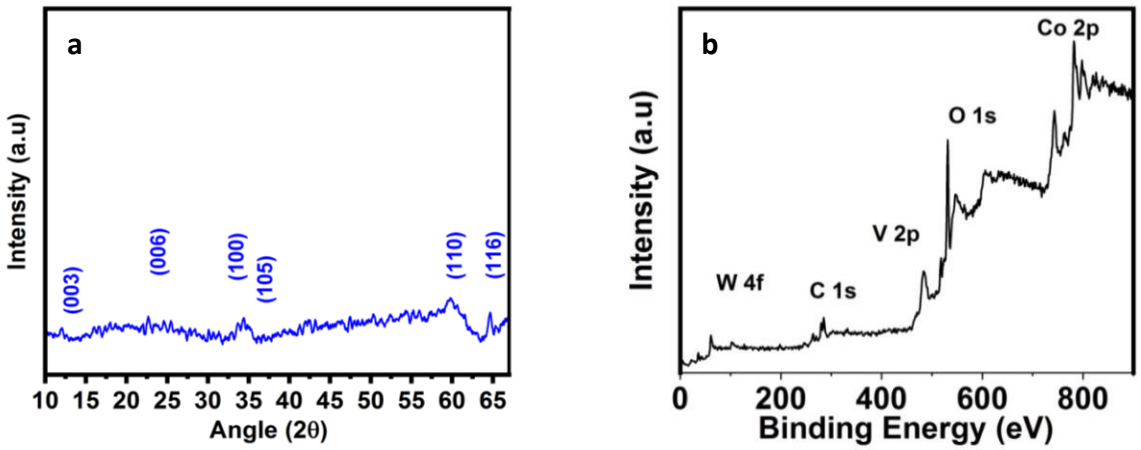

Fig 5.1: PXRD spectra of (a) $CoVW_{0.025}LDH$ (b) XPS wide scan spectra of $CoVW_{0.025}$ LDH

After elucidating the structure the chemical state of the $CoVW_{0.025}$ LDH was analyzed using XPS. For better understanding and detailed analysis, XPS studies were also done for CoV LDH. The wide scan spectra of $CoVW_{0.025}LDH$ are shown in Fig (5.1b) which contains the peaks corresponding to Co, V, and W elements in an atomic ratio of approximately 3:1:1 confirming the assimilation of W in the CoVLDH. The high-resolution Co 2p spectra for $CoVW_{0.025}$ LDH are shown in Fig (5.2a) which show two major peaks one positioned at 781.5 eV and the other at 797.1 eV along with two satellite peaks (787 eV and 801.3 eV). The

energy between the peaks Co $2p_{1/2}$ and Co $2p_{3/2}$ is equal to 16.1 eV which is a direct characteristic of high spin Co^{+2} state [22]. The high-resolution O 1s spectra are shown in Fig (5.2b) where one distinct peak is observed at 531 eV both in the case of CoVLDH and $CoVW_{0.025}$LDH which is referred to as M-OH bond [23]. For V 2p spectra of $CoVW_{0.025}$LDH, two peaks appeared in the high-resolution spectra, one at 517 eV and the second one at 524 eV as displayed in Fig (5.2c). The energy separation between two peaks is 7 eV which corresponds to V^{+5} oxidation state [24]. The high-resolution W4f spectra are shown in Fig (5.2d) where peaks allocated at 34.9 eV and 37.2 eV are assigned to W $4f_{7/2}$ and W $4f_{5/2}$ spin states respectively giving a clear indication of the presence of W in +6 oxidation state [25]. In comparing the Co 2p spectra obtained in the case of CoVLDH it is interesting to observe a positive shift of 0.5 eV both in the case of Co $2p_{3/2}$ and Co $2p_{1/2}$ whereas in spectra of V 2p a positive shift of 0.9 eV for V $2p_{3/2}$ is observed. This keen observation in XPS data suggest on assimilation of W in CoV lattice has modulated the electronic environment which is responsible for huge improvement in the activity.

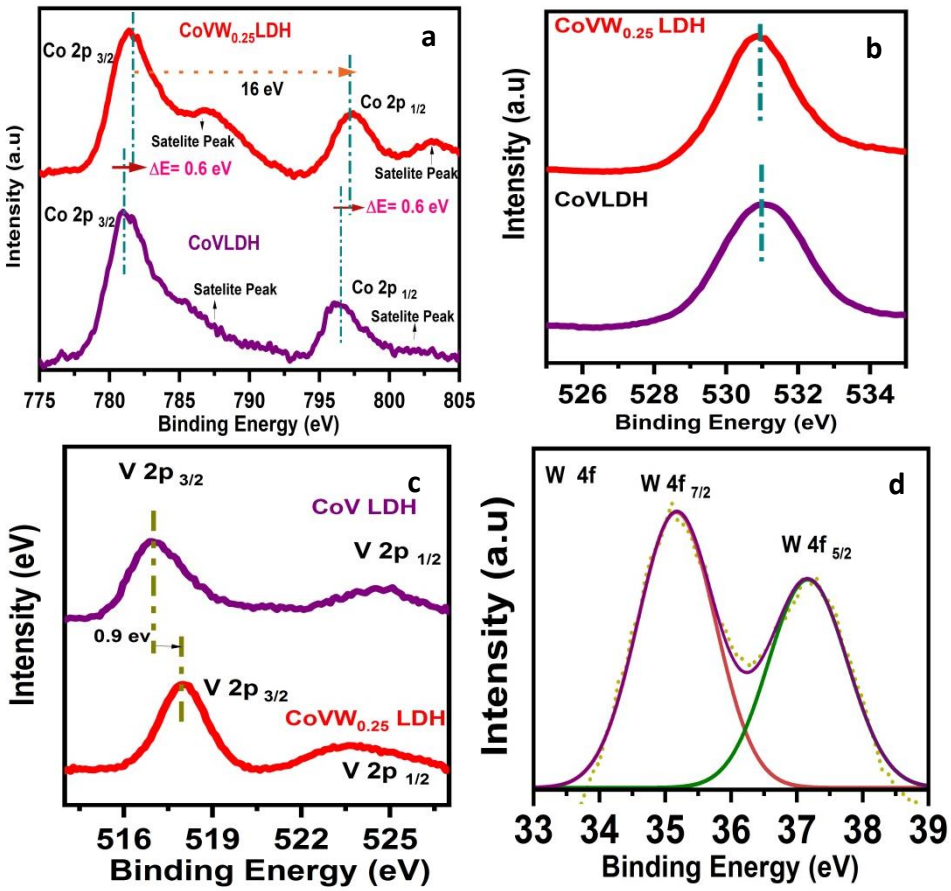

Fig 5.2 High resolution (a) Co 2p spectra (b) O1s spectra (c) V 2p spectra (d) W 4f spectra of CoVLDH and $CoVW_{0.025}$ LDH

After elucidating the structure the morphology of the $CoVW_{0.025}$LDH catalyst was investigated using scanning electron microscopy. Fig (5.3a-d) shows the SEM images of bare Ni foam as well as the catalyst where we can see that the porous network of nickel foam substrate was uniformly covered with $CoVW_{0.025}$LDH Nanosheets after the reaction. EDX elemental mapping images along with EDX spectra further confirm the uniform distribution of all the elements present in the catalyst as shown in Fig (5.3e-k).

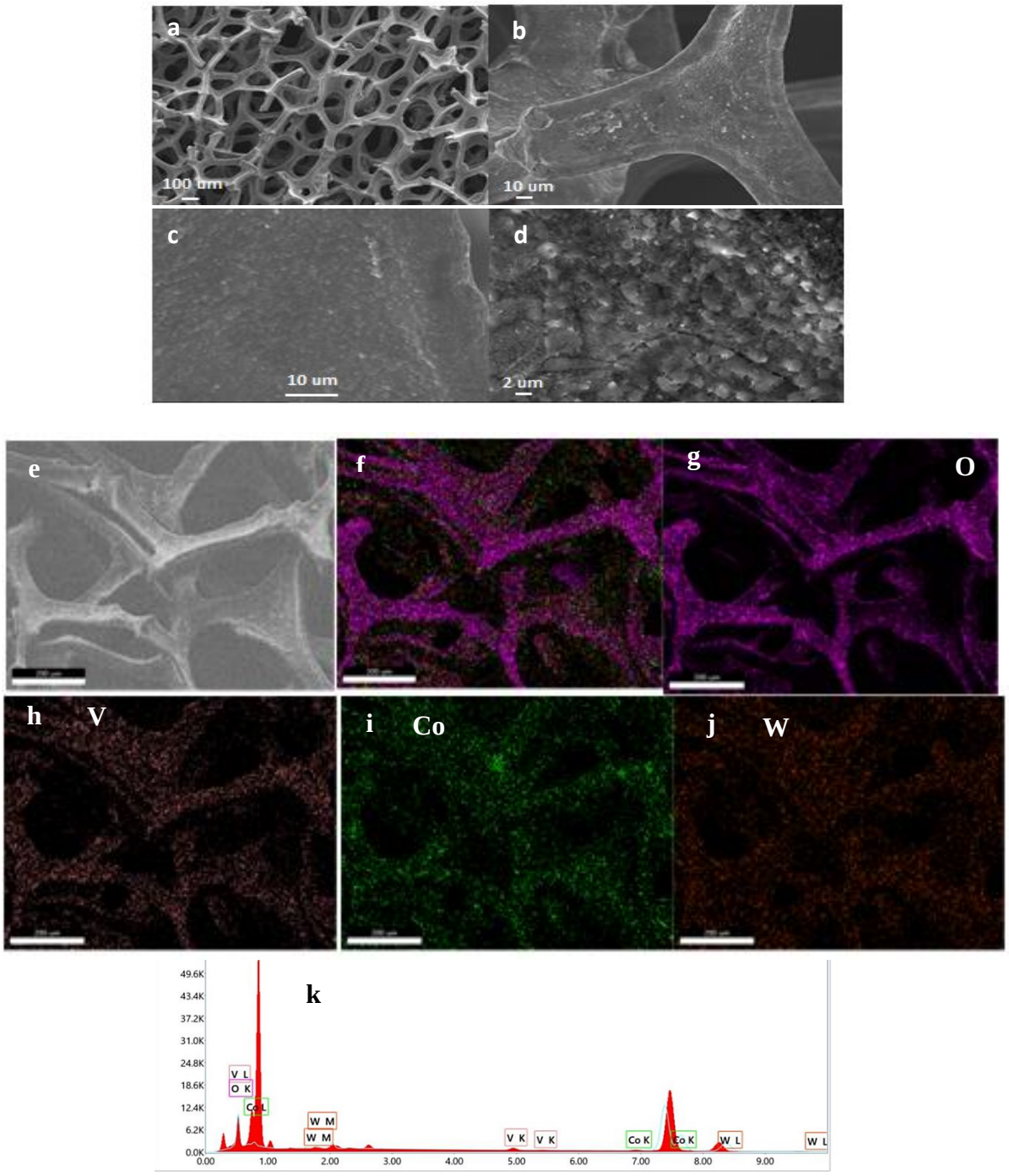

Fig 5.3: (a-d) SEM images of bare nickel foam and $CoVW_{0.025}$LDH (e-k) EDX elemental mapping with EDX spectra

After structural characterization and morphology study, the catalytic performance of $CoVW_{0.025}LDH$ is evaluated along with CoVLDH and Pt/C. The linear sweep voltammetry curves are recorded at a scan rate of 2 mV/sec in 1 M KOH as shown in Fig (5.4a). To attain a current density of 10 mA/cm^2 $CoVW_{0.025}LDH$ requires an overpotential of 127 mV which is less as compared to CoVLDH which requires 200 mv as shown in Fig (5.4b). Moreover, the current density in the case of $CoVW_{0.025}LDH$ is as high as Pt/C confirming the efficacy of the former. Such superior performance in the case of $CoVW_{0.025}LDH$ can be attributed to the presence of W which possesses optimal binding for H atoms thereby lowering the barrier for hydrogen evolution reaction.

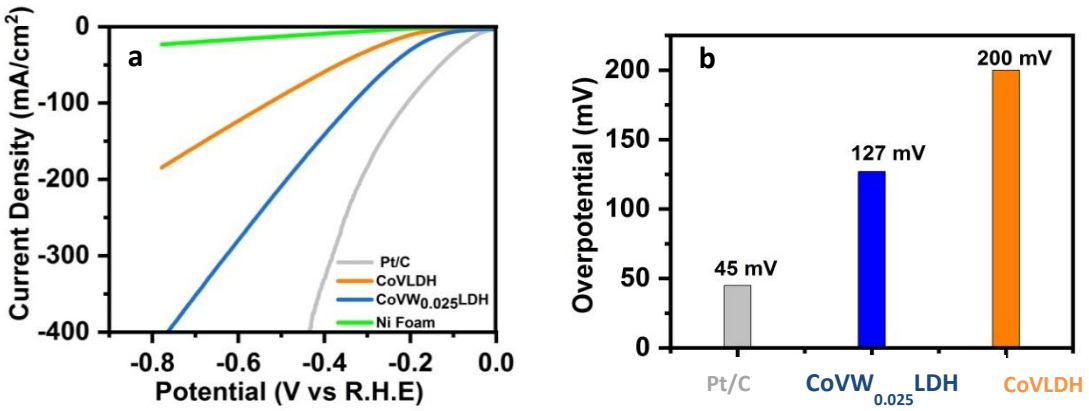

Fig 5.4: (a) Linear sweep voltammetry curves of $CoVW_{0.025}LDH$ catalyst along with CoV LDH and Pt/C (b) Bar graph showing the overpotential of the catalyst along with supporting catalyst.

To get an idea about the kinetics Tafel slope of $CoVW_{0.025}LDH$, CoVLDH is calculated along with Pt/C. Fig (5.5a) shows the Tafel plot of $CoVW_{0.025}LDH$, CoVLDH, and Pt/C where the Tafel slope in the case of $CoVW_{0.025}LDH$ is 144 mV /dec which is lower than that of CoV LDH i.e. 177 mV/dec indicating faster kinetics of HER reaction. The tafel slope in case of Pt/C is 88 mV/Dec. To get information about the conductive properties of the electrocatalyst electrochemical impedance spectra were recorded for the main catalyst as well as the counter catalyst Fig (5.5b). After fitting the impedance spectra with the equivalent circuit shown in the inset charge transfer resistance of $CoVW_{0.025}LDH$ is 3 ohm which is very less compared to CoVLDH which has a charge transfer resistance of 15 ohms. The low value of Rct again indicates a superior property of $CoVW_{0.025}LDH$

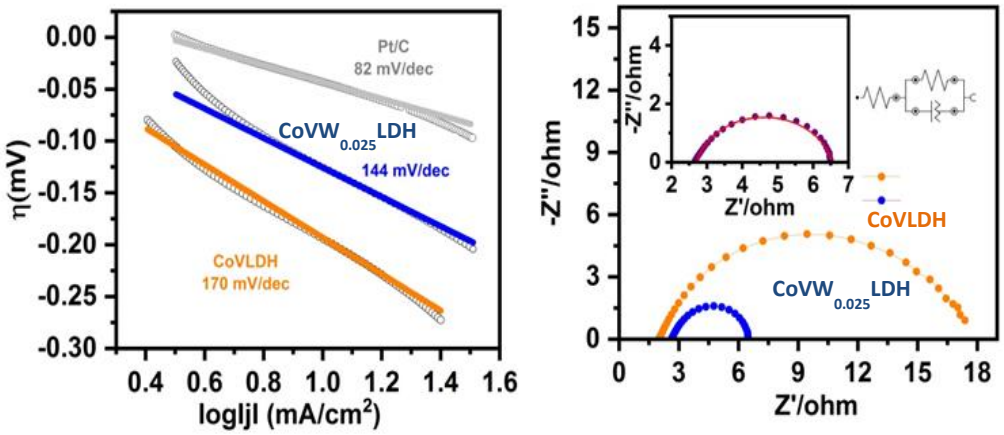

Fig 5.5 (a) Tafel slope of $CoVW_{0.025}$ LDH catalyst along with CoVLDH and Pt/ (b) C Nyquist plot of CoVLDH and $CoVW_{0.025}$LDH at 150 mV with inset showing the fitted Nyquist plot along with the equivalent circuit

Further to ensure the durability of $CoVW_{0.025}$LDH under prolonged operations Chroamperommetry studies were carried out at the current density of 10 mA/cm^2 for 20 hours as well as at a high current density of 50 mA/cm^2 for 15 hours. From the chronoamperometry curve as shown in Fig (5.6a) and Fig (5.6b) It can be inferred that catalyst shows very less loss in current density even after prolonged cycling with 99 % retention in current density after a time duration of 20 hours. Even at a higher current density of 50 mA/cm^2 catalyst was able to retain 86 % of its initial current density. These observations prove the durability of the catalyst.

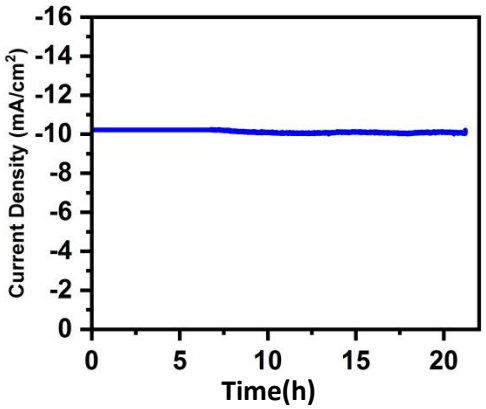

Fig 5.6 Chronoamperometry curve of $CoVW_{0.025}$LDH at current density at 10 mA/cm^2 for 20 hours.

The availability of abundant active sites also proves the superior performance of the catalyst. To have the clue about the same electrochemical surface area was calculated for both

$CoVW_{0.025}$LDH and CoVLDH by performing cyclic voltammetry measurements in potential window 0.86 V TO 0.98 V vs R.H.E. as shown in Fig (5.7a) and Fig (5.7b). Cdl was estimated from the slope of linear plot between current density and scan rate Fig (5.7c). The value of Cdl for $CoVW_{0.025}$LDH and CoVLDH is 2.5 mF/cm^2 and 1.5 mF/cm^2. The high value of Cdl for $CoVW_{0.025}$LDH indicates adequate availability of active sites which is responsible for the enhanced performance.

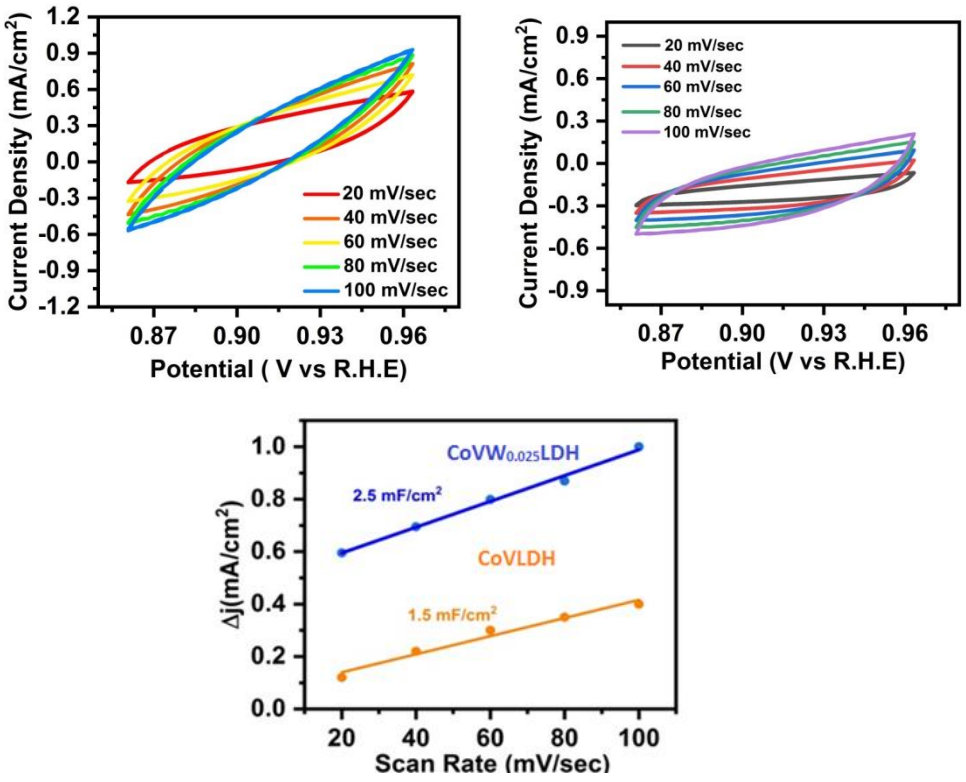

Fig 5.7 (a) CV plot of CoVLDH (b) CV plot of $CoVW_{0.025}$LDH (c) Cdl of $CoVW_{0.025}$ LDH and CoVLDH

Thus based on the above examination of HER performance of the synthesized catalyst, it can be said that W doped CoV LDH show remarkably improved activity as compared toCoVLDH due to a couple of reasons such as firstly due to changes in the electronic environment which are noticed in the XPS studies and secondly due to presence of W which has optimum binding energy for the proton thus facilitating the conversion to H_2.

Conclusion

In this work, the approach of using a third element was used to improve the activity of Cobalt vanadium layered double hydroxides for hydrogen evolution reaction in an alkaline medium. The presence of W in the high valence state of CoVLDH lattice boosts up the performance which is reflected by the sound decrease in the over- potential of CoVLDH from 200 mV to 127 mV. This rise in the activity can be attributed to the alteration in the electronic structure. Thus this strategy can be used further to explore the other LDH-based systems to enhance their performance for HER.

Table 5.1: Comparison of overpotentials at 10 mA/cm^2 with other reported catalysts in literature

Catalyst	η (mV)	Electrolyte	Ref
NiFeCo LDH	108	1 M KOH	[16]
NiFeV LDH	125	1 M KOH	[17]
NiFe LDH with trace Fe	170	1 M KOH	[26]
NiCo LDH	130	1 M KOH	[27]
CoFe LDH @g-C3N4	210	1 M KOH	[28]
Defected CoFe LDH	300	1 M KOH	[29]
NiCoFe LTH	185	1 M KOH	[16]
AuCoNi LDH	210	1 M KOH	[30]
CuCoFe LDH	190	1 M KOH	[31]
MnCo-$(CO)_3$-OH	190	1 M KOH	[32]
$Co_{0.85}$ Se NiFe LDH	260	1 M KOH	[33]
MoS_2 $Ni(OH)_2$	197	1 M KOH	[34]
MoS_2 $Co(OH)_2$	150	1 M KOH	[34]
CeO_x NiFe LDH	154	1 M KOH	[35]

$NiCo_2O_4$ NiFe LDH	190	1 M KOH	[36]
$CoVW_{0.025}$ LDH	**127 mv**	**1 M KOH**	**This work**

References

1. H. Du, L. Xia, S. Zhu, F. Qu and F. Qu, *Chemical Communications*, 2018, **54**, 2894-2897.
2. Y. Zhou, S. Sun, J. Song, S. Xi, B. Chen, Y. Du, A. C. Fisher, F. Cheng, X. Wang and H. Zhang, *Advanced Materials*, 2018, **30**, 1802912.
3. H. Du, X. Guo, R.-M. Kong and F. Qu, *Chemical Communications*, 2018, **54**, 12848-12851.
4. H. Du, R.-M. Kong, X. Guo, F. Qu and J. Li, *Nanoscale*, 2018, **10**, 21617-21624.
5. C. Wu, Y. Yang, D. Dong, Y. Zhang and J. Li, *Small*, 2017, **13**, 1602873.
6. J. Tian, Q. Liu, A. M. Asiri and X. Sun, *Journal of the American Chemical Society*, 2014, **136**, 7587-7590.
7. S. Anantharaj, S. Noda, V. R. Jothi, S. Yi, M. Driess and P. W. Menezes, *Angewandte Chemie International Edition*, 2021.
8. J. Durst, *Energy Environ. Sci*, 2014, **7**, 2255.
9. X. Long, Z. Wang, S. Xiao, Y. An and S. Yang, *Materials today*, 2016, **19**, 213-226.
10. Y. Wang, D. Yan, S. El Hankari, Y. Zou and S. Wang, *Advanced Science*, 2018, **5**, 1800064.
11. D. Li, B. Zhang, Y. Li, R. Chen, S. Hu and H. Ni, *Electrochemistry Communications*, 2019, **101**, 23-27.
12. M. Pumera, *ACS Catalysis*, 2020, **10**, 7087-7092.
13. L. Hui, Y. Xue, B. Huang, H. Yu, C. Zhang, D. Zhang, D. Jia, Y. Zhao, Y. Li and H. Liu, *Nature communications*, 2018, **9**, 1-11.
14. Y. Jia, L. Zhang, G. Gao, H. Chen, B. Wang, J. Zhou, M. T. Soo, M. Hong, X. Yan and G. Qian, *Advanced Materials*, 2017, **29**, 1700017.
15. A.-L. Wang, H. Xu and G.-R. Li, *ACS Energy Letters*, 2016, **1**, 445-453.
16. P. Babar, A. Lokhande, V. Karade, B. Pawar, M. G. Gang, S. Pawar and J. H. Kim, *ACS Sustainable Chemistry & Engineering*, 2019, **7**, 10035-10043.

17. K. N. Dinh, P. Zheng, Z. Dai, Y. Zhang, R. Dangol, Y. Zheng, B. Li, Y. Zong and Q. Yan, *Small*, 2018, **14**, 1703257.
18. S. Hao, L. Chen, C. Yu, B. Yang, Z. Li, Y. Hou, L. Lei and X. Zhang, *ACS Energy Letters*, 2019, **4**, 952-959.
19. M. Yang, X. Fu, M. Shao, Z. Wang, L. Cao, S. Gu, M. Li, H. Cheng, Y. Li and H. Pan, *ChemElectroChem*, 2019, **6**, 2050-2055.
20. J. Liu, Y. Ji, J. Nai, X. Niu, Y. Luo, L. Guo and S. Yang, *Energy & Environmental Science*, 2018, **11**, 1736-1741.
21. L. Ding, K. Li, Z. Xie, G. Yang, S. Yu, W. Wang, H. Yu, J. Baxter, H. M. Meyer and D. A. Cullen, *ACS Applied Materials & Interfaces*, 2021, **13**, 20070-20080.
22. J. Liu, Y. Ji, J. Nai, X. Niu, Y. Luo, L. Guo and S. Yang, *Energy & Environmental Science*, 2018, **11**, 1736-1741.
23. M. Zhang, L. Ding, J. Zheng, L. Liu, H. Alsulami, M. A. Kutbi and J. Xu, *Applied Surface Science*, 2020, **509**, 145348.
24. M. Xing, L.-B. Kong, M.-C. Liu, L.-Y. Liu, L. Kang and Y.-C. Luo, *Journal of Materials Chemistry A*, 2014, **2**, 18435-18443.
25. R. Liu, Y. Lin, L. Y. Chou, S. W. Sheehan, W. He, F. Zhang, H. J. Hou and D. Wang, *Angewandte Chemie International Edition*, 2011, **50**, 499-502.
26. G. Rajeshkhanna, T. I. Singh, N. H. Kim and J. H. Lee, *ACS Applied Materials & Interfaces*, 2018, **10**, 42453-42468.
27. W. Liu, J. Bao, M. Guan, Y. Zhao, J. Lian, J. Qiu, L. Xu, Y. Huang, J. Qian and H. Li, *Dalton Transactions*, 2017, **46**, 8372-8376.
28. T. Bhowmik, M. K. Kundu and S. Barman, *ACS Applied Energy Materials*, 2018, **1**, 1200-1209.
29. P. F. Liu, S. Yang, B. Zhang and H. G. Yang, *ACS applied materials & interfaces*, 2016, **8**, 34474-34481.
30. U. K. Sultana, J. D. Riches and A. P. O'Mullane, *Advanced Functional Materials*, 2018, **28**, 1804361.
31. L. Yu, H. Zhou, J. Sun, F. Qin, D. Luo, L. Xie, F. Yu, J. Bao, Y. Li and Y. Yu, *Nano Energy*, 2017, **41**, 327-336.
32. T. Tang, W.-J. Jiang, S. Niu, N. Liu, H. Luo, Y.-Y. Chen, S.-F. Jin, F. Gao, L.-J. Wan and J.-S. Hu, *Journal of the American Chemical Society*, 2017, **139**, 8320-8328.
33. Y. Hou, M. R. Lohe, J. Zhang, S. Liu, X. Zhuang and X. Feng, *Energy & Environmental Science*, 2016, **9**, 478-483.

34. Z. Zhu, H. Yin, C. T. He, M. Al-Mamun, P. Liu, L. Jiang, Y. Zhao, Y. Wang, H. G. Yang and Z. Tang, *Advanced Materials*, 2018, **30**, 1801171.
35. X. Wang, Y. Yang, L. Diao, Y. Tang, F. He, E. Liu, C. He, C. Shi, J. Li and J. Sha, *ACS applied materials & interfaces*, 2018, **10**, 35145-35153.
36. Z. Wang, S. Zeng, W. Liu, X. Wang, Q. Li, Z. Zhao and F. Geng, *ACS Applied Materials & Interfaces*, 2017, **9**, 1488-1495.

Appendix

CONCLUSION AND FUTURE PERSPECTIVE

Thesis Summary

This thesis comprises various nanomaterials synthesized to assist hydrogen evolution reaction as well as oxygen evolution reaction. The focus of this work is not only limited to synthesis but it also involves broad characterization of the synthesized materials using various physical and electrochemical techniques that helped me to attain comprehensive and deep knowledge about the role of heterostructures in enhancing the kinetics of electrochemical reactions.

- The first chapter deals with the understanding of the current scenario about the energy crisis, the role of renewable sources of energy for addressing the issues related to ocean acidification, global warming along with emerging hydrogen fuel technology. The focus and motive of the thesis are also explained in this chapter based on the intensive literature study.
- The second chapter is all about the information of materials and all the characterization tools that are used in the thesis. Characterization studies include structural characterization using PXRD, XPS, etc., morphological studies were done using SEM, TEM, and electrochemical studies that cover LSV, CV, GCD, EIS, etc.
- The third chapter is about the synthesis of reduced graphene oxide using a new and unique methodology that evolves minimum use of chemical reagents and does not involve any requirement of purification techniques after the reaction. With elaborative and peculiar theoretical studies clubbed by mechanistic studies, we have shown the existence of a transient species i.e. solvated electron in the reaction system that is responsible for carrying out the reduction of GO to RGO without compromising with the quality of RGO.
- Co_3O_4 has gained huge attention for oxygen evolution catalysis and it has been coordinated with other metal oxides, conductive carbon supports to cause additional refinement in the activity. Another aspect is also that Mesoporous TiO2 has never been in limelight for OER catalysis. Thus based on the above facts we have designed a heterostructure based on Mesoporous TiO_2 and Co_3O_4 nanosheets which shows good activity for oxygen evolution reaction. The detailed work is discussed in the fourth chapter.
- Double layer hydroxides have shown case prominent results in oxygen evolution reaction but their hydrogen evolution activity is not up to the mark. Thus with this

motive behind the fifth chapter involves the study of W doped CoV LDH as a catalyst for hydrogen evolution reaction in alkaline medium. The catalyst was found to show good durability at both low and high current densities.

Future Perspective

Thus by getting sound and broad knowledge about the importance of interface engineering from the work presented in this thesis the search of non-noble metal catalysts can be extended to the heterostructure between other compounds of earth-abundant transition metals such as nitrides, carbides, phosphides, oxides, hydroxides, sulfides. The use of conductive templates such as CNTs, aerogels, carbon cloth, and heteroatom doped RGO play a positive role in boosting the activity. Titanium oxide which is a good photo-catalyst can be alloyed with other transition metal oxides/ hydroxides to explore its electrochemical activity. Double layer hydroxides which have recently gained attention in water oxidation can be modified and tuned to be effective for hydrogen evolution reaction irrespective of the electrolyte medium.

MOF-based compounds that have high conductivity and high surface area can be used as host materials to hold the nanomaterials as well as they can be used to form heterostructures.

By designing and tuning the activity of heterostructures using various strategies the approach of catalysis can be diverted towards overall water splitting. The material should be devised in such a way that it has the capability of catalyzing both the half redox reactions i.e. HER and OER effectively.

One of the important points regarding catalysis is the ability of the material to show good activity irrespective of the pH of the electrolyte medium. Most of the time the catalyst is able to show the best performance only at one pH value. Thus the approach of catalysis can be diverted to create new materials that can work for both HER and OER at all pH.

Thus it can be concluded that this area has still a lot to be explored on the practical ground so that material synthesis and their applicability can be extended to an industrial scale which will provide a huge relief from the ongoing energy thirst and environmental degradation.

LIST OF PUBLICATIONS

1. **Rai, R.;** Ahmed, Z.; Kumar, R.; Kumawat, R. L.; Chordiya, K.; Maruyama, T.; Ali, M. E.; Bagchi, V., Environmentally Benign Metal-Free Reduction of GO Using Molecular Hydrogen: A Mechanistic Insight. ACS Omega 2018, 3 (11), 15112-15118.

2. **Ritu Rai;** Ashish Gaur; Zubair Ahmed; Shilpa Kumari; Krishankant; Vikas Pundir; Rajinder Kumar; Deepak Upreti; Takahiro Maruyama; Vivek Bagchi; Ultrathin Co3O4 nanosheet wrapped mesoporous TiO_2 for oxygen evolution reaction (submitted to Electroanalysis).

3. Kumar, R.; **Rai, R**.; Gautam, S.; De Sarkar, A.; Tiwari, N.; Jha, S. N.; Bhattacharyya, D.; Ganguli, A. K.; Bagchi, V., Nano-structured hybrid molybdenum carbides/nitrides generated in situ for HER applications. Journal of Materials Chemistry A 2017, 5 (17), 7764-7768

4. Kumar, R.; Ahmed, Z.; **Rai, R**.; Gaur, A.; Kumari, S.; Maruyama, T.; Bagchi, V., Uniformly Decorated Molybdenum Carbide/Nitride Nanostructures on Biomass Templates for Hydrogen Evolution Reaction Applications. ACS Omega 2019, 4 (9), 14155-14161.

5. Ahmed, Z.; **Rai, R**.; Kumar, R.; Maruyama, T.; Bagchi, V., Hydrated FePO4 nanoparticles supported on P-doped RGO show enhanced ORR activity compared to their dehydrated form in an alkaline medium. RSC Advances 2019, 9 (42), 24654-2465.

6. Zubair Ahmed; Parrydeep Kaur Sachdeva; **Ritu Rai**; Rajinder Kumar; Takahiro Maruyama,; Chandan Bera; Vivek Bagchi, " Promoting Electrocatalytic Oxygen Reduction in a Model Composite Using Selective Metal Ions. ACS Appl. EnergyMater.2020, 3, 3645−3652

7. Ahmed, Zubair; Krishankant,; **Rai, Ritu**; Kumar, Rajinder; Maruyama, Takahiro; Bera, Chandan; Bagchi, Vivek "Unravelling a graphene-exfoliation technique analogy in the making of ultrathin nickel-iron oxyhydroxides@nickel foam to promote OER". ACS Applied Materials & Interfaces 13(46).

8. Gaur, Ashish; Pundir, Vikas; ., Krishankant; **Rai, Ritu**; Kaur, Baljeet; Maruyama, Takahiro; Bera, Chandan; Bagchi, Vivek; Interfacial interaction induced OER activity of MOF derived super hydrophilic Co_3O_4-NiO hybrid nanostructures. Dalton Trans., 2022, 51, 2019-2025.

To be submitted soon

1. **Ritu Rai;** Krishankant; Zubair Ahmed; W doped CoV LDH for alkaline Hydrogen evolution reaction. (Manuscript under preparation)

LIST OF CONFERENCES ATTENDED

1. Participated in **"One Day Conclave on Nano Biotechnology (December 2014)**" organized by INST MOHALI.
2. Presented poster in **"Australia – India strategic research fund (AISRF) meeting - 2015"** organized by INST MOHALI.
3. Participated in **"CRICK Nanoscience Day" (JULY 2015)** "organized by INST MOHALI.
4. Participated in " **2 ND CRICK Nanoscience Day" (JULY 2015) "**organized by INST MOHALI
5. Presented poster in **"CACEE 2018"** organized by TIFR Mumbai.

WORKSHOPS and TRAINING

1. PARTICIPATED IN THE TWO-DAY COURSE **"ADVANCED MICROSCOPY AND IMAGING TECHNIQUE"** ORGANIZED BY DSS IMAGETECH PVT LTD, OLYMPUS MEDICAL SYSTEM, AND INST MOHALI.
2. ATTENDED WORKSHOP ON **"JEOL TEM, SEM &NMR PRODUCTS"** ORGANIZED BY INST MOHALI.
3. COMPLETED TRAINING ON **"STA 8000" AND "DSC 8000"** ORGANIZED BY INST MOHALI.

Vitae

RITU RAI

Ph.D. Research Scholar

Institute of Nanoscience and Technology
&
Indian Institute of Science Education and Research Mohali (Punjab), India

Ritu Rai completed her Bachelor's Honours Degree in 2010 and Master Honours Degree in 2012 in chemistry from the Department of chemistry, Panjab University, Chandigarh. In 2012 she joined as a guest lecturer in chemistry at Khalsa College for Women from July 2012 to July 2013. In 2014 she joined the Institute of Nanoscience and Technology as a Ph.D. scholar under the worthy guidance of Dr. Vivek Bagchi. She published and presented her work in several reputed scientific journals as well in national and international conferences. Her research area is dedicated to the synthesis of catalytic nanomaterials based on transition elements for electrocatalysis.